

Development of miniature double-focusing mass
spectrograph for lunar exploration

Masaru Nishiguchi

Department of Physics, Graduate School of Science,

Osaka University

March, 2006

Abstract

For space science, the analysis of the atmosphere and surface substances in planetary explorations is of interest. In particular, measurements of the elemental composition and the isotope ratio of surface substances provide basic information on the origin and evolution of the planet. A future lunar surface exploration using a rover was planned, in which the ice in the poles and isotope ratios of noble gases in the surface regolith and rocks will be investigated. A miniature double-focusing mass spectrograph has been developed for the lunar exploration.

The computer program TRIO 2.0 was developed for the design and evaluation of the ion optical systems. Many useful functions are provided with GUIs in TRIO 2.0. The aberration coefficients can be calculated up to third-order by the transfer matrix method. The following properties can be simulated and visualized: ion trajectories, the image of the beam profile, the beam envelope and the ion transmission, the TOF peak, and the energy and angular focal planes.

A new ion optical system of the miniature double-focusing mass spectrograph was designed by TRIO 2.0. The ion optical system was designed to satisfy the double-focusing along a straight line being at a distance from the exit fringe of the magnetic sector to employ a focal plane detector. In the design, the ion optical properties of the system, e.g., beam profile, mass resolution, beam envelope, and transmission were evaluated by TRIO 2.0. The constructed instrument is comprised of an EI ion source, a spherical electrostatic sector, a homogeneous magnetic sector and a focal plane detector using a CCD. A CCD driver system and a data acquisition system was developed.

The ion optical properties and the quantitative performance of the newly constructed instrument was evaluated. The mass resolution of 130 was achieved with the main slit width of 0.25 mm, which is in good agreement with the simulation. The detectable m/z range was estimated from a spectrum of the residual gases. The result was well consistent with the theoretically calculated value. The energy and the angular focal planes were evaluated. In the system, double-focusing was successfully achieved along a straight line. Furthermore,

the energy and angular focusing points were simulated to compare with the experimental result. These results of the experiment and the simulation well agreed with each other. In addition, the second-order element of the transfer matrix ($x|\delta\delta$) was measured experimentally as -0.47 ± 0.03 m. This measurement was in good agreement with the simulation by TRIO 2.0.

The quantitative performance of the instrument was evaluated. A dynamic range of the simultaneous detection was achieved as 300 from the spectrum of neon. The gain distribution of the employed focal plane detector was evaluated. The peak intensity of the isotope of neon fluctuated about 40%. This result shows that the gain distribution is inhomogeneous in the focal plane detector. However, sufficient reproducibility and linearity of the gain was achieved when the detecting position is fixed. The instrument could, therefore, provide a high sensitivity and a good quantitative performance if the gain distribution would be calibrated.

Contents

1	Introduction	1
2	Computer program “TRIO 2.0” for the design of ion optical systems	7
2.1	Introduction	7
2.2	Transfer matrix method	9
2.3	Computer program TRIO 2.0	12
2.3.1	Main frame	12
2.3.2	Simulation and visualization of ion trajectories	15
2.3.3	Simulation and visualization of the image of the beam profile	16
2.3.4	Simulation and visualization of the beam envelope and the ion transmission	19
2.3.5	Simulation and visualization of the TOF peak	22
2.3.6	Simulation and visualization of the energy and angular focal planes	22
2.4	Conclusion	26
3	Design of a miniature double-focusing mass spectrograph	30
3.1	Introduction	30
3.2	Design concept	30
3.3	Design of a miniature double-focusing mass spectrograph	32
3.4	Ion optical system	34
3.5	Numerical evaluation of the newly designed ion optical system	37
3.6	Conclusion	42
4	Instrumentation	45
4.1	Introduction	45
4.2	Whole instrument	45
4.3	Ion source	48
4.4	Spherical electrostatic sector	48

4.5	Homogeneous magnetic sector	50
4.6	Focal plane detector	54
4.6.1	MCP assembly	55
4.6.2	CCD area image sensor	56
4.6.3	CCD driver system	56
4.7	Data acquisition system	59
4.8	Conclusion	61
5	Evaluation of the miniature double-focusing mass spectrograph	63
5.1	Introduction	63
5.2	2D and 1D spectra	63
5.2.1	Observation of the phosphor layer image	63
5.2.2	2D and 1D spectra	64
5.2.3	Mass resolution	68
5.2.4	Evaluation of the detectable m/z range	71
5.3	Evaluation of the energy and angular focal planes	74
5.3.1	Method for the evaluation of the energy and angular focal planes	74
5.3.2	Dependence of the peak position on the voltage applied to the electrostatic sector	76
5.3.3	Temperature dependence of the peak position	77
5.3.4	Evaluation of the energy and the angular focal planes	80
5.4	Measurement of a second-order element of the transfer matrix ($x \delta\delta$) .	83
5.5	Simulation of the ion trajectories in the magnetic sector	85
5.6	Evaluation of the quantitative performance	91
5.6.1	Dynamic range of the simultaneous detection	91
5.6.2	Gain distribution in the detector	94
5.7	Conclusion	98
6	Conclusion	101

Chapter 1

Introduction

Since the first systematic investigation of positive rays was undertaken by Thomson with his parabola mass spectrograph during 1910–1920 [1.1], mass spectrometry has progressively evolved. In the early days of the mass spectrometry, it was used for isotopic analysis. Moreover, it has been applied to a broader research fields by developments of new ionization techniques. Almost any materials can be analyzed with a suitable ionization technique and a mass spectrometer. A mass spectrometric analysis provides identification of the materials and the abundance of each. It is being applied in physics, chemistry, biology, pharmacology, geology, environmental science, space science. In this thesis, the application of mass spectrometry to space science is described.

For space science, the analysis of the atmosphere and surface substances in planetary explorations is of interest. In particular, measurements of the elemental composition and the isotope ratio of surface substances provide basic information on the origin and evolution of the planet. Mass spectrometry is obviously the most suitable method for these purposes, so mass spectrometers have often been employed in past and present space missions. For example, two mass spectrometers were on board in the Viking mission in 1976: one was a double focusing mass spectrometer using Mattauch-Herzog geometry for analysis of the Martian atmosphere [1.2] and the other was a gas chromatograph (GC)-mass spectrometer employing a double focusing analyzer using Nier-Johnson geometry for the measurement of organic compounds in the surface soil [1.3]. Quadrupole mass spectrometers were also carried on several space probes to analyze the atmosphere: the Pioneer Venus in 1979 [1.4], the Galileo probe in 1989 [1.5], and the Cassini-Huygens in 1997 [1.6]. An instrument for space explorations must feature reduced size, weight, and electric power consumption. Magnetic sector, quadrupole or time-of-flight (TOF) mass spectrometers are generally employed for space exploration. Quadrupole and TOF analyzers have good potential for weight reduction because they consist of only electrodes. On the other hand, a magnetic sector analyzer is not amenable to weight reduction due to its heavy magnet. Magnetic analyzers, however, provide

a large dynamic range. If the exploration target is near the Earth, e.g., lunar or Mars exploration, the weight of the instrument is less crucial. In that case, a magnetic sector analyzer may provide the advantage of good quantitative performance.

In a magnetic sector-type instrument, the following well known relationship is satisfied:

$$\frac{m}{z} = \frac{r^2 B^2}{2V} \quad (1.1)$$

where m is the mass of the ion, z is the charge, r is the radius of the circular trajectory, B is the magnetic flux density, and V is the accelerating voltage. Generally, magnetic sector-type instruments are classified in two types by the method of the analysis for mass: one is called as “mass spectrograph” and the other is “mass spectrometer.” From equation 1.1, it can be found that mass of the ion can be determined by three parameters of r , B , and V . In mass spectrograph, parameters of B and V are fixed. Ion beams spatially dispersed by their mass are observed with a focal plane detector [1.7], e.g., a photographic plate, a micro-channel plate (MCP) based detector, etc. On the other hand, in mass spectrometer, the parameter of r is fixed. Mass of ions is successively varied by scanning the value of B or V , and ions are detected by an ion detector with a collector slit which is set at a fixed position corresponding the value of r . For an ion detector, a Faraday cup, an electron multiplier, etc. are employed.

During mass spectra are obtained with a mass spectrometer, most of the ions cannot pass through the collector slit and thus are not detected. If all the ions that pass through the analyzer are detected simultaneously, the detection efficiency can be drastically improved. Quantitative performance, furthermore, can also be improved by simultaneous detection because time-dependent fluctuations of the conditions of the ion source, power supplies, etc., can be eliminated. For these reasons, a mass spectrograph employing a focal plane detector is suited in principle for trace and quantitative analyses.

As commonly known, first, photographic plates has been employed as a focal plane detector in mass spectrographs until 1960s. A photographic plate, however, has numerous drawbacks. The dynamic range is limited, on the order of $10-10^3$. It is also inherently non-linear, which complicates quantitative analysis. Moreover, processing and analysis of a photographic plate is troublesome and time-consuming. Instead, focal plane detectors using electrical devices have been developed since the 1970s. For example, Giffin et al. [1.8]

applied a focal plane detector comprising a microchannel plate (MCP), a phosphor screen, a fiber-optic image dissector, and a vidicon camera system to a mass spectrograph with the Mattauch-Herzog geometry [1.9]. Murphy and Mauersberger [1.10] developed an MCP detector system that consists of an MCP, a phosphor layer on a fiber-optic bundle and a photodiode array. They operated the detector in ion counting mode for a mass spectrograph. Burgoyne et al. also employed an MCP with an active phosphor for a mass spectrograph [1.11]. They detected the phosphor images using a 1.32-cm charge-coupled device (CCD). Yurimoto et al. employed a stacked CMOS-type active pixel sensor for two-dimensional isotope ratio imaging in secondary ion mass spectrometry [1.12]. Thus, several types of devices have been used as focal plane detectors. An MCP is the most often used device as a focal plane detector. An MCP can convert ions into electron clouds at the position ions have arrived. Consequently, MCPs are generally combined with a system, which can detect these electrons and retain the spatial information. For this objective, two types of electron-detecting systems are employed. One is a device which directly detects these electrons; a multi-anode detector, a charge division detector, etc. The other is a photon detector with a phosphor screen; a CCD or a photodiode array, etc. In this system, the electron clouds from the MCP are firstly converted into light by the phosphor screen, then the light is detected by these photon detector. In recent years, thanks to progress in semiconductor technology, large CCDs with high spatial resolution have become available at comparatively low cost.

A future lunar surface exploration using a rover was planned as a subsequent mission of SELENE [1.13]. In the mission, it was planned to characterize the ice in the poles and measure isotope ratios of noble gases of the low mass range from He to Ar in the surface regolith and rocks. For this objectives, an instrument which achieves a good quantitative performance is required. As described above, a mass spectrograph, which provide the advantage of good quantitative performance, would be available for space exploration near the Earth. A miniature double-focusing mass spectrograph, therefore, has been developed as a prototype model for a lunar exploration [1.14]. In this thesis, the investigation and the development of a miniature double-focusing mass spectrograph for a lunar exploration are presented. The outline of this thesis is as follows:

Chapter 2:

In the design of any mass spectrometer, the investigation of the ion optics is essential. The computer program TRIO 2.0 equipping GUIs was developed for this purpose. It can calculate the aberration coefficients up to third-order for an ion optical system including drift spaces, electrostatic sectors, magnetic sectors, electric or magnetic quadrupole lenses, and multipole lenses. The program has many useful functions to evaluate the ion optical properties of a system. In TRIO 2.0, the following informations can be simulated and visualized: ion trajectories, the image of the beam profile, the beam envelope and the ion transmission, the TOF peak, and the energy and angular focal planes. The functions of the program are presented.

Chapter 3:

A miniature double-focusing mass spectrograph was newly designed. The system employed a double-focusing mass spectrograph using a focal plane detector to achieve a good quantitative performance. Several ion optical properties of the system was evaluated by simulations with TRIO 2.0. The features of the designed ion optical system is described in detail.

Chapter 4:

The designed ion optical system was constructed. The constructed instrument is equipped with an EI ion source, a spherical electrostatic sector, a homogeneous magnetic sector and a focal plane detector using a CCD whose size is about 5 cm. A CCD driver system and a data acquisition system was developed. Each part of the instrument are explained.

Chapter 5:

The performance of the newly constructed instrument was investigated. The 2D and 1D spectra of the residual gases, krypton and neon were observed. The energy and the angular focal planes were evaluated both experimentally and by simulation. The second-order element of the transfer matrix was measured experimentally. The mass resolution and detectable m/z range of the constructed instrument were evaluated. Moreover, the quantitative

performance was investigated. The results of the evaluations are reported.

References

- [1.1] J. J. Thomson. *Rays of Positive Electricity and Their Application to Chemical Analysis*. Longmans, Greek & Co., Ltd., 1913.
- [1.2] A. O. Nier, W. B. Hanson, A. Seiff, M. B. McElroy, N. W. Spencer, R. J. Duckett, T. C. D. Knight, and W. S. Cook. Composition and Structure of the Martian Atmosphere: Preliminary Results from Viking 1. *SCIENCE*, 193:786–788, 1976.
- [1.3] K. Biemann, J. Oro, P. Toulmin III, L. E. Orgel, A. O. Nier, D. M. Anderson, P. G. Simmonds, D. Flory, A. V. Diaz, D. R. Rushneck, and J. A. Biller. Search for Organic and Volatile Inorganic Compounds in Two Surface Samples from the Chryse Planitia Region of Mars. *SCIENCE*, 194:72–76, 1976.
- [1.4] H. B. Niemann, W. T. Kasprzak, A.E. Hedin, and N. W. Spencer. Mass spectrometric measurements of the neutral gas composition of the thermosphere and exosphere of Venus. *J. Geophys. Res.*, 85:7817–7827, 1980.
- [1.5] H. B. Niemann, S. K. Atreya, G. R. Carignan, T. M. Donahaue, J. A. Haberman, D. N. Harpold, R. E. Hartle, D. M. Hunten, W. T. Kasprzak, P. R. Mahaffy, T. C. Owen, N. W. Spencer, and S. H. Way. The Galileo Probe Mass Spectrometer: Composition of Jupiter's Atmosphere. *SCIENCE*, 272:846–849, 1996.
- [1.6] H. B. Niemann, S. K. Atreya, S. J. Bauer, K. Biemann, B. Block, G. R. Carignan, T. M. Donahaue, R. L. Frost, D. Gautire, J. A. Haberman, K. Mauersberger, T. C. Owen, F. Raulin, J. E. Richards, and S. H. Way. THE GAS CHROMATOGRAPH MASS SPECTROMETER FOR THE HUYGENS PROBE. *Space Sci. Rev.*, 104:553–591, 2002.
- [1.7] K. Birkinshaw. Fundamentals of Focal Plane Detectors. *J. Mass Spectrom.*, 32:795–806, 1997.

- [1.8] C. E. Giffin, H. G. Boettger, and D. D. Norris. AN ELECTRO-OPTICAL DETECTOR FOR FOCAL PLANE MASS SPECTROMETERS. *Int. J. Mass Spectrom. Ion Phys.*, 15:437–449, 1974.
- [1.9] J. Mattauch and R. Herzog. Über einen neuen Massenspektrographen. *Z. Phys.*, 89:786–795, 1934.
- [1.10] D. Murphy and K. Mauersberger. A HIGH SENSITIVE MASS SPECTROMETER DETECTOR SYSTEM. *Int. J. Mass Spectrom. Ion Proc.*, 76:85–93, 1987.
- [1.11] T. W. Burgoyne, G. M. Hieftje, and R. A. Hites. Design and Performance of a Plasma-Source Mass Spectrograph. *J. Am. Soc. Mass Spectrom.*, 8:307–318, 1997.
- [1.12] H. Yurimoto, K. Nagashima, and T. Kunihiro. High precision isotope micro-imaging of materials. *Appl. Surf. Sci.*, 203:793–797, 2003.
- [1.13] <http://www.isas.jaxa.jp>.
- [1.14] M. Nishiguchi, M. Toyoda, M. Ishihara, M. Ohtake, T. Sugihara, and I. Katakuse. Development of a miniature double focusing mass spectrograph using a focal plane detector. *J. Mass Spectrom. Soc. Jpn.*, 54:1–9, 2006.

Chapter 2

Computer program “TRIO 2.0” for the design of ion optical systems

2.1 Introduction

For the design of any mass spectrometer, the investigation of the ion optics is essential. In magnetic sector type instruments and time-of-flight (TOF) mass spectrometers, the spatial or time aberrations have directly influence on the performance of the ion optical system. The aberration theory for the mass spectrograph or mass spectrometer, therefore, has been investigated since late 1910s.

Aston constructed his first mass spectrograph which satisfies the energy focusing in 1919 [2.1]. Dempster designed the first 180° mass spectrograph which achieves the angular focusing in 1918 [2.2]. For the magnetic sector type instrument, Mattauch and Herzog investigated the first-order double-focusing ion optics in 1930s [2.3]. The second-order calculation of an ion trajectory was given in late 1950s by Hintenberger [2.4] and by Ewald [2.5]. To calculate the aberration coefficients of an ion optical system, transfer matrix method was introduced by Penner in 1961 [2.6]. The effect of the fringing field on the focusing properties of the magnetic sector was first investigated by Enge [2.7]. Wollnik and Ewald discussed it in the second-order [2.8]. Matsuda and Wollnik calculated it in the third-order [2.9]. Matsuo calculated the third-order aberration coefficients of the magnetic sector field [2.10] and electric sector field [2.11]. For the TOF mass spectrometer, two-stage acceleration and time-lag focusing methods were developed by Wiley and McLaren in 1955 to reduce the time aberration depending on the ion's initial energy deviation [2.12]. Mamyrin *et al* give the solution to achieve the energy focusing for the flight time by the ion mirror [2.13]. Poschenrieder proposed the isochronous focusing and space focusing by electrostatic sectors. Sakurai *et al* calculated the time aberration coefficients for a toroidal electrostatic sector and an electrostatic quadrupole lens up to third-order considering the influence of the fringing fields.

In order to calculate these aberrations, the equation of motion for ions in the ion optical

system must be solved theoretically or numerically. The computational calculation plays an important role for this purpose in recent years. There are two general methods to solve the equation of motion, i.e., to calculate an ion trajectory: one is the transfer matrix method, and the other is the ray tracing method. If the aberration coefficients for each part of the ion optical system had already presented with an available form by the theoretical investigation, the transfer matrix method is simpler and faster method than the ray tracing. Several computer programs employing the transfer matrix method had already developed. For example, “TRIO” [2.14] and “GIOS” computer programs were developed by Matsuo *et al* and by Wollnik *et al*, respectively. The computer program TRIO can calculate the image aberration coefficients including the influence of the fringing fields up to third-order. A computer program “BEIS” was developed to simulate the image shape and scanned peak shape at the detecting position [2.15]. Sakurai and Matsuo developed “TRIO-TOF” computer program to calculate the time aberration coefficients for an ion optical system consisting of electrostatic sectors and quadrupole lenses [2.16]. Toyoda and Matsuo developed “TRIO-DRAW” computer program combining TRIO, TRIO-TOF and BEIS [2.17]. The computer program TRIO-DRAW can calculate the spatial and time aberration coefficients using the transfer matrix method and make the drawing of the ion trajectories as postscript files. The program was written in FORTRAN and C languages.

Although TRIO-DRAW has several useful functions, it doesn't have the graphical user interface (GUI). Moreover, several languages of FORTRAN, C and Postscript are employed in the program. Consequently, it would be troublesome and take times to expand or add the functions in the program. Needless to say, a useful GUI give the more efficiency for the design of ion optical systems, and the expandability of the program is necessary for the future progress. Therefore, TRIO 2.0 computer program equipping GUIs was developed as improved version of TRIO-DRAW. The computer program TRIO 2.0 has the following features:

- TRIO 2.0 can calculate spatial and time aberration coefficients of an ion optical system up to third-order both in the horizontal and vertical directions. An ion optical system including the following elements can be calculated: cylindrical or toroidal electro-

static sectors, homogeneous or inhomogeneous magnetic sectors, quadrupole lenses and multipole lenses.

- TRIO 2.0 has following functions:
 - Simulation and visualization of ion trajectories
 - Simulation and visualization of beam profiles
 - Simulation and visualization of the beam envelope and the transmission
 - Simulation and visualization of the TOF peak
 - Simulation and visualization of the energy and angular focal planes

All of these functions have GUIs. These simulation results are visualized with a printable form.

- TRIO 2.0 employs a modern object oriented language of Java. All the programs are written in only Java. It brings us a high expandability, flexibility and maintainability of the coding. Moreover, it has a high compatibility for platforms, e.g., Mac OS X, Linux and Windows.

In this chapter, details of TRIO 2.0 are presented. First, the principle of the transfer matrix method is described. Then, the functions of TRIO 2.0 are presented.

2.2 Transfer matrix method

In the transfer matrix method, the geometrical trajectory of an arbitrary particle is expressed by an ion optical position vector $\mathbf{P}(x, \alpha, y, \beta, \gamma, \delta)$. Here x and α denote the positional and angular deviations of the arbitrary trajectories in the horizontal direction, and y and β denote the same ones in the vertical direction. They are defined with respect to the optic axis, which is the trajectory of a reference ion of mass m_0 , charge e_0 and energy U_0 . The mass and energy deviations, γ and δ , are defined as

$$m/e = (m_0/e_0)(1 + \gamma), \quad U/e = (U_0/e_0)(1 + \delta) \quad (2.1)$$

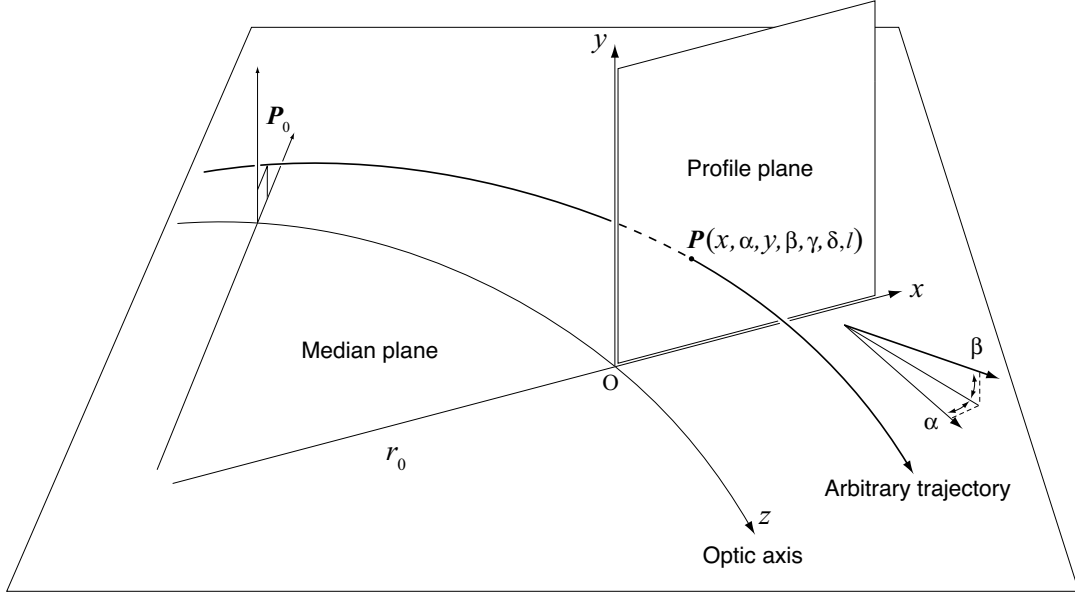


Figure 2.1: Coordinate system for the ion optical position vector

where m , e , U are the mass, charge, and energy of an arbitrary ion. The coordinate system for the ion optical position vector is shown in Figure 2.1.

The parameters of the ion optical position vector at an arbitrary profile plane could be given with a form of the expansion into power series of the initial parameters at the initial profile plane by solving the equation of motion. For example, the parameter of x is expressed as follows:

$$\begin{aligned}
x = & (x|x)x_0 + (x|\alpha)\alpha_0 + (x|\gamma)\gamma + (x|\delta)\delta \\
& + (x|xx)x_0^2 + (x|x\alpha)x_0\alpha_0 + (x|x\gamma)x_0\gamma + (x|x\delta)x_0\delta + (x|\alpha\alpha)\alpha_0^2 + (x|\alpha\gamma)\alpha_0\gamma + (x|\alpha\delta)\alpha_0\delta \\
& + (x|yy)y_0^2 + (x|y\beta)y_0\beta_0 + (x|\beta\beta)\beta_0^2 + (x|\gamma\gamma)\gamma^2 + (x|\gamma\delta)\gamma\delta + (x|\delta\delta)\delta^2 \\
& + (\text{third order terms})
\end{aligned} \tag{2.2}$$

The parameters of α , y and β are expressed as the same form. The parameters of γ and δ are generally conserved. In the first-order approximation, the relation between the position vector $\mathbf{P}(x, \alpha, y, \beta, \gamma, \delta)$ at an arbitrary profile plane and an initial position vector $\mathbf{P}_0(x_0, \alpha_0, y_0, \beta_0, \gamma, \delta)$

is expressed as the following form of a matrix:

$$\begin{pmatrix} x \\ \alpha \\ y \\ \beta \\ \gamma \\ \delta \end{pmatrix} = \begin{pmatrix} (x|x) & (x|\alpha) & 0 & 0 & (x|\gamma) & (x|\delta) \\ (\alpha|x) & (\alpha|\alpha) & 0 & 0 & (\alpha|\gamma) & (\alpha|\delta) \\ 0 & 0 & (y|y) & (y|\beta) & 0 & 0 \\ 0 & 0 & (\beta|y) & (\beta|\beta) & 0 & 0 \\ 0 & 0 & 0 & 0 & 1 & 0 \\ 0 & 0 & 0 & 0 & 0 & 1 \end{pmatrix} \begin{pmatrix} x_0 \\ \alpha_0 \\ y_0 \\ \beta_0 \\ \gamma \\ \delta \end{pmatrix} \quad (2.3)$$

This matrix is called as transfer matrix, and the elements of the transfer matrix are called as transfer coefficients or aberration coefficients. Some aberration coefficients are equal to zero because of the symmetry of the field distribution relative to the median plane. Hereinafter, each element of the transfer matrix, e.g., the element in row x and in column α is denoted as $(x|\alpha)$. The transfer matrix shows the action of the field. Once the transfer matrix for each field is given with the analytical form, the transfer matrix for the same type of the field can be easily derived by assigning the physical parameters of the field from then on. Moreover, the total transfer matrix of an ion optical system can be determined as the product of the matrices of the individual components. That is, the total transfer matrix \mathbf{T} is given as follows.

$$\mathbf{T} = \mathbf{T}_n \times \mathbf{T}_{n-1} \times \cdots \times \mathbf{T}_2 \times \mathbf{T}_1 \quad (2.4)$$

Here, T_i shows the transfer matrix of the i th component in the order which ions will pass through.

In case of TOF mass spectrometers, the parameter l of the path length deviation is introduced to the ion optical parameters. The path length deviation l is defined relative to the path length of the reference ion as:

$$l = \int_0^s \frac{v_0}{v} dz - \int_0^s dz \quad (2.5)$$

where v_0 and v are the velocity of the reference and an arbitrary ion. A line element dz is along the optic axis. If an ion has a positive value of the path length deviation at an arbitrary profile plane, it means that the ion has the longer flight path than the reference ion, i.e., the ion will pass through the profile plane late from the reference ion, and vice versa. The flight time deviation t is derived from the path length deviation as $t = l/v_0$. Then the time focusing

conditions of the system can be evaluated by the path length deviation. The transfer matrix is then expanded as follows:

$$\begin{pmatrix} x \\ \alpha \\ y \\ \beta \\ \gamma \\ \delta \\ l \end{pmatrix} = \begin{pmatrix} (x|x) & (x|\alpha) & 0 & 0 & (x|\gamma) & (x|\delta) & 0 \\ (\alpha|x) & (\alpha|\alpha) & 0 & 0 & (\alpha|\gamma) & (\alpha|\delta) & 0 \\ 0 & 0 & (y|y) & (y|\beta) & 0 & 0 & 0 \\ 0 & 0 & (\beta|y) & (\beta|\beta) & 0 & 0 & 0 \\ 0 & 0 & 0 & 0 & 1 & 0 & 0 \\ 0 & 0 & 0 & 0 & 0 & 1 & 0 \\ (l|x) & (l|\alpha) & 0 & 0 & (l|\gamma) & (l|\delta) & 1 \end{pmatrix} \begin{pmatrix} x_0 \\ \alpha_0 \\ y_0 \\ \beta_0 \\ \gamma \\ \delta \\ l_0 \end{pmatrix} \quad (2.6)$$

The ion optical characteristics of the system could then be investigated by the total transfer matrix. For example, the focusing conditions of the ion optical system will be discussed about the corresponding aberration coefficients of the total transfer matrix.

2.3 Computer program TRIO 2.0

For the design and evaluation of ion optical systems, TRIO 2.0 computer program equipment was developed. The program can calculate the aberration coefficients up to third-order for an ion optical system including drift spaces, electrostatic sectors, magnetic sectors, electric or magnetic quadrupole lenses, and multipole lenses. In addition, it has several useful functions to evaluate the ion optical system. Ion trajectories, a profile of the ion beam, the beam envelope and the transmission, and the TOF peak can be simulated and visualized in TRIO 2.0. A screenshot running TRIO 2.0 is shown in Figure 2.2. Each functions are presented in the following subsections.

2.3.1 Main frame

For the design of an ion optical system, first, each component of the ion optical system and its physical parameters, e.g., the length of a drift space, the mean radius and the deflection angle of an electric or magnetic sector, the field strength of a quadrupole lens, etc, must be determined. In TRIO 2.0, the selection of the ion optical component and the setting of its physical parameters are easily carried out via the main frame. The calculated transfer matrix

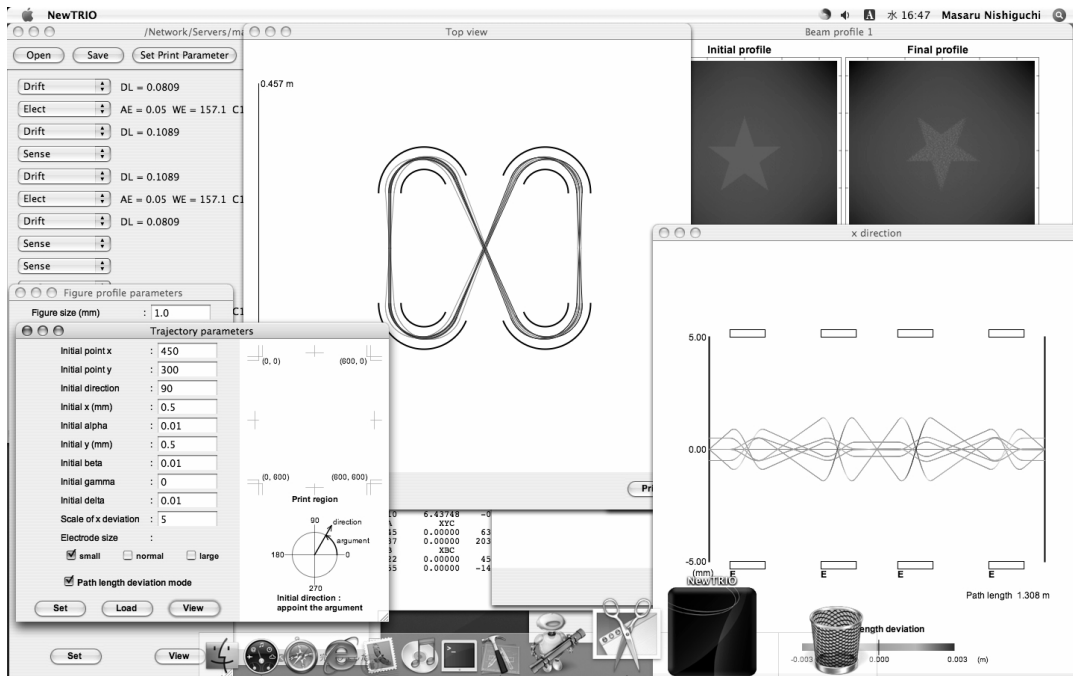


Figure 2.2: Screenshot of TRIO2.0

is shown in a window as a text date. A screenshot of the main frame and the output window is shown in Figure 2.3(a). In the main frame, an ion optical component can be selected from the pulldown menu. Then, its physical parameters are set through a dialog box. As an example, the dialog box to set parameters for a electric sector is shown in Figure 2.3(b). The physical parameters for each ion optical component are same as TRIO. The definition of the parameters are presented in ref. [2.14]. In the pulldown menu, a menu of simplex supplies a function for the parameter search by the simplex method. In many cases for designing an ion optical system, it is required that the system will satisfy several focusing conditions. For this purpose, arbitrary physical parameters of an ion optical components will be optimize to fulfill the required focusing conditions by the parameter search function. The program “MSPLEX” for the parameter search employing the simplex method was already developed by Ishihara [2.18], and it was transported to TRIO 2.0. The parameters being optimized for required focusing conditions can be chosen in the parameter setting dialog. The buttons in the upper side of the main frame supply the each function to evaluate the ion optical system.

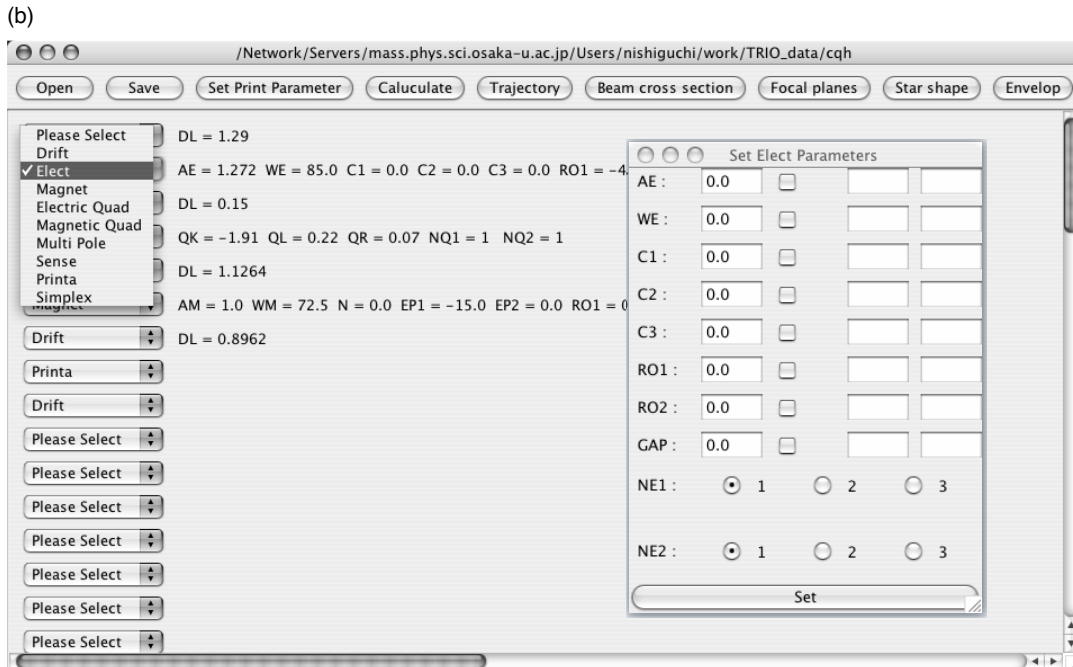
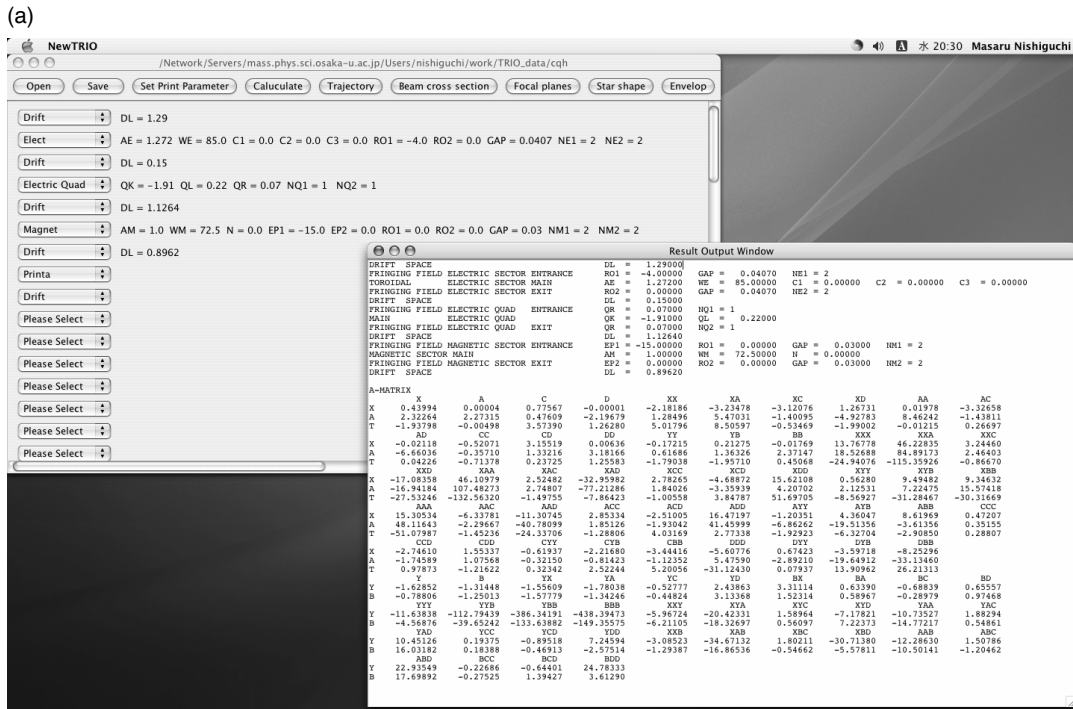


Figure 2.3: Screen shot of the main frame of TRIO 2.0. (a) The main frame and the output window, and (b) the pulldown menu of the main frame and a dialog box for setting physical parameters of a electric sector

2.3.2 Simulation and visualization of ion trajectories

Ion trajectories in an ion optical system can be simulated and visualized. The modes for the visualization of ion trajectories are same as TRIO-DRAW. When the “Trajectory” button in the main frame is clicked, a window will appear for the simulation and the visualization of ion trajectories. A screenshot of the window for ion trajectories is shown in Figure 2.4. Initial point and direction should be set to draw ion trajectories. Ion trajectories are visualized in three display modes, i.e., top view, x -direction and y -direction for each initial condition of x_0 , α_0 , y_0 , β_0 , γ and δ with different colors. Top view mode shows a plane view of ion trajectories. The display modes of x -direction and y -direction represent ion trajectories as the optic axis will be drawn in a straight line. Although TRIO 2.0 can calculate the transfer matrix up to third-order, ion trajectories are simulated in first-order because the first-order focusing conditions are the most interesting features for a ion optical system. The third-order calculation of ion trajectories is supplied at another function in TRIO 2.0. By the visualization of ion trajectories, the focusing properties of a ion optical system can be clearly realized. As a example, ion trajectories of QHQHC (quadrupole, quadrupole, homogeneous magnetic sector, quadrupole, and cylindrical electric sector) type mass spectrometer called as “GEMMY” [2.19] are shown in Figure 2.5. From the ion trajectories, it can be visually found that the energy and angular focusing called as double focusing is fulfilled in the ion optical system.

For a TOF mass spectrometer, the path length deviation can be calculated for each initial condition. When the check box is checked in the window to set the parameters for ion trajectories, the path length deviation mode is available. The path length deviation at an arbitrary profile plane is expressed by the hue for each trajectory. An advanced and retarded trajectories are colored red and blue, respectively. If the color of a trajectory is green at the final profile plane, it indicates that the trajectory focusing in time. Here, an example of the path length deviation mode is shown in Figure 2.6. The path length deviations in a TOF mass spectrometer called as “MULTUM II” are simulated in Figure 2.6.

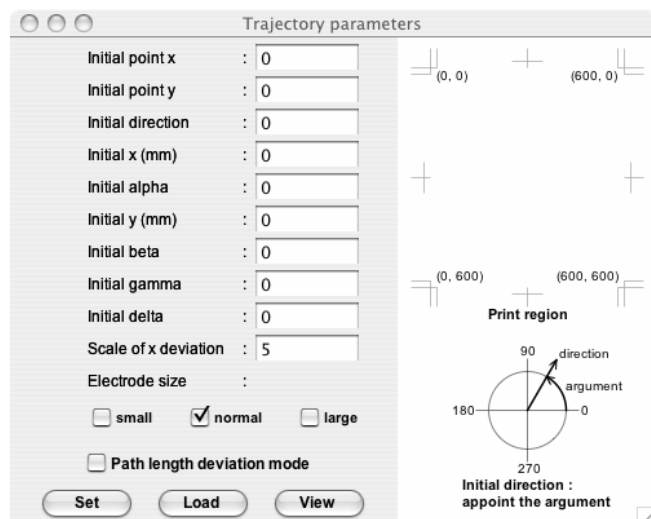


Figure 2.4: Window for the simulation and visualization of ion trajectories

2.3.3 Simulation and visualization of the image of the beam profile

Although the image shape in only x -direction was calculated by TRIO-DRAW, the divergence of an ion beam in y -direction and the image of beam profile are significant information to estimate the beam acceptance and the required detector size. In TRIO 2.0, the image of the beam profile can be simulated in third-order. When the “Beam profile” or the “Star shape” button in the main frame is clicked, a window will appear for the simulation and the visualization of the beam profile. The windows for the beam profile are shown in Figure 2.7.

Two types of initial beam shape can be simulated, i.e., a normal rectangular slit and a star-shaped slit are supplied. In the case of the normal rectangular slit, the width and height of main slit and those of the second slit, e.g., α slit, the hole of a field shunt, etc. should be set. The ion’s initial parameters of x_0 and y_0 are chosen so that the ion beam would pass through the main slit uniformly. From the two slit sizes and the first drift length, the parameters of α_0 and β_0 are generated by the random number in the range of appointed maximal value so as to satisfy the beam acceptance at the second slit. In addition, the angle between the detecting plane and the optic axis can be varied for a mass spectrograph. The simulated image of the beam profile and the peak shape are shown in a window. The peak width (10% valley) and the mass resolution are also calculated and shown in the window. Here, a simulation result

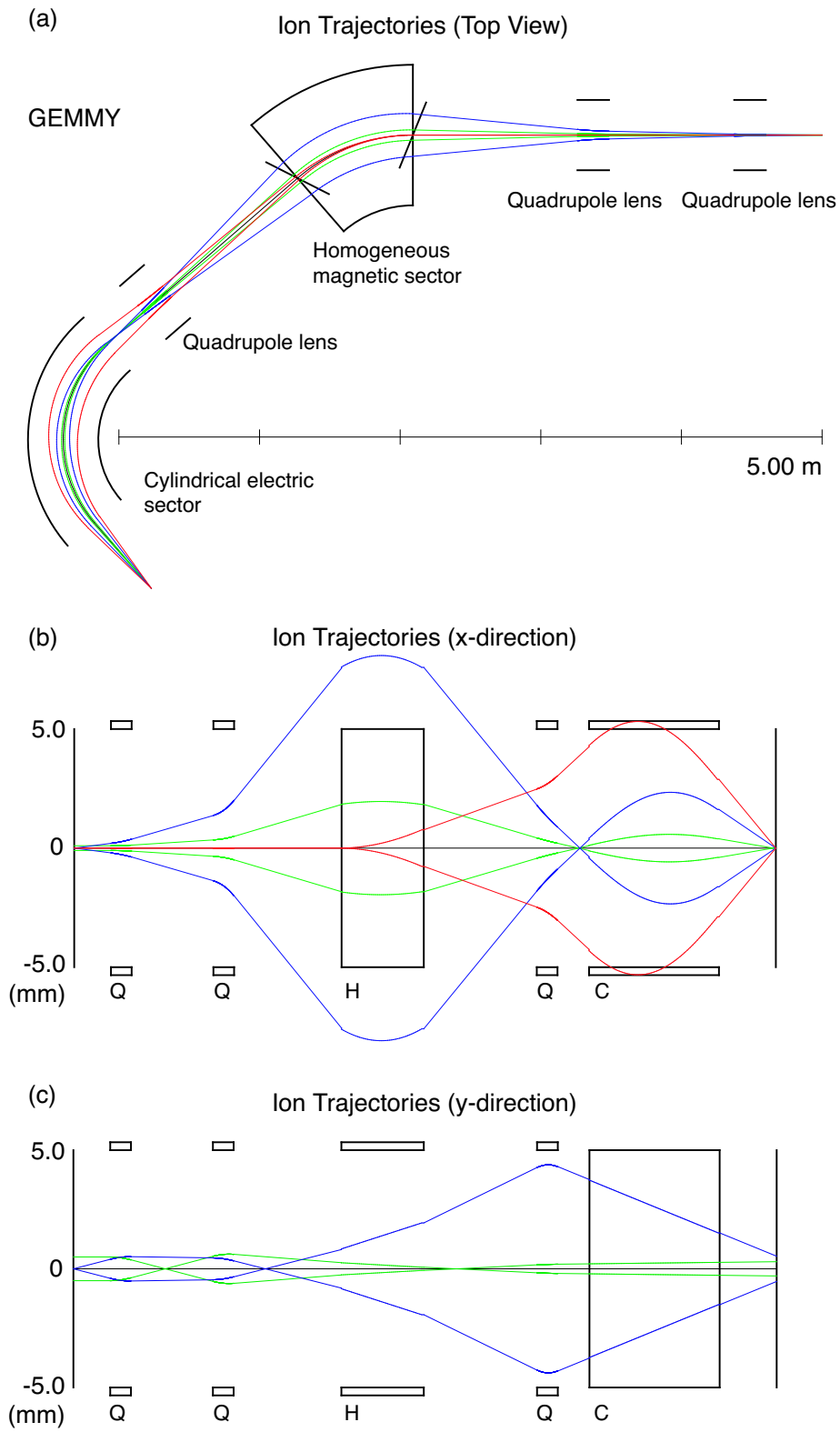


Figure 2.5: Ion trajectories in GEMMY. The display modes of (a) Top view, (b) x -direction, and (c) y -direction are shown.

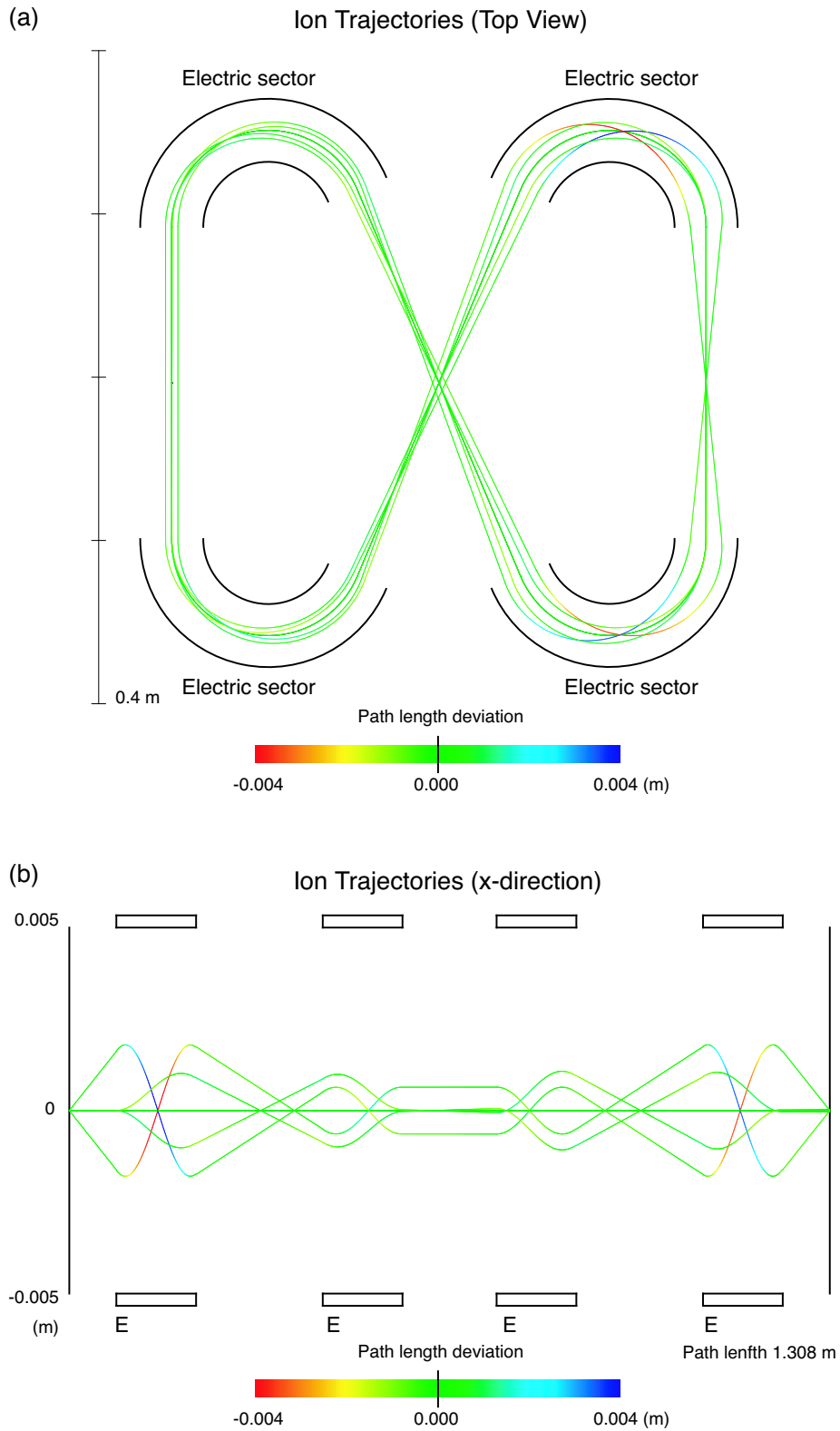


Figure 2.6: Ion trajectories in the path length deviation mode. Ion trajectories in MULTUM II are simulated. (a) Top view and (b) x -direction are shown.

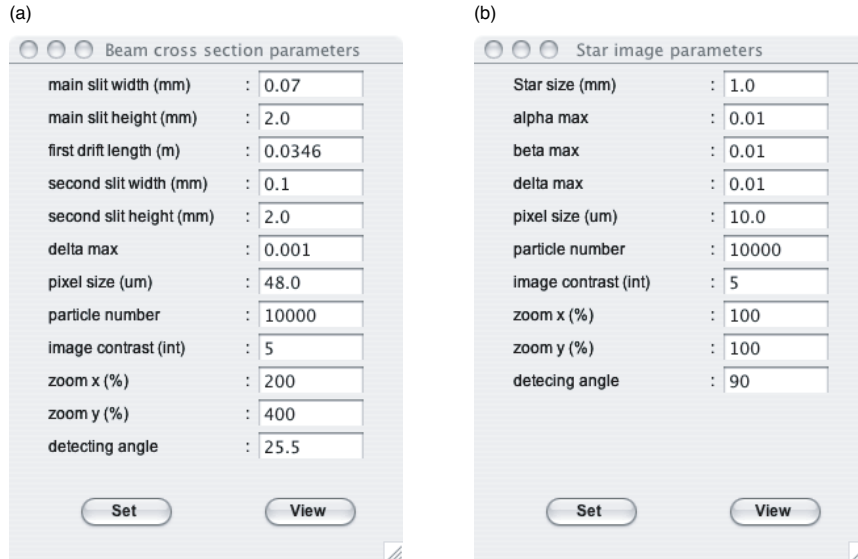


Figure 2.7: Window for the simulation and visualization of the beam profile. The shape of initial images can be chosen from (a) a rectangular slit and (b) a star shape.

of the CQH-type mass spectrometer [2.20] is shown in Figure 2.8.

From the simulation of the star-shaped slit, the deformation of the beam profile after passing through the system can be clearly found. A simulated image of the star-shaped slit in MULTUM II is shown in Figure 2.9. The size of the star-shaped slit is 1 mm. Since the ion optical system of MULTUM II satisfies the perfect focusing [2.21], the initial star-shaped image is conserved after one cycle of the ion optical system. The final image is inverse in both x - and y -direction relative to the initial image because of the image magnification values of $(x|x) = -1$ and $(y|y) = -1$.

2.3.4 Simulation and visualization of the beam envelope and the ion transmission

For any mass analyzer, the sensitivity is an important property. Accordingly the ion transmission or the beam acceptance should be evaluated in the design of the system. The program BEIS and TRIO-DRAW could only visualize the rough beam envelope from a few ion trajectories with each initial condition. In TRIO 2.0, the functions to visualize the beam envelope and evaluate the ion transmission are significantly improved and newly added. When the

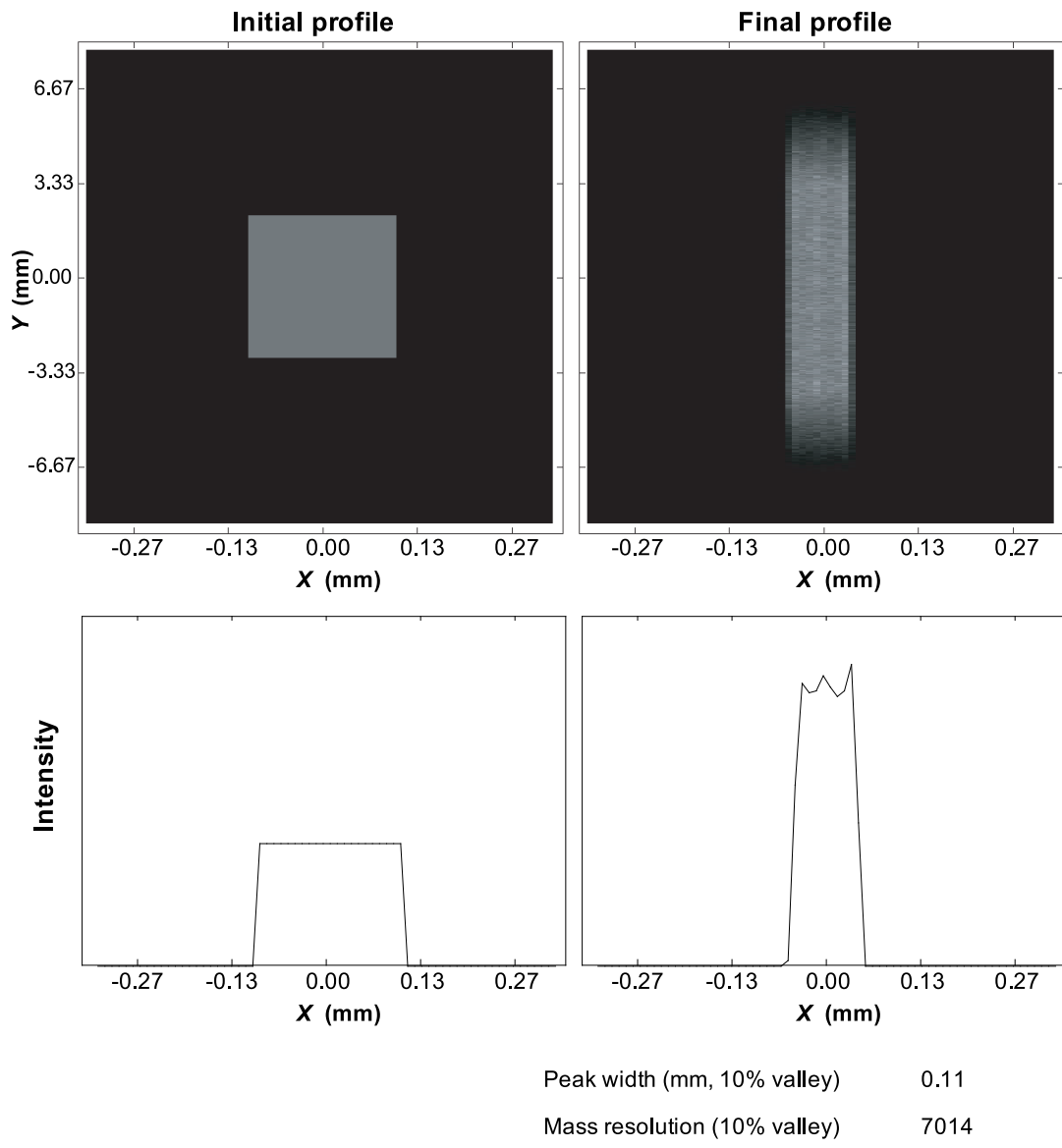


Figure 2.8: Image of the beam profile and the peak shape of CQH-type mass spectrometer

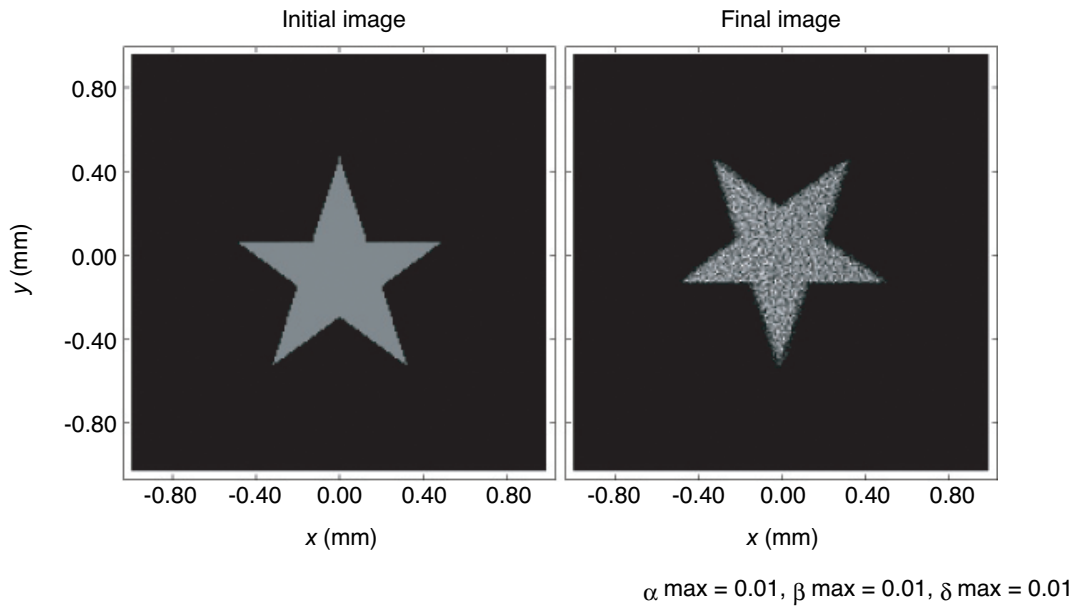


Figure 2.9: A simulated image of the star-shaped slit in MULTUM II

“Envelop” button in the main frame is clicked, a window to set the parameters will appear for these functions.

The program TRIO 2.0 can calculate ion trajectories for many particles with each initial condition generated by the random number in third-order. In addition, the collision with each ion optical component are judged for each ion trajectory every determined steps. For example, the collision when an ion is passing through an electric sector is judged as follows: if the deviation x of the ion trajectory would become larger than the half gap width of the electric sector, it was judged that the ion would collide with the electric sector. The ion transmission is defined as the ratio of the number of the ions passing through the whole system without the collision and the number of total number of ions.

Furthermore, TRIO 2.0 can accept the multi-turn ion optical systems. In recent years, several types of multi-turn TOF mass spectrometers were developed and established its high resolving power. For a multi-turn ion optical system, the beam envelope for the overall flight path should be evaluated to estimate its ion transmission. By appointing the cycle number in the parameter setting window, the beam envelope in a multi-turn ion optical system can be simulated and visualized. As an example, the beam envelope in the MULTUM II is shown

in Figures 2.10 and 2.11. The ion trajectories of 1000 particles are simulated. Figure 2.10(a) and (b) show beam envelopes for one cycle in x - and y - direction, respectively. In Figure 2.11 those for 5 cycles are shown.

From this function, the beam envelope for the overall flight path can be easily simulated and visualized. In addition, the ion transmission can be calculated simultaneously. These evaluations are necessary for the design of any mass analyzer.

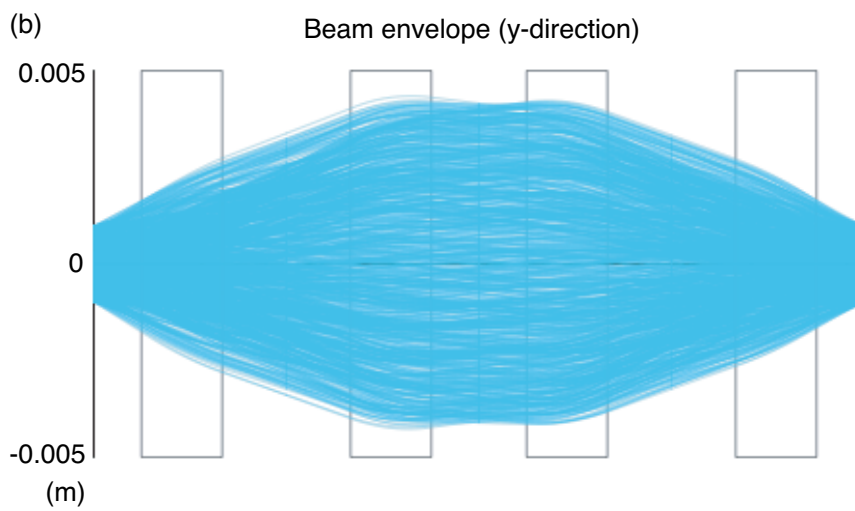
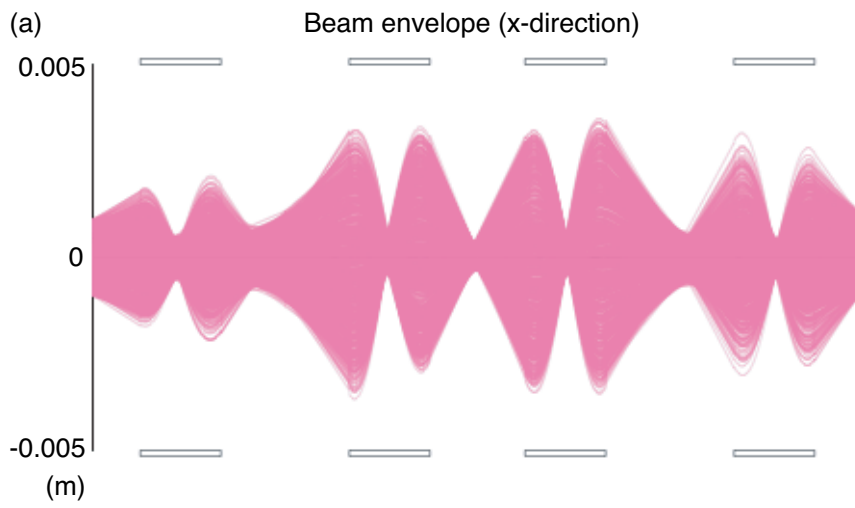
2.3.5 Simulation and visualization of the TOF peak

For the TOF mass spectrometers, the TOF peak can be simulated and visualized in third-order. In the menu bar of the parameter setting window for the beam envelope, the “Tool” menu is equipped. When the item of “TOF peak” in the “Tool” menu is selected, a window to set the parameters for the simulation of the TOF peak will appear. A screenshot of the parameter setting window for the TOF peak simulation is shown in Figure 2.12. A TOF peak simulation of MULTUM II is shown in Figure 2.13. The peak width (FWHM) and the mass resolution are also calculated and shown simultaneously.

2.3.6 Simulation and visualization of the energy and angular focal planes

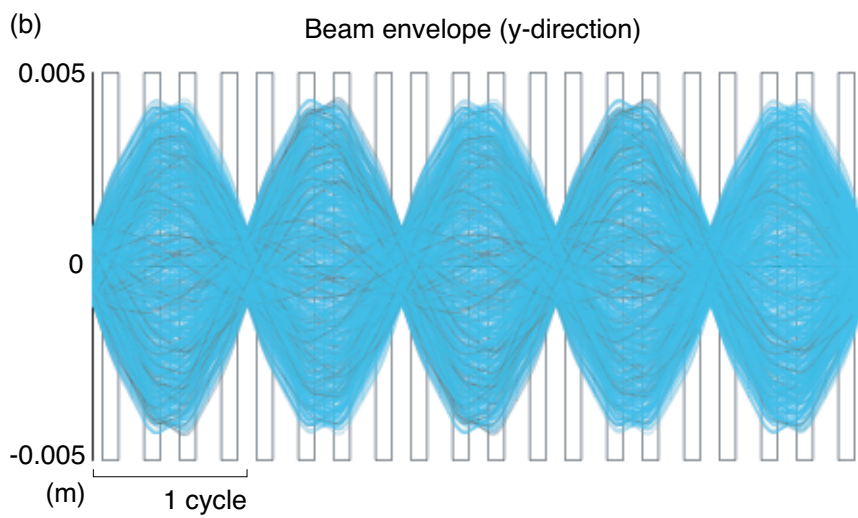
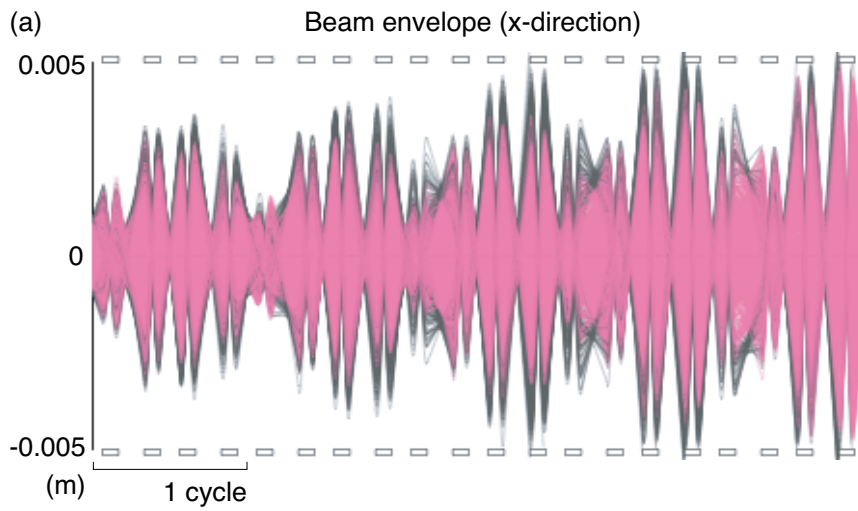
The configurations of the energy and angular focal planes are the principal ion optical properties for a double focusing mass spectrograph. The energy and angular focal planes can be simulated in third-order. When the “Focal planes” button in the main frame is clicked, a window to set the parameters for the simulation of the focal planes will appear. In this function, the energy and angular focusing points are calculated for ion trajectories of each value of the mass deviation γ . In Figure 2.14, the parameter setting window for the simulation of the focal planes is shown. A simulation result of the energy and angular focal planes of GEMMY is shown in Figure 2.15.

In this ion optical system, it is found that the energy and angular focal planes are not consistent with each other, and the double-focusing is satisfied at only one point.



x_0 max	1.0 mm	
α_0 max	0.01	1000 particles
y_0 max	1.0 mm	1 cycle
β_0 max	0.01	Path length 1.308 m
δ max	0.01	Ion transmission 100%

Figure 2.10: Beam envelope for 1 cycle in MULTUM II



x_0 max	1.0 mm	
α_0 max	0.01	1000 particles
y_0 max	1.0 mm	5 cycles
β_0 max	0.01	Path length 6.538 m
δ max	0.01	Ion transmission 87%

Figure 2.11: Beam envelope for 5 cycles in MULTUM II

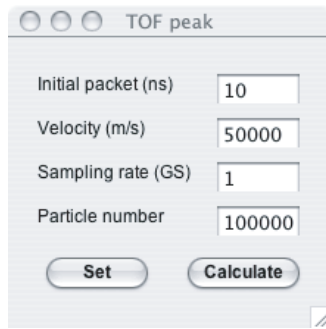


Figure 2.12: Window for the TOF peak simulation and visualization

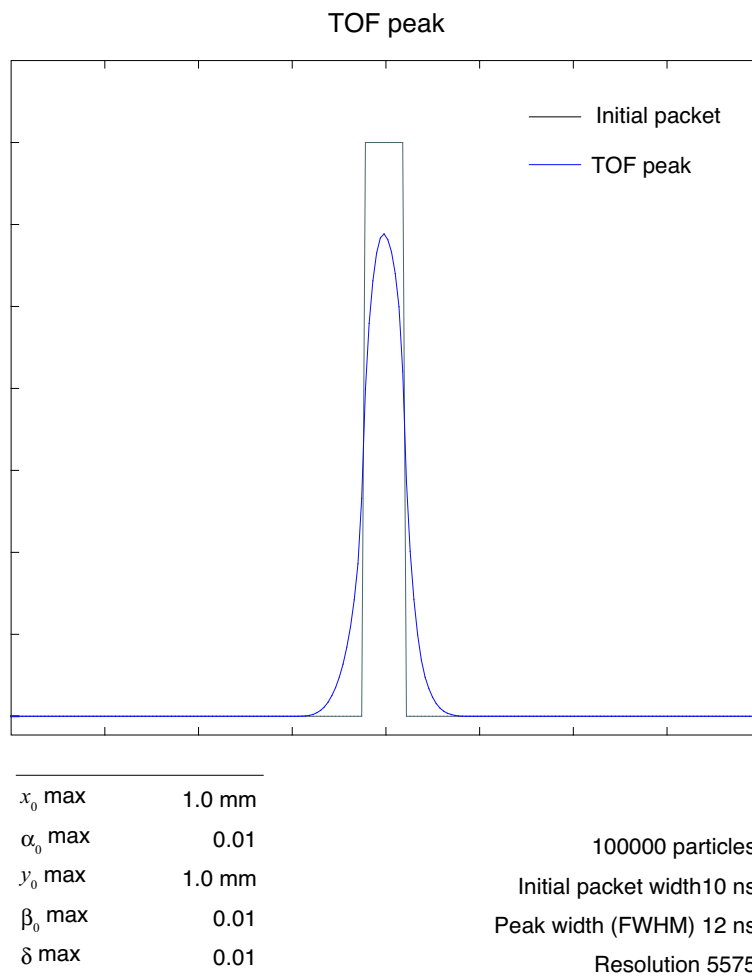


Figure 2.13: Simulated TOF peak after 5 cycles in MULTUM II

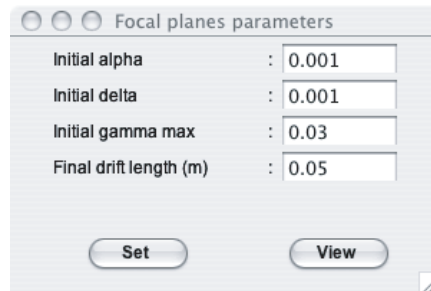


Figure 2.14: Window for the focal plane simulation and visualization

2.4 Conclusion

The computer program TRIO 2.0 equipping GUIs was developed for the design of ion optical systems. The program has many useful functions to evaluate the ion optical properties of a system. In TRIO 2.0, the following informations can be simulated and visualized: ion trajectories, the image of the beam profile, the beam envelope and the ion transmission, the TOF peak, and the energy and angular focal planes. This program enables us to design a high resolution and a high sensitive mass analyzer.

References

- [2.1] F. W. Aston. A positive-ray spectrograph. *Phil. Mag.*, 38:707–715, 1919.
- [2.2] A. J. Dempster. A NEW METHOD OF POSITIVE RAY ANALYSIS. *Phys. Rev.*, 11:316–325, 1918.
- [2.3] J. Mattauch and R. Herzog. Über einen neuen Massenspektrographen. *Z. Phys.*, 89:786–795, 1934.
- [2.4] H. Hintenberger and L. A. K. Über die Bildfehler in doppelfokussierenden Massenspektrometern und Massenspektrographen. *Z. Naturf.*, 12a:140–147, 1957.
- [2.5] H. Ewald and H. Liebl. Die Bilfehler des Troidkondensators. *Z. Naturf.*, 12a:28–33, 1957.

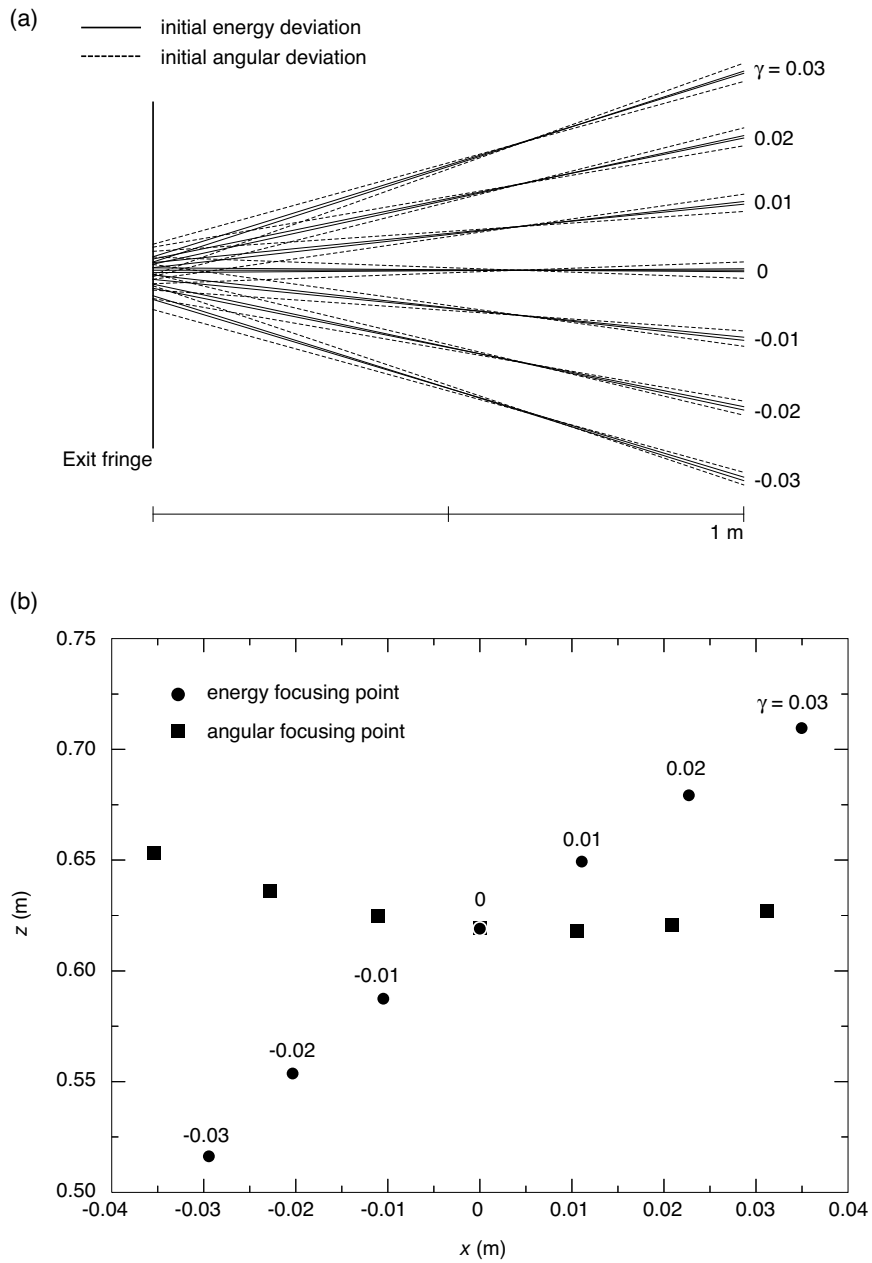


Figure 2.15: Simulation of the focal planes of GEMMY. (a) Ion trajectories with the initial energy and angular deviations for each value of γ and (b) the expanded plot of the energy and angular focusing points for each value of γ are shown.

- [2.6] S. Penner. Calculations of Properties of Magnetic Deflecting Systems. *Rev. Sci. Instrum.*, 32:150–160, 1961.
- [2.7] H. Enge. Effect of Extended Fringing Fields on Ion-Focusing Properties of Deflecting Magnets. *Rev. Sci. Instrum.*, 35:278–287, 1964.
- [2.8] H. Wollnik and H. Ewald. The influence of magnetic and electric fringing fields on trajectories of charged particles. *Nucl. Instrum. Methods*, 36:93–104, 1965.
- [2.9] H. Matsuda and H. Wollnik. Third order transfer matrices of the fringing field of an inhomogeneous magnet. *Nucl. Instrum. Methods*, 77:283–292, 1970.
- [2.10] T. Matsuo and H. Matsuda. THIRD ORDER CALCULATION OF THE ION TRAJECTORIES IN AN INHOMOGENEOUS MAGNETIC SECTOR FIELD. *Int. J. Mass Spectrom. Ion Phys.*, 6:361–383, 1971.
- [2.11] T. Matsuo and H. Matsuda. PARTICLE TRAJECTORIES IN A TOROIDAL CONDENSER CALCULATED IN A THIRD ORDER APPROXIMATION. *Nucl. Instrum. Methods*, 103:515–532, 1972.
- [2.12] W. C. Wiley and I. H. McLaren. Time-of-Flight Mass Spectrometer with Improved Resolution. *Rev. Sci. Instrum.*, 26:1150–1157, 1955.
- [2.13] V. I. Kartaev, B. A. Mamyrin, and D. V. Shmikk. New method for focusing ion bunches in time-of-flight mass spectrometers. *Sov. Phys. Tech. Phys.*, 16:1177–1179, 1972.
- [2.14] T. Matuo, H. Matsuda, Y. Fujita, and H. Wollnik. Computer Program “TRIO” for Third Order Calculation of Ion Trajectory. *Mass Spectroscopy (Japan)*, 24:19–62, 1976.
- [2.15] T. Matuo, T. Sakurai, H. Matsuda, and H. Nakabushi. Computer Program “BEIS” for Estimation of Beam Envelop and Image Shape of an Ion Optical System. *Mass Spectroscopy (Japan)*, 33:261–270, 1985.
- [2.16] T. Sakurai and T. Matsuo. Computer Code “TRIO-TOF” for the Third Order Calculation of Ion Flight Times. *J. Mass Spectrom. Soc. Jpn.*, 46:437–441, 1998.

- [2.17] M. Toyoda and T. Matuo. Computer Program “TRIO-DRAW” for displaying ion trajectory and flight time. *Nucl. Instrum. Methods A*, 427:375–381, 1999.
- [2.18] M. Ishihara. *Ion optical study of mass spectrometers*. PhD thesis, Osaka University, 1991.
- [2.19] H. Matsuda, T. Matsuo, Y. Fujita, and T. Sakurai. A NEW MASS SPECTROMETER AT OSAKA UNIVERSITY. *Int. J. Mass Spectrom. Ion Proc.*, 91:1–10, 1989.
- [2.20] H. Matsuda. DOUBLE FOCUSING MASS SPECTROMETERS OF SECOND ORDER. *Int. J. Mass Spectrom. Ion Phys.*, 14:219–233, 1974.
- [2.21] M. Ishihara, M. Toyoda, and T. Matsuo. Perfect space and time focusing ion optics for multiturn time of flight mass spectrometers. *Int. J. Mass Spectrom.*, 197:179–189, 2000.

Chapter 3

Design of a miniature double-focusing mass spectrograph

3.1 Introduction

For a lunar exploration, an ion optical system was newly designed [3.1]. The system employed a double-focusing mass spectrograph due to its high sensitivity and good quantitative performance. An instrument loading on a space probe would be restricted its size, weight, and power consumption. The instrument must be design within these imposed restrictions. In this chapter, the newly designed ion optical system is described. Moreover, results of simulations to evaluate the designed ion optical system were presented. The computer program TRIO 2.0 described in the previous chapter was applied for these simulations.

3.2 Design concept

As already described in chapter 1, a lunar surface exploration using a mass spectrometric instrument was planned. The instrument would be carried on a rover and the surface substances would be analyzed on site. As the measuring objects, ices in the poles and noble gases from He to Ar in the surface regolith and rocks were considered. Accordingly, the mass range of the measurements was set from 1 u to 50 u. The mass resolution of 500 is required to resolve HD and ^3He . This is essential to measure the isotope ratio of He. The dynamic range of 10^4 are required for the measurement of the isotope ratios of Ar. As a typical instrument for loading on a rover, following specifications are considered: the size of the mass analyzer must be less than $200 \times 150 \times 100$ mm; the weight must be less than 3 kg. A schematic diagram of the mass spectrometric system for a lunar exploration is shown in Figure 3.1. In this system, samples are loaded into the sample box by a manipulator equipped in the rover. The samples are heated in the box and gases from the samples are transported to a gas purification part, e.g., GC, getter pump, etc. Then, the objective gases are introduced to

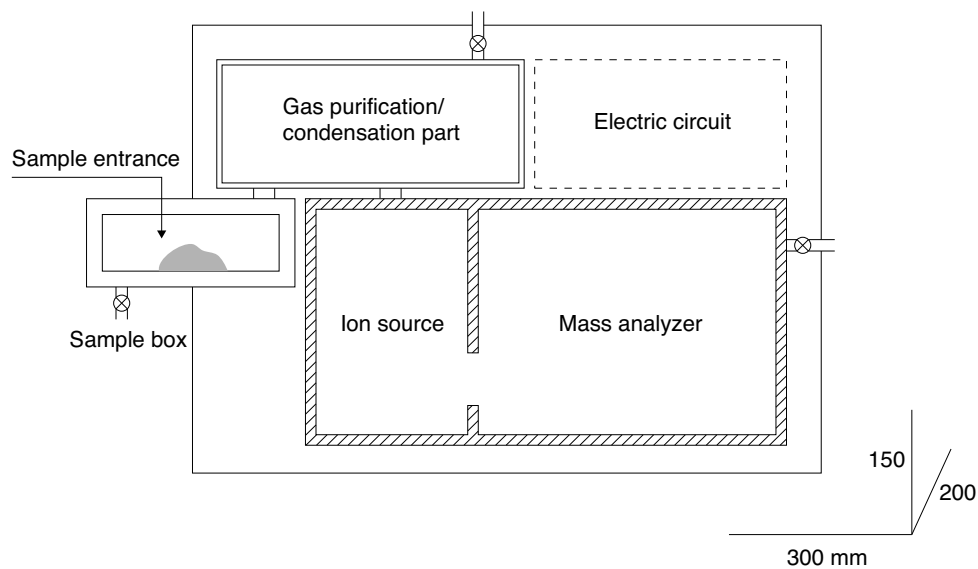


Figure 3.1: Schematic diagram of the mass spectrometric system

the ion source.

As already explained, a magnetic sector-type instrument, which may have the advantage of a good quantitative performance, can be available for planetary explorations that would be near the Earth, e.g., lunar or Mars explorations. A magnetic sector-type was, therefore, employed as the mass analyzer. Magnetic sector-type analyzers are classified in mass spectrographs and mass spectrometers. The typical ion optical system of the mass spectrometer is the Nier-Johnson geometry [3.3]. A schematic drawing of the Nier-Johnson geometry is shown in Figure 3.3. It consists of a cylindrical electrostatic sector and a homogeneous magnetic sector. The Nier-Johnson geometry provides only one double focusing point, i.e., the energy focal plane and the angular focal plane intersect at one point. On the other hand, the typical ion optical system for the mass spectrograph is the Mattauch-Herzog geometry [3.2]. A schematic drawing of the ion optical systems of the Mattauch-Herzog geometry is shown in Figures 3.2. Both of them consist of a cylindrical electrostatic sector and a homogeneous magnetic sector, and they satisfy the double-focusing. The Mattauch-Herzog geometry provides the double focusing on a straight line at the exit of the magnet. This is ideal for the use of a focal plane detector. Since a mass spectrograph can simultaneously detect all the ions that pass through the analyzer, it has dramatically better detection efficiency. Furthermore,

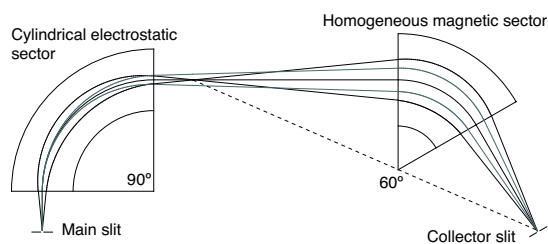


Figure 3.2: Schematic drawing of the Nier-Johnson geometry

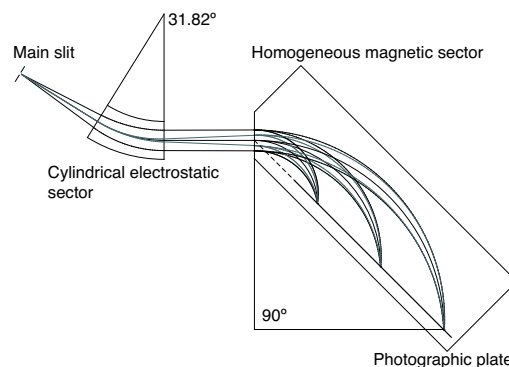


Figure 3.3: Schematic drawing of the Mattauch-Herzog geometry

quantitative performance can be improved by simultaneous detection, since time-dependent fluctuations of the system are eliminated. For these reasons, a mass spectrograph that employs a focal plane detector is suited in principle for trace and quantitative analysis. Therefore an ion optical system based on the Mattauch-Herzog geometry was newly designed for a lunar exploration.

3.3 Design of a miniature double-focusing mass spectrograph

In the design, the following two conditions are considered:

- The ion beams must be parallel rays in the drift space between the electrostatic sector and the magnetic sector.
- Both the energy and angular focal planes must be placed at a distance from the exit of the magnet.

The first condition is theoretically required to realize a straight line for double focusing [3.2]. This condition can be easily fulfilled by adjusting the length of the first drift space between the ion source and the electrostatic sector. The second condition is needed to mount an MCP-based position sensitive detector on the mass analyzer. In the original Mattauch-Herzog design, where the photographic plate was used, the focal planes are placed at the exit fringe of the magnetic sector as shown in Figure 3.2. However, to install an MCP-based position

sensitive detector, it is desirable that the focal planes be at a distance from the exit fringe of the magnetic sector. For this purpose, the defocusing action of the fringing fields of the magnetic sector can be available. The fringing field of the magnet will exert a defocusing action in the horizontal direction if the inclination angle between the incident normal of the field boundary and the optical axis is positive [3.4]. Therefore, the second condition can be fulfilled with a positive inclination angle at the magnet entrance.

A spherical electrostatic sector is employed in the ion optical system. The spherical electric field exerts focusing actions both in the vertical and horizontal directions. The focusing action in the vertical direction contributes to achieving high transmission in the magnetic sector. The mean radius of the spherical electrostatic sector is 50 mm.

In the design of a mass spectrograph, the magnetic sector is the most important part, since it is the heaviest part, and the detectable range of mass to charge ratio (m/z) depends on the size of the magnet. Here, the detectable m/z range is defined as the ratio of the maximal to the minimal observable m/z . It is expressed in terms of the maximal radius r_{\max} and the minimal radius r_{\min} of the trajectories in the magnetic field as $(r_{\max}/r_{\min})^2$. Accordingly, in order to achieve a wide range of detectable m/z , the maximal radius should be increased, or the minimal radius should be decreased. The maximal radius, however, directly depends on the magnet size; thus, it is limited. The minimal radius is also limited. Because the magnetic field would not be homogeneous in the region of the magnet fringe, the minimal radius must be sufficiently larger than the gap width between the pole pieces. In this instrument, the maximal radius and the minimal radius are 75 mm and 25 mm, respectively. In this design, the detectable m/z range of 7 is sufficiently achieved. If it is required to detect from 1 u to 49 u, the observed mass region can be altered by switching the accelerating voltage and the field strength of the electrostatic sector. When low mass ions from 1 u to 7 u are observed at a high accelerating voltage V_h , the high mass ions from 7 u to 49 u can be observed at a low accelerating voltage $V_l = V_h/7$.

The design of the ion optical system was carried out with the computer programs TRIO-DRAW and TRIO 2.0.

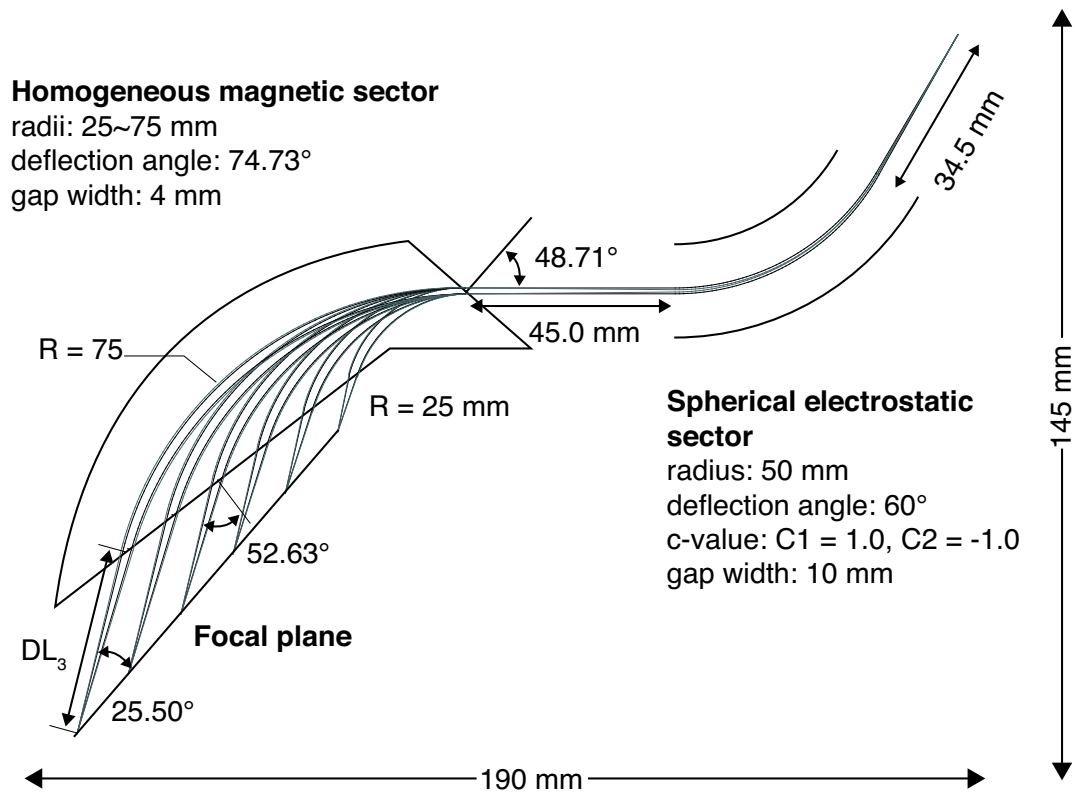


Figure 3.4: Ion optical system of the miniature double-focusing mass spectrograph

3.4 Ion optical system

Figure 3.4 shows the schematic drawing of the newly designed ion optical system where the ion trajectories for the mean radii in the magnetic sector of 25-75 mm at 5 mm intervals are shown. The deflection angle of the electrostatic sector is 60° and the gap between the electrodes is 10 mm. The inclination angle at the magnet entrance is 48.71°. The deflection angle of the magnetic sector is 74.73° and the gap between the pole pieces is 4 mm. The required size of the focal plane detector depends on the radius and the deflection angle of the magnet. If the maximal radius and the minimal radius are set at 66 mm and 25 mm, respectively, to achieve the detectable m/z range of 7, the required detector size is 70 mm. The physical parameters of the ion optical system and the elements of transfer matrix are shown in Table 3.1, where the mean radius in the magnetic sector is 50 mm.

In Table 3.1(a), the physical parameters of each ion optical component are shown. The

Table 3.1: Physical parameters of the ion optical system and the elements of the transfer matrix

(a) Physical parameters of ion optical components.

Drift space	DL = 0.0345
Toroidal ESA entrance	RO1 = 0.0000, GAP = 0.0050, NE1 = 2
Toroidal ESA	AE = 0.0500, WE = 60.00, C1 = 1.0000, C2 = -1.0000
Toroidal ESA exit	RO2 = 0.0000, GAP = 0.0050, NE2 = 2
Drift space	DL = 0.0450
Deflection is in reverse sense	
Sector magnet entrance	EP1 = 48.71, RO1 = 0.0000, GAP = 0.0050, NM1 = 2
Sector magnet	AM = 0.0500, WE = 74.73, N1 = 0.0000, N2 = 0.0000
Sector magnet exit	EP2 = -52.63, RO2 = 0.0000, GAP = 0.0050, NM2 = 2
Deflection is in reverse sense	
Drift space	DL = 0.0269

(b) Transfer matrix relating to the region from the ion source to the ESA exit

	x	α	γ	δ
x	0.5525	0.0625	0.0000	0.0250
α	-16.00	0.0000	0.0000	0.89371

(c) Transfer matrix of the whole system

	x	α	γ	δ	xx	$x\alpha$	$x\gamma$	$x\delta$
x	-0.3267	0.0000	-0.0183	0.0000	-38.42	5.313	-1.211	8.554
α	27.60	-3.061	0.0069	-4.271	1677	269.7	-6.080	-121.9
	$\alpha\alpha$	$\alpha\gamma$	$\alpha\delta$	$\gamma\gamma$	$\gamma\delta$	$\delta\delta$		
x	-0.3034	0.1160	-0.6745	0.0044	0.1619	-0.4602		
α	0.7392	1.552	-23.11	-0.0036	1.727	-3.706		
	yy	$y\beta$	$\beta\beta$					
x	17.09	-0.0487	-0.0001					
α	-1378	-205.3	0.7713					
	y	β						
y	-2.315	-0.06474						
β	-49.19	-1.724						

Table 3.2: The length of the last drift space, $(x|\alpha)$, $(x|x)$, $(x|\gamma)$ and $(x|\gamma)/(x|x)$ at the energy focusing point, i.e., where $(x|\delta) = 0.000$.

r_m	DL_3	$(x \alpha)$	$(x x)$	$(x \gamma)$	$(x \gamma)/(x x)$
25	12.2	0.000	-0.162	-0.0089	0.055
30	15.3	0.000	-0.195	-0.0108	0.055
35	18.3	0.000	-0.228	-0.0127	0.056
40	21.2	0.000	-0.261	-0.0145	0.056
45	24.1	0.000	-0.294	-0.0164	0.056
50	26.9	0.000	-0.327	-0.0183	0.056
55	29.8	0.000	-0.359	-0.0201	0.056
60	32.6	0.000	-0.392	-0.0220	0.056
65	35.5	0.000	-0.425	-0.0238	0.056
70	38.3	0.000	-0.458	-0.0257	0.056
75	41.1	0.000	-0.491	-0.0275	0.056

definitions of the ion optical parameters are presented in ref. [3.5]. From Table 3.1(b), it was found that the element of $(\alpha|\alpha)$ in the transfer matrix relating to the region from the ion source to the electrostatic sector is equal to zero. This indicates that the angle of an ion beam is independent of its initial angle, i.e., the ion beams are parallel in the drift space between the electrostatic sector and the magnetic sector. Accordingly, the first condition to realize a straight line for the double-focusing is fulfilled. The elements of $(x|\alpha)$ and $(x|\delta)$ for the whole ion optical system are equal to zero. This shows that the double-focusing is achieved in this ion optical system.

The elements of $(x|\alpha)$, $(x|x)$ and $(x|\gamma)$ at the energy focusing point for mean radii of the magnetic sector from 25 mm to 75 mm at 5 mm intervals are shown in Table 3.2. The length of the last drift space between exit of the magnetic sector and the energy focusing point is also shown in the second column of Table 3.2. From the column of $(x|\alpha)$, it can be confirmed that the double-focusing is achieved for all mean radii in the magnetic field. The elements of $(x|x)$ and $(x|\gamma)$ are respectively the image magnification in the horizontal direction and the mass dispersion coefficient. When the double focusing is satisfied, the mass resolution R is

expressed in the first-order approximation as:

$$R = \frac{(x|\gamma)}{(x|x)s_0} \quad (3.1)$$

Here, s_0 is the main slit width. Equation 3.1 indicates that the mass resolution of the ion optical system would be proportional to the value of $(x|\gamma)/(x|x)$. The values of $(x|\gamma)/(x|x)$ for each mean radius are equal in this ion optical system, as shown in the last column of Table 3.2. The main slit width s_0 is a constant value for all mean radii. Thus, the mass resolution is independent of the mean radii of the magnetic sector. Consequently, the mass spectra can be observed with a same mass resolution in overall detecting plane.

3.5 Numerical evaluation of the newly designed ion optical system

For the evaluation of the newly designed ion optical system, several simulations were carried out by TRIO 2.0. First, the ion trajectories were simulated in the first-order. The ion trajectories in x - and y -direction are shown in Figure 3.5. It can be clearly found that the ion trajectories with each initial energy deviation and those with each initial angular deviation focus at a point.

Then, the energy and angular focal planes were simulated in a small range of the mass deviation γ by TRIO 2.0. The simulated focal planes are shown in Figure 3.6. The mean radius in the magnetic sector of the mass deviation $\gamma = 0$ is 50 mm. The ion trajectories for the mass deviations from $\gamma = -0.06$ to 0.06 at 0.02 intervals were simulated in third-order. The focusing points were given as an intersection of trajectories, e.g., an energy focusing point is the intersection of two trajectories whose initial energy deviations are δ and $-\delta$. As shown in Figure 3.6(b), the energy and angular focusing points for each value of γ are coincide with each other, and these are along a straight line. It shows that this ion optical system is sufficiently available for a mass spectrograph employing a focal plane detector.

The mass resolution of a mass spectrograph is directly dependent on the main slit size. However, when the width of the beam profile would become small, the spatial resolution of the detector has influence on the mass resolution. The image of the beam profile and the

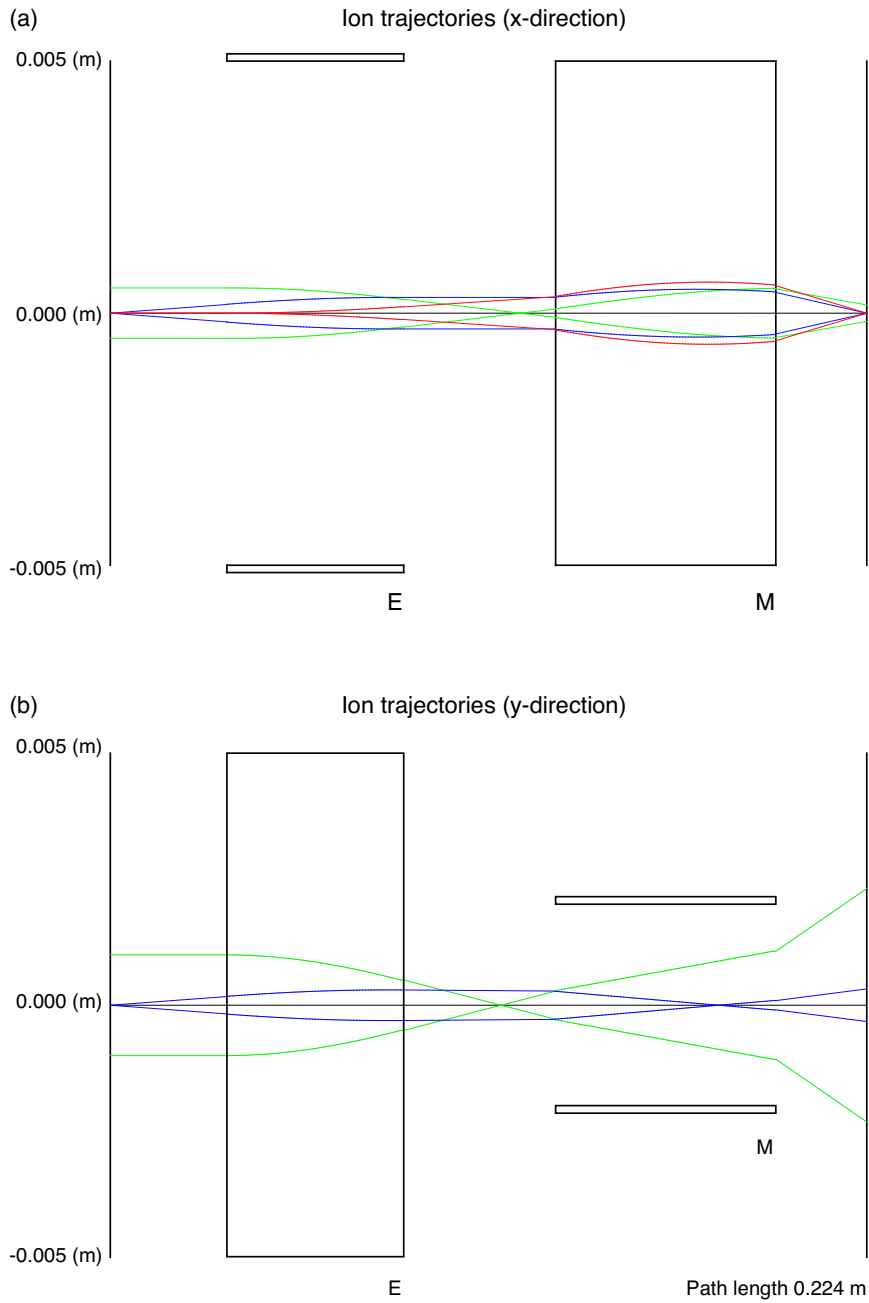


Figure 3.5: Ion trajectories of the ion optical system simulated in the first-order. That of in (a) x - and (b) y -direction are shown. The initial conditions are as follows: $x_0 = \pm 0.5$ mm, $\alpha_0 = \pm 0.005$, $y_0 = \pm 1$ mm, $\beta_0 = \pm 0.005$, and $\delta = \pm 0.005$

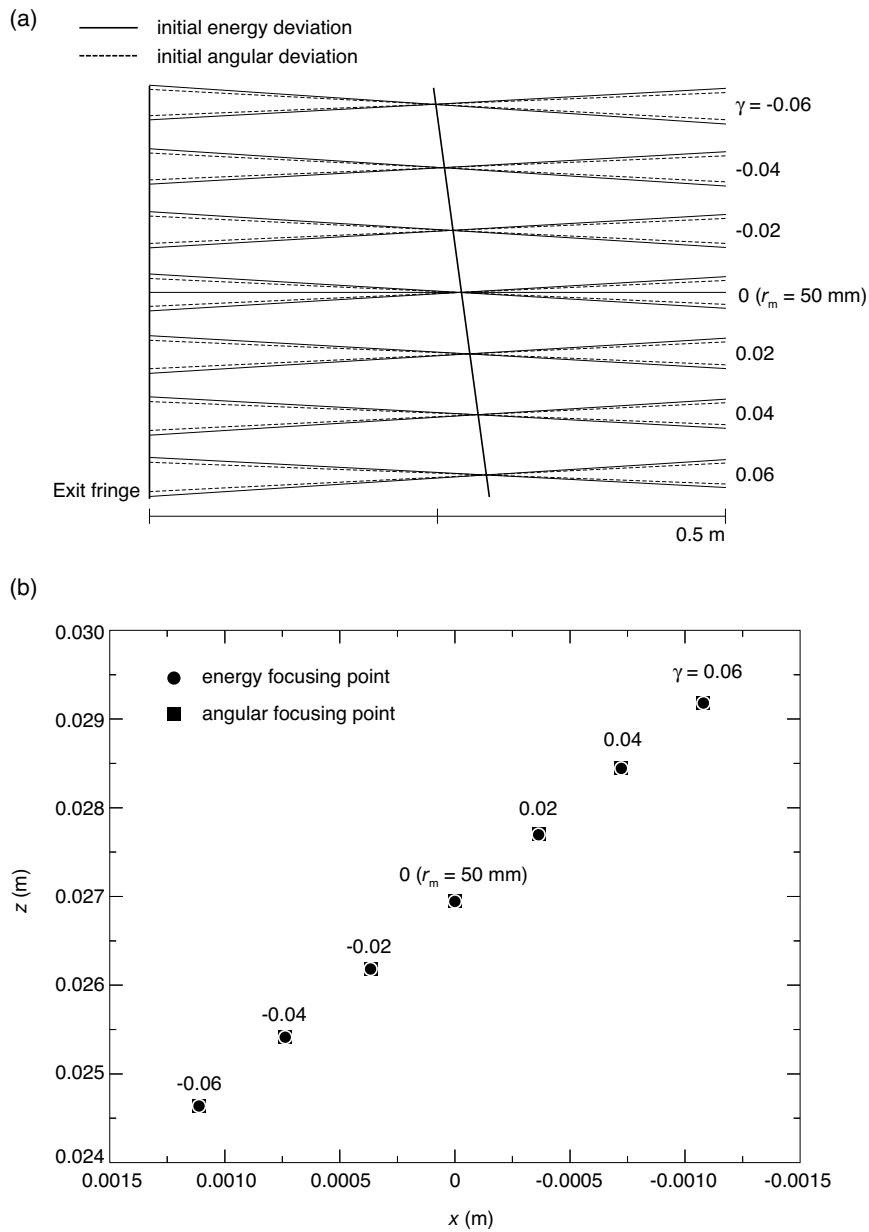


Figure 3.6: Energy and angular focal planes of the miniature double-focusing mass spectrograph simulated in the third-order. (a) Ion trajectories with the initial energy and angular deviations for each value of γ , where the mean radius of the magnetic sector is 50 mm. (b) The expanded plot of the energy and angular focusing points for each value of γ .

mass resolution are simulated for several slit sizes. The simulated images of the beam profile are shown in Figure 3.7. The ion beams that the mean radius in the magnetic sector is 50 mm were simulated. The spatial resolution of the focal plane detector practically employed in the instrument is $48 \mu\text{m}$. The details of the focal plane detector are described in chapter 4. Figures 3.7(a)-(d) shows the images with the pixel of $48 \mu\text{m}$. The slit conditions of each image are as follows: (a) the main slit width and height are 0.25 and 2.0 mm, respectively. (b) the main slit width and height are 0.15 and 2.0 mm, respectively. (c) the main slit width and height are 0.07 and 2.0 mm, respectively. (d) the main slit width and height are 0.07 and 1.0 mm, respectively. In these simulations, the α slit width and height are 0.5 and 3.0 mm, respectively. From Figures 3.7(a)-(c), it can be clearly found that the mass resolutions increase as the main slit width decreases.

In this ion optical system, the aberration coefficient of $(x|yy)$ is comparatively large ($(x|yy) = 17.09 \text{ m}^{-1}$) and the angular focusing in the y -direction is not satisfied. Accordingly, the main slit height may have influence on not only the image height but also the image width. Figure 3.7(d) shows the simulation when the main slit height is 1.0 mm. Figures 3.7(c) and (d) show that the aberration of $(x|yy)y_0^2$ has large influence on the image width. The image width of Figure 3.7(d) was about $150 \mu\text{m}$ (10% valley). As previously mentioned, when the image width is as small as the pixel size, the pixel size would affect the image width. Then, the image with the pixel of $20 \mu\text{m}$ is shown in Figure 3.7(e). In this condition, the mass resolution of 500 was achieved. From above simulations, the condition of the main slit size and the spatial resolution required to achieve the mass resolution of 500 is the follows: the main slit width and height are 0.07 mm and 1.0 mm, respectively, the spatial resolution of the focal plane detector is less than $20 \mu\text{m}$.

The beam envelope and the ion transmission were simulated. In this ion optical system, ion beams will pass through the small gap width of 4 mm between the magnetic pole faces. Consequently, the ion transmission in the magnetic sector should be estimated. The simulated beam envelopes are shown in Figure 3.8. The mean radius in the magnetic sector is 50 mm. The beam envelopes were simulated with several value of $y_0 \text{ max}$. In each simulation, ion trajectories of 1000 particles are calculated. The beam envelop in x -direction is shown in Figure 3.8(a). Figure 3.8(b), (c) and (d) show the beam envelopes in y -direction for $y_0 \text{ max}$

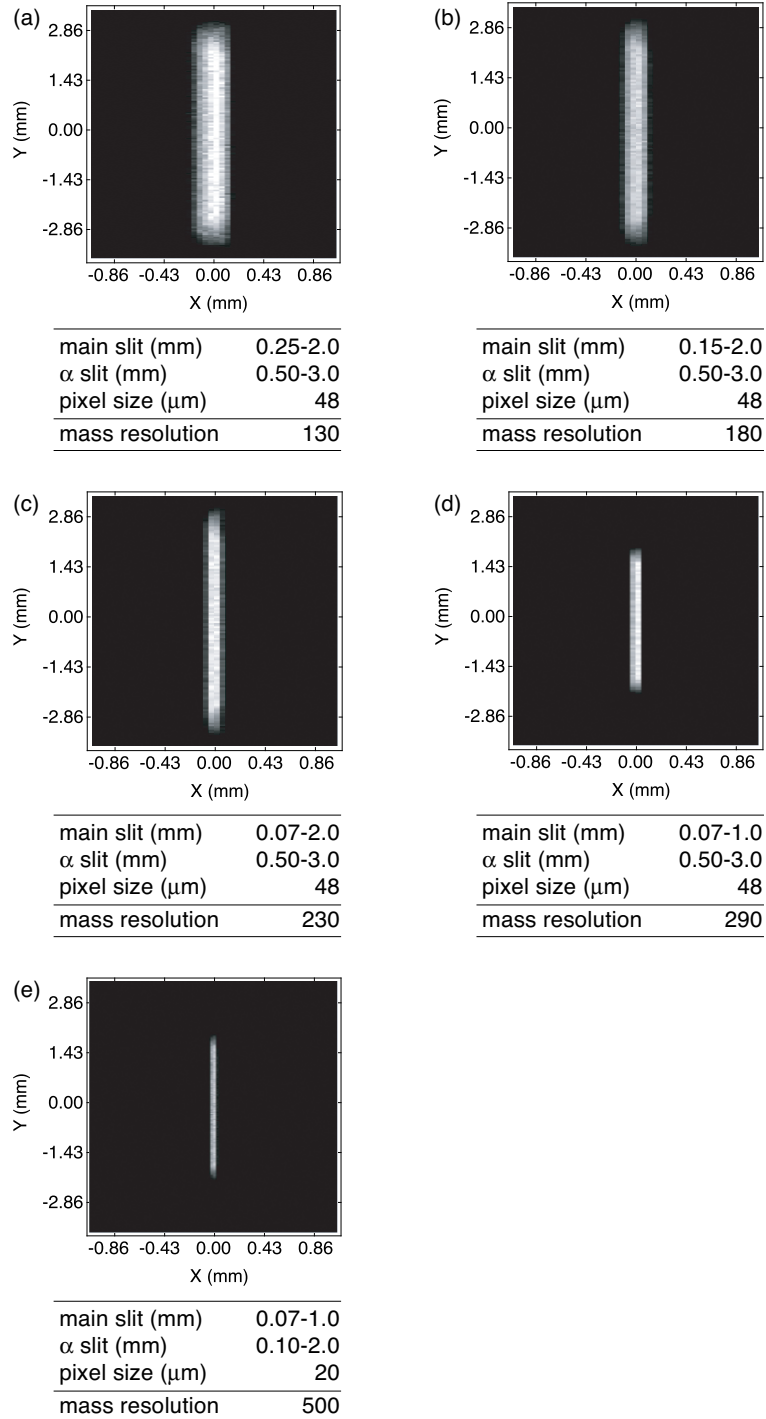


Figure 3.7: Images of the beam profile for several slit size. The main slit size, the pixel size and achieved mass resolution are as follows: (a) 0.25-2.0 mm, 48 μm and 130, (b) 0.15-2.0 mm, 48 μm and 200, (c) 0.07-2.0 mm, 48 μm and 250,(d) 0.07-1.0 mm, 48 μm and 290, and (e) 0.07-1.0 mm, 20 μm and 500, respectively.

= 1.0, 1.5, and 2.0 mm, respectively. In all cases, the other initial conditions are fixed as follows: $x_0 \text{ max} = 0.5 \text{ mm}$, $\alpha_0 \text{ max} = 0.005$, $\beta_0 \text{ max}$ is 0.01, and $\delta \text{ max} = 0.005$.

Since the spherical electrostatic sector has the focusing action in y -direction, the ion beam would be compressed in y -direction before entering the magnetic sector. It is effective to get a high transmission in the magnetic sector. This effect is obviously shown in Figures 3.8(b)-(d). At the condition of $y_0 \text{ max} = 1.5 \text{ mm}$, i.e., when the main slit height is 3 mm, the ion transmission of 100% was achieved by the simulation. Furthermore, almost all ions (about 90 %) could pass the magnetic sector when the main slit height is 4 mm.

3.6 Conclusion

The ion optical system of the miniature double-focusing mass spectrograph was newly designed. The ion optical system has the following features:

- The double focusing is satisfied along a straight line being at a distance from the exit fringe of the magnetic sector to employ a focal plane detector.
- The simultaneously detectable m/z range is 7.
- The mass resolution of 500 could be achieved when the main slit width and height are 0.07 and 1.0 mm, respectively, and the pixel size of the detector is 20 μm .
- A high ion transmission could be achieved. The ion transmission is 100% when the main slit height is 3 mm, and 90 % when the main slit height is 4 mm.

It was found that the pixel size of the detector would have influence of the mass resolution.

References

- [3.1] M. Nishiguchi, M. Toyoda, M. Ishihara, M. Ohtake, T. Sugihara, and I. Katakuse. Development of a miniature double focusing mass spectrograph using a focal plane detector. *J. Mass Spectrom. Soc. Jpn.*, 54:1–9, 2006.

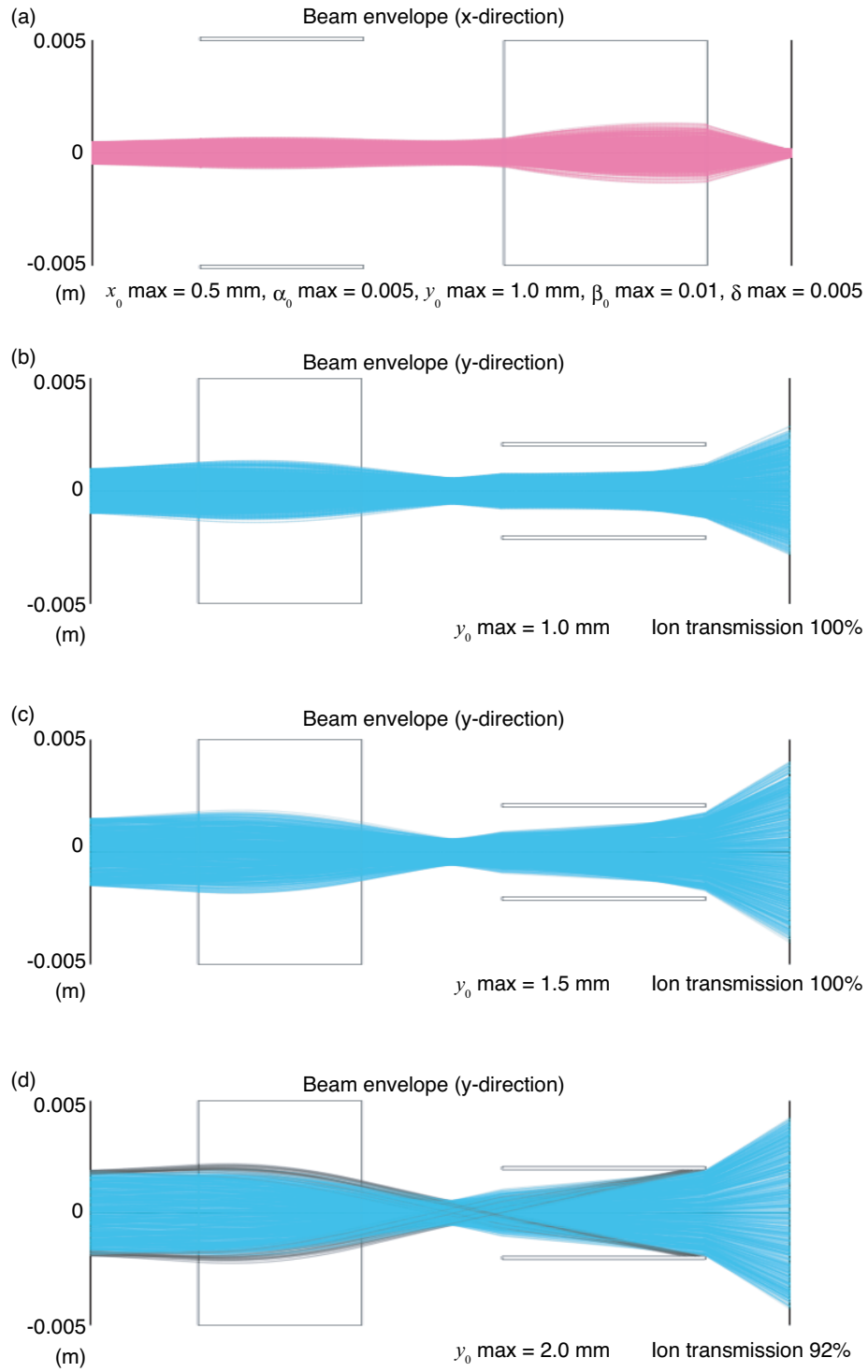


Figure 3.8: Beam envelopes and the ion transmissions in the ion optical system. (a) x-direction, (b) y-direction when $y_0 \text{ max} = 1.0 \text{ mm}$, (c) y-direction when $y_0 \text{ max} = 1.5 \text{ mm}$, and (d) y-direction when $y_0 \text{ max} = 2.0 \text{ mm}$

- [3.2] E. G. Johnson and A. O. Nier. Angular Aberrations in Sector Shaped Electromagnetic Lenses for Focusing Beams of Charged Particles. *Phys. Rev.*, 91:10–17, 1953.
- [3.3] J. Mattauch. A Double-Focusing Mass Spectrograph and the Masses of N^{15} and O^{18} . *Phys. Rev.*, 50:617–624, 1936.
- [3.4] H. Wollnik. *Optics of Charged Particles*. Academic Press. Inc., 1987.
- [3.5] T. Matuo, H. Matsuda, Y. Fujita, and H. Wollnik. Computer Program “TRIO” for Third Order Calculation of Ion Trajectory. *Mass Spectroscopy (Japan)*, 24:19–62, 1976.

Chapter 4

Instrumentation

4.1 Introduction

A miniature mass spectrograph employing the newly designed ion optical system was constructed [4.1]. The instrument is equipped with an EI ion source, a spherical electrostatic sector, a homogeneous magnetic sector and a focal plane detector using a CCD. The newly constructed instrument can detect ions over the wider mass range simultaneously than already developed mass spectrographs by combining the newly designed ion optical system and the large focal plane detector. In recent years, large imaging devices used in the focal plane detectors, e.g., photodiode arrays and CCDs, have become available at comparatively low cost. The instrument equips the CCD whose size is about 5 cm. A CCD driver system and a data acquisition system was developed. In this chapter, the detailed descriptions of each part of the instrument are given.

4.2 Whole instrument

Here, the technical drawing and a photograph of the newly constructed instrument are shown in Figures 4.1 and 4.2. The instrument is set in a circular vacuum chamber whose diameter is 40 cm. The vacuum chamber is evacuated with a turbomolecular pump (TMP 280G, SHIMADZU CORPORATION, Kyoto, Japan). The vacuum pressure is measured with an ionization gauge (GI-TL2, ULVAC, Inc., Kanagawa, Japan) attached at the side of the vacuum chamber. The base pressure is maintained at about 4×10^{-4} Pa. The mass analyzer is fixed on a base plate whose size is about 20 cm \times 20 cm. The focal plane detector is fixed to a movable stage. In this instrument, the position of the detecting plane can be adjusted by the practical ion optical conditions of the energy and angular focal planes. The details of each part are described in following sections.

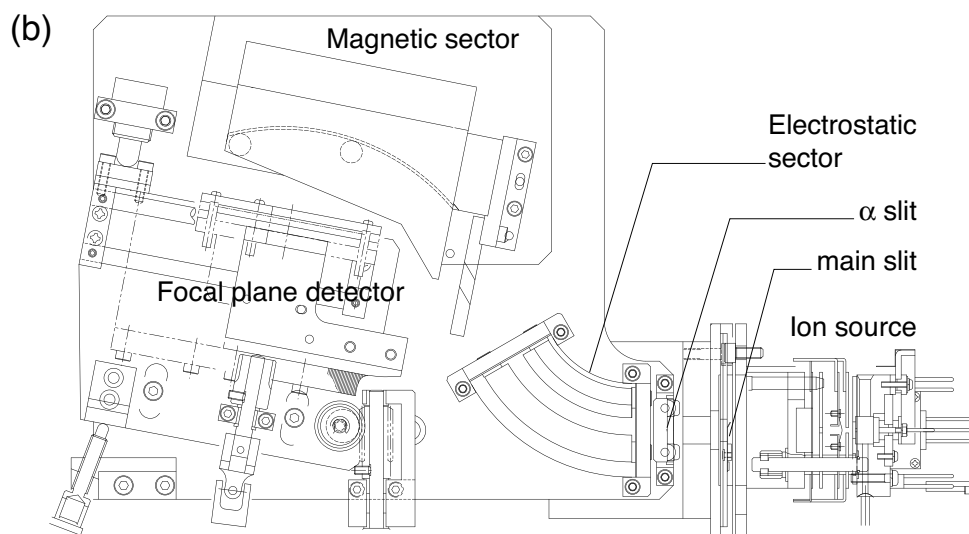
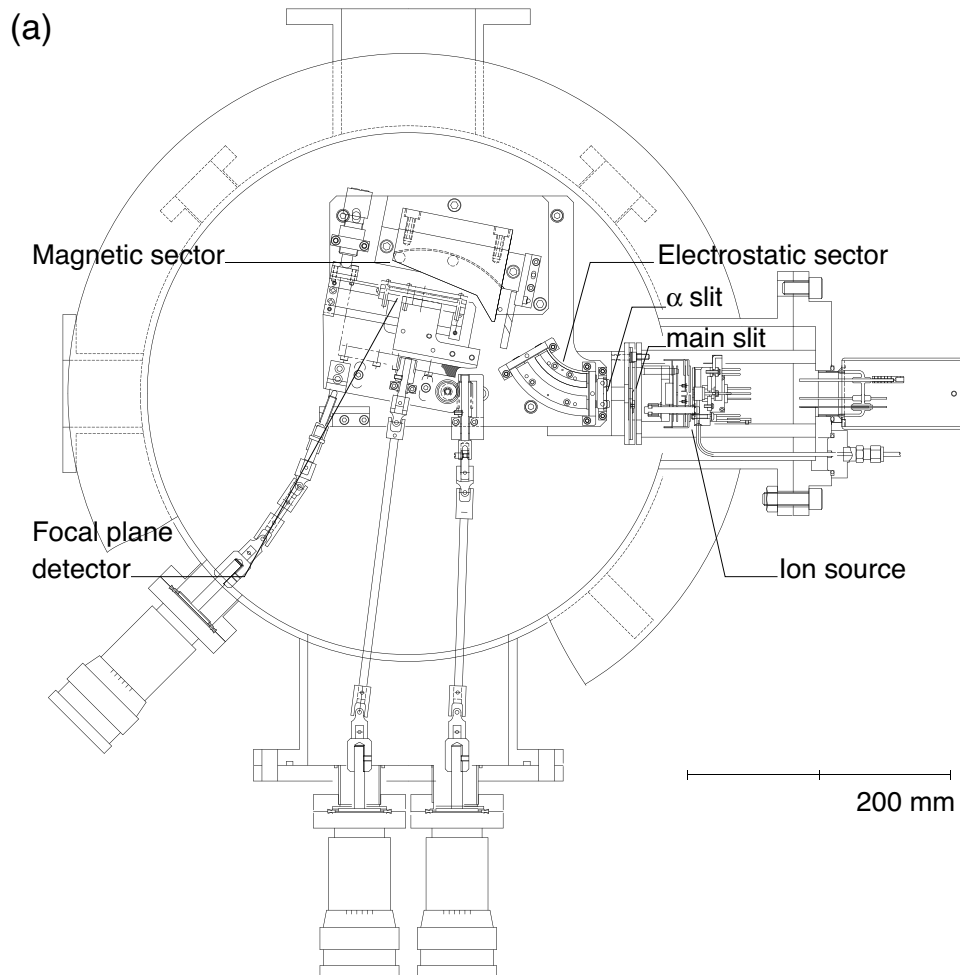


Figure 4.1: Technical drawing of the instrument. The drawings of (a) the instrument in the vacuum chamber and (b) the mass spectrograph are shown.

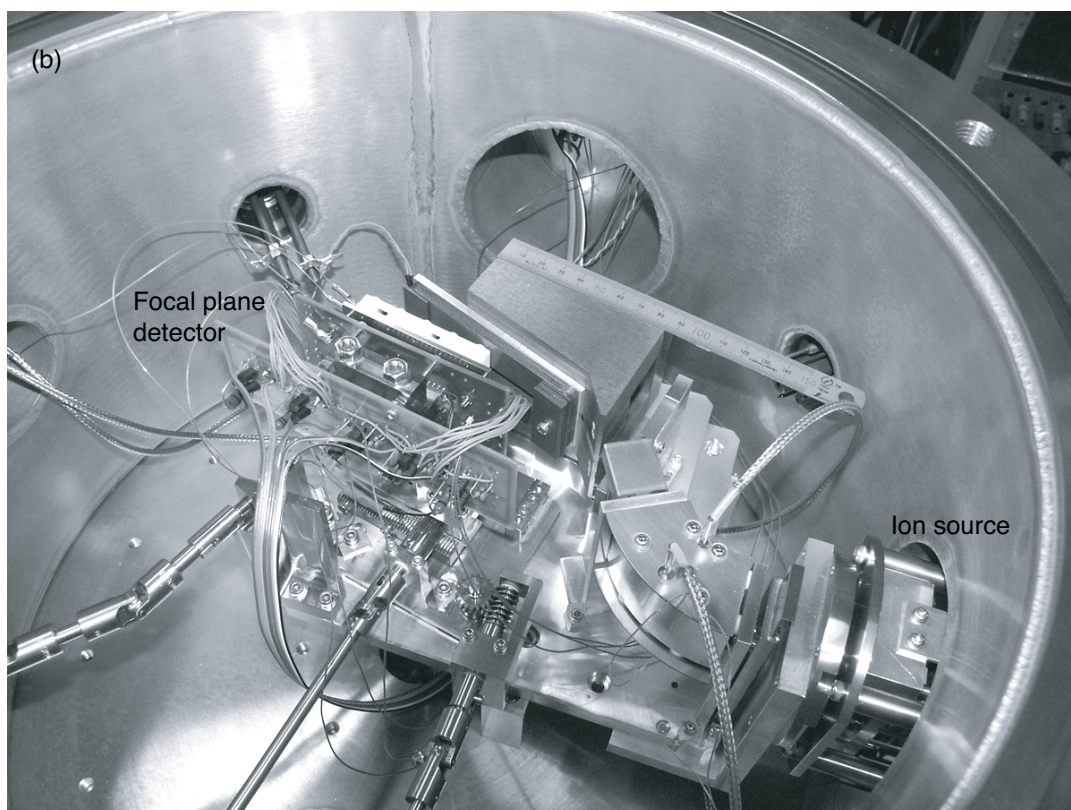
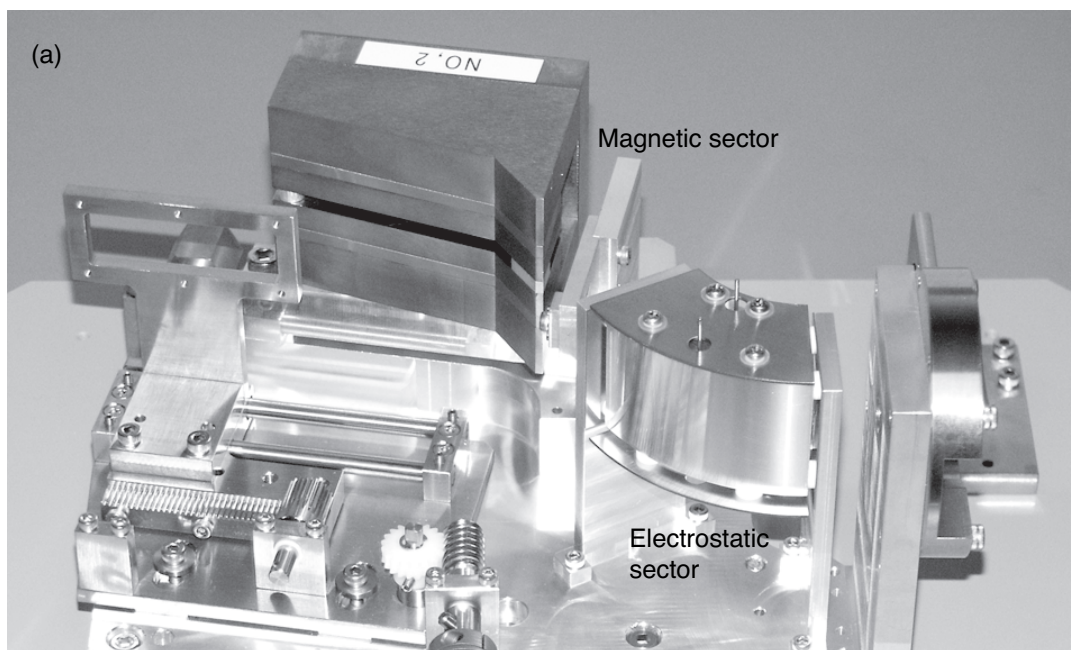


Figure 4.2: Photograph of the instrument. (a) The analyzer part and (b) the instrument in the vacuum chamber are shown.

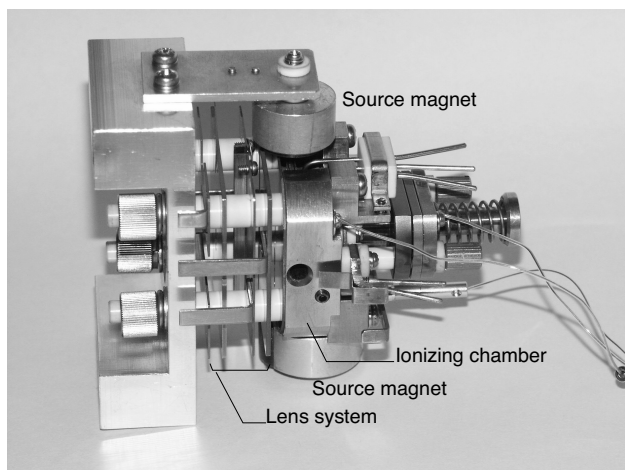


Figure 4.3: Photograph of the EI ion source. The same one used for JMS-HX110 is employed.

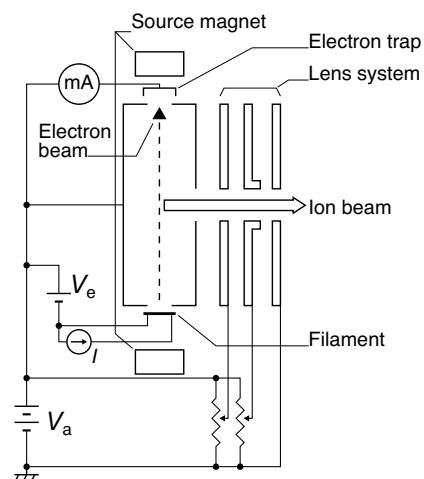


Figure 4.4: Schematic diagram of the EI ion source

4.3 Ion source

The EI ion source employed in this instrument is the same one as used for JMS-HX110 (JEOL, Tokyo, Japan). Although the development of a small and light ion source is also important in space exploration, a reliable ion source is needed for this instrument to evaluate the ion optical properties. Thus, the commercially available ion source was employed. A photograph and a schematic diagram of the ion source are shown in Figures 4.3 and 4.4, respectively. In Figure 4.4, the voltages of V_a and V_e correspond to the accelerating voltages of ions and that of electrons for the ionization, respectively. The accelerating voltage of V_a is supplied by a high voltage power supply (4105B, Fluke Corporation, USA). The accelerating voltage of ions can be applied up to 10 kV with this power supply. In this work, V_a is set in a range of 1–3 kV, and the accelerating voltage of electrons V_e is set at about 70 V.

4.4 Spherical electrostatic sector

A spherical electrostatic sector is employed in the instrument. A photograph and a technical drawing of the spherical electrostatic sector are shown in Figures 4.5 and 4.6, respectively. The mean radius, the gap width of the electrodes, the deflection angle and the height of the spherical electrostatic sector are 50 mm, 10 mm, 60° and 40 mm, respectively. The shielding

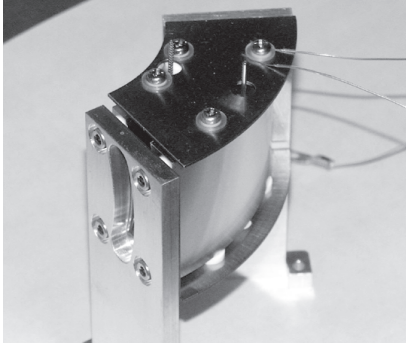


Figure 4.5: Photograph of the electrostatic sector

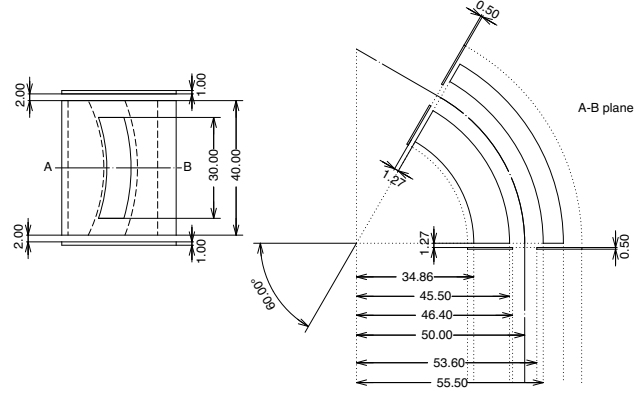


Figure 4.6: Technical drawing of the electrostatic sector

plates are equipped at the top and bottom of the electrode, and the height of the electrode is determined with a margin by considering the leakage of the field.

As well known, the theoretical voltage applied to the electrostatic sector depends on the accelerating voltage of the ions. The relation between the theoretical voltage applied to the electrostatic sector and the accelerating voltage for this spherical electrostatic sector is calculated as follows. When the voltages of $+V_E$ and $-V_E$ are applied to the outer and inner spherical electrodes whose radii are r_+ and r_- , respectively, the electric potential $\phi(r)$ and the electric field $E(r)$ are expressed as follows.

$$\phi(r) = -\frac{V_E}{r_+ - r_-} \left[\frac{2r_+r_-}{r} - (r_+ + r_-) \right] \quad (4.1)$$

$$E(r) = \frac{2r_+r_-V_E}{r_+ - r_-} \frac{1}{r^2} \quad (4.2)$$

The radius r_0 of the zero potential is derived from eq. 4.1 as

$$r_0 = \frac{2r_+r_-}{r_+ + r_-} \quad (4.3)$$

The equation of motion at the radius of r_0 is expressed as

$$\frac{mv^2}{r_0} = eE(r_0) \quad (4.4)$$

where m , e and v are the mass, charge and velocity of an ion, respectively. If the accelerating voltage of ions is V_a , the relation between the energy of the ion and the accelerating voltage

is given as the following well known equation.

$$\frac{1}{2}mv^2 = eV_a \quad (4.5)$$

Equations 4.4 and 4.5 yield

$$r_0E(r_0) = 2V_a \quad (4.6)$$

Then, substitution of eq. 4.3 into eq. 4.6 yields

$$V_E = 2 \frac{r_+ - r_-}{r_+ + r_-} V_a \quad (4.7)$$

In this spherical electrostatic sector, the radius of the zero potential and the gap width between the electrodes must be 50 mm and 10 mm, respectively. Accordingly, the outer radius r_+ and the inner radius r_- are set as 55.5 mm and 45.5 mm, respectively, from eq. 4.3. Thus, the relation between the theoretical voltage applied to the electrostatic sector and the accelerating voltage is derived as follows.

$$V_E = 0.1980V_a \quad (4.8)$$

The positive and negative voltages of the electrostatic sector were supplied by two voltage power supply modules (MP2P and MP2N, Spellman, UK). The ripple of the module is 10 mV. When the accelerating voltage of ions is 10 kV, the voltage applied to the electrostatic sector is about 2 kV, as shown in eq. 5.13.

4.5 Homogeneous magnetic sector

For a homogeneous magnetic sector, a permanent magnet is employed in the instrument to save power consumption. The magnetic circuit consists of pole pieces, magnets and a magnetic yoke. It was designed to achieve the required magnetic flux density and the sufficient uniformity. From the ion optical design, the gap width between the pole pieces was set at 4 mm. The magnetic flux density was determined as 0.576 T. When ions of m/z 4 are accelerated to 10 keV, the mean radius of the ion trajectory is 50 mm in this magnetic field. From these conditions, then, the thickness of the magnet and the material of the permanent

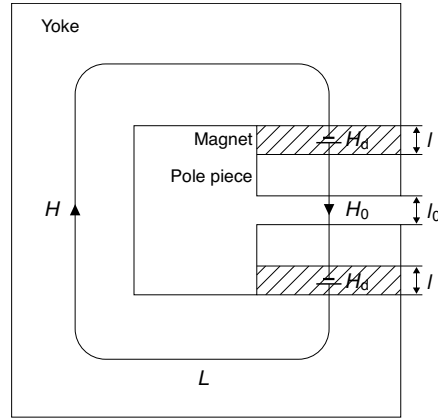


Figure 4.7: Schematic drawing of the magnetic circuit

magnet were considered. A schematic drawing of the considered magnetic circuit is shown in Figure 4.7. In the magnetic circuit, the following equation is satisfied by Ampère's law:

$$\oint \mathbf{H} \cdot d\mathbf{l} = 0 \quad (4.9)$$

The line integral of \mathbf{H} along the loop shown in Figure 4.7 is expressed as:

$$H_0 l_0 + HL + 2H_d l = 0 \quad (4.10)$$

where H_0 and l_0 are the magnetic field strength and the length along the integral line in the gap between the pole pieces, respectively, H and L are those in the pole pieces and the yoke, H_d and l are the magnetizing field strength and the thickness of the magnet. The magnetic flux density B_0 in the gap between the pole pieces and B in the pole pieces are generally comparable. On the other hand, the relative magnetic permeability of the iron is more than the order of 10^3 as well known, i.e., $\mu \gg \mu_0$ where μ and μ_0 are the magnetic permeability in the iron and the vacuum, respectively. In consequence, the magnetic field strength $H = B/\mu$ can be negligible compared with $H_0 = B_0/\mu_0$. Thus, equation 4.10 can be rewritten as:

$$rH_0 l_0 + 2H_d l = 0 \quad (4.11)$$

where r is the reluctance coefficient concerning the loss of the magnetizing force in the magnetic circuit. Generally, the reluctance coefficient r is in a range of 1.1–1.5. The magnetic flux density B_0 can be given with the remanent magnetic flux density B_d of the magnet and a

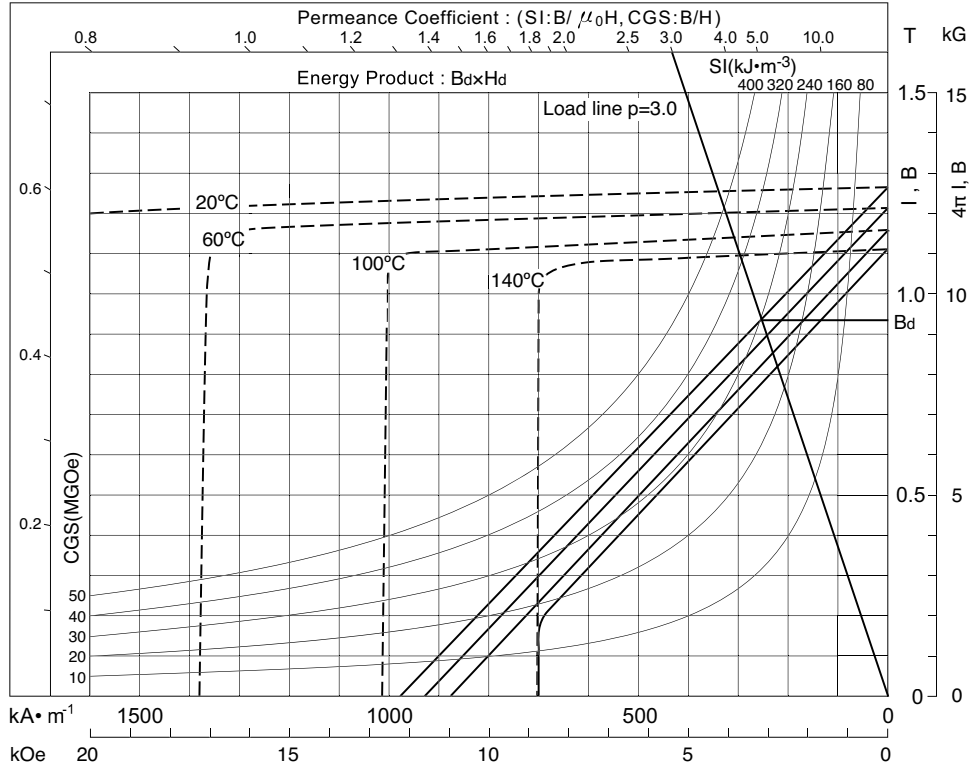


Figure 4.8: Demagnetization curves of NEOMAX 39SH and the load line of $p = 3.0$

coefficient σ concerning the leakage of the magnetic flux in the magnetic circuit as:

$$B_0 = \frac{B_d}{\sigma} \quad (4.12)$$

In ordinary cases, the coefficient σ is in a range of 1.5–4.0. From equations 4.11 and 4.12, the following equation can be derived:

$$\frac{B_d}{\mu_0 H_d} = -\frac{2\sigma l}{rl_0} \quad (4.13)$$

Here, $p = -B_d/(\mu_0 H_d)$ is called as the permeance coefficient that determines the practical remanent magnetic flux density B_d and the magnetizing field strength H_d from the demagnetization curve of the magnetic material. The intersection of the demagnetization curve with the load line corresponding the calculated permeance coefficient would give the practical operating point of B_d and H_d .

For the magnetic material, it is desired that the maximum energy product $B_d \times H_d$ should be as large as possible. Additionally, the material employed in a space exploration must has a

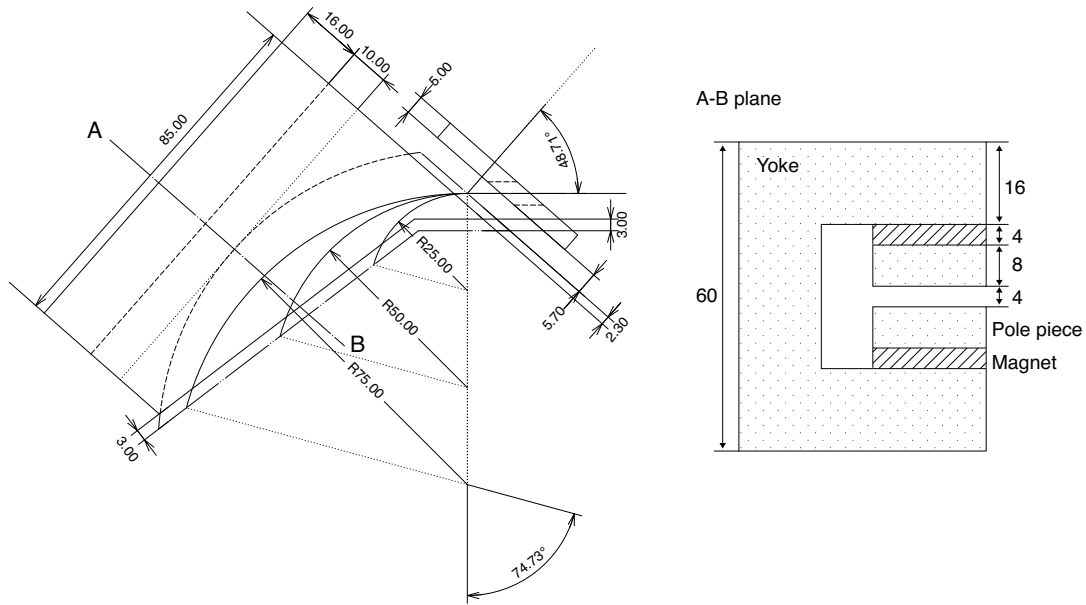


Figure 4.9: Technical drawing of the magnetic sector

high heat resistance. From these viewpoints, the magnetic material was selected. In this magnetic sector, a sintered Neodymium-Iron-Boron magnet (NEOMAX 39SH, NEOMAX Co., Ltd., Osaka, Japan) was employed as a permanent magnet. The maximum energy product is 319 kJ/m^3 (40 MGOe). The temperature characteristic of the magnetic material NEOMAX 39SH is as follows: the temperature coefficient of the magnetic flux density is -0.11% at 20°C , and the Curie temperature is about 400°C . For this magnetic material, the operating point in the demagnetization curve was determined.

Here, demagnetization curves of NEOMAX 39SH [4.2] are shown in Figure 4.8. First, the coefficients r and σ are empirically and roughly estimated as $r = 1.1$ and $\sigma = 1.5$. Then, the required remanent magnetic flux density B_d was calculated by eq. 4.12 as $0.576 \times 1.5 = 0.86 \text{ (T)}$. From the demagnetization curve at 20°C , the load line of the permeance coefficient $p = 3.0$ would sufficiently realize $B_d \approx 0.86$. The load line of $p = 3.0$ is also shown in Figure 4.8. Accordingly, the thickness of the magnet l was determined by eq. 4.13 as $l = l_0 = 4.0 \text{ (mm)}$. The thickness of the pole pieces were designed as 8 mm for the uniformity of magnetic field. Furthermore, the yoke was designed to prevent the magnetic saturation. The cross section of the magnet is about $1.35 \times 10^{-3} \text{ m}^2$. The saturation flux density of the iron is about

2 T as commonly known, and the flux density of 1.5 T in the iron is useful. In consequence, when the flux density in the gap between the pole pieces is about 0.6 T, the following relation between the cross section of the magnet S_0 and that of the magnetic yoke S can be given:

$$S > \frac{\sigma B_0}{B} S_0 = \frac{1.5 \times 0.6}{1.5} S_0 = 0.6 S_0 \quad (4.14)$$

The width of the yoke is 85 mm as shown in Figure 4.9. Here, the thickness of the yoke was set at 16 mm. The cross section of the yoke is $0.085 \times 0.016 = 1.36 \times 10^{-3}$ (m²). This cross section of the yoke would be sufficiently large as shown in eq. 4.14. Low-carbon steel SS400 (JIS G3101) is used for the pole piece and the yoke. Since the magnetic material is porous, the surface of the magnet is coated with TiN. This coating prevents adsorbed gases flowing out from the magnet.

A technical drawing of the magnetic sector and the magnetic circuit is shown in Figure 4.9. The inclination angle at the magnet entrance is 48.71°. The deflection angle of the magnetic sector is 74.73°. The mean radii of the magnetic sector are in a range from 25 to 75 mm.

4.6 Focal plane detector

The focal plane detector is an important part of the mass spectrograph. The detectable m/z range depends on the size of the focal plane detector. Furthermore, the mass resolution of the instrument would finally depend on the spatial resolution of the focal plane detector. The required size to observe the m/z range of 7 is 70 mm, and the required spatial resolution to achieve the mass resolution of 500 is 20 μ m as presented in the previous chapter. Needless to say, ideally, the size should be as large as possible, and the spatial resolution should be as small as possible. However, generally speaking, the spatial resolution would become large as the detector size increase. Therefore, it is quite difficult to select the best devices both in size and spatial resolution for the focal plane detector.

This instrument employs a focal plane detector consisting of an MCP, a phosphor layer on a fiber-optic plate (FOP) and a CCD. The schematic drawing of the focal plane detector is shown in Figure 4.10. In this focal plane detector, ions are detected as follows. Firstly, ion

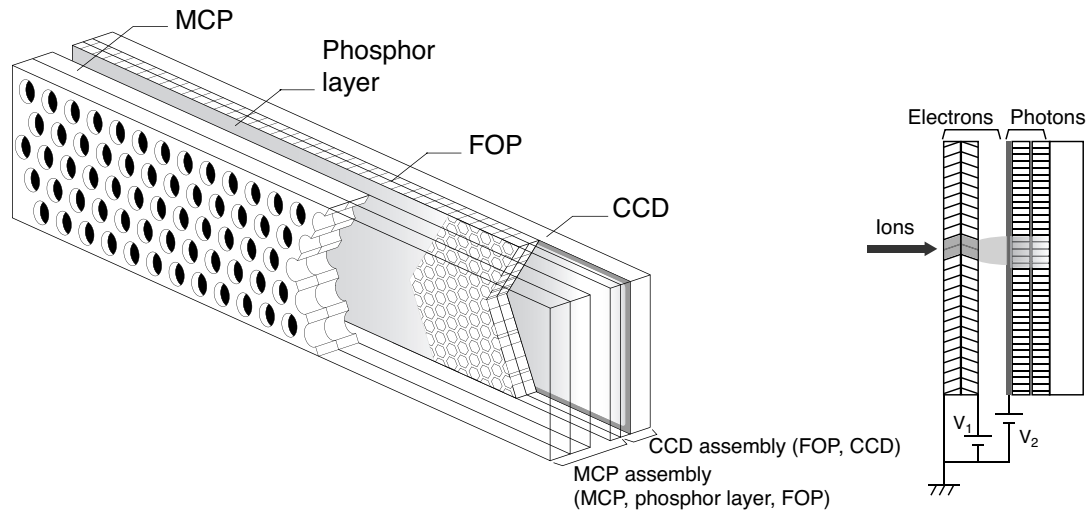


Figure 4.10: Schematic drawing of the focal plane detector

beams entering the channels of the MCP are converted and amplified to electron clouds by the MCP. The MCP also retains the spatial information of the profile of the ion beam. Then, these electrons are accelerated to the phosphor layer and converted into photons. Finally, these photons pass through the FOP and are detected by the CCD. In this focal plane detector, the size and spatial resolution are determined by those of the CCD. The specification of the CCD is described in subsection 4.6.2.

4.6.1 MCP assembly

An assembly (F4301-04, Hamamatsu Photonics, Shizuoka, Japan) comprising an MCP, a phosphor layer and a FOP is used for the detector [4.3]. The active area of the MCP is $55 \text{ mm} \times 8 \text{ mm}$ and the channel diameter is $12 \mu\text{m}$. The MCP is composed of two stages and the typical gain is over 10^6 if the voltage applied to the MCP is 2.0 kV. The front surface of the MCP is grounded. The type of phosphor is P46, and the typical wavelength and the decay time are 530 nm and 300 ns, respectively. A photograph of the MCP assembly is shown in Figure 4.11.

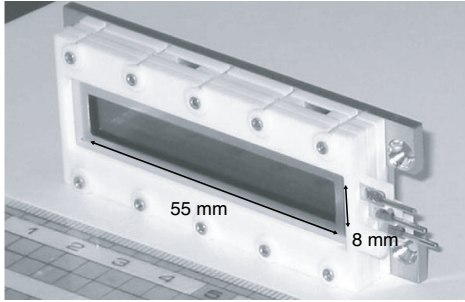


Figure 4.11: Photograph of the MCP assembly (F4301-04, Hamamatsu Photonics)

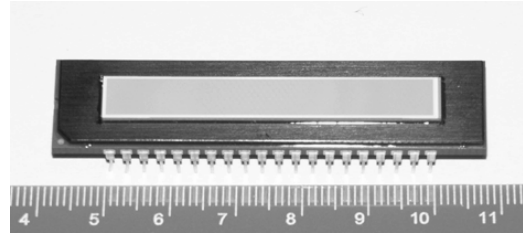


Figure 4.12: Photograph of the CCD (S7175F, Hamamatsu Photonics)

4.6.2 CCD area image sensor

In recent years, thanks to progress in semiconductor technology, large CCDs have become available at comparatively low cost. The CCD employed in this instrument is a front-illuminated type (S7175F, Hamamatsu Photonics, Shizuoka, Japan) [4.4]. The FOP window is attached in front of the CCD to couple with the MCP assembly. The structure of the CCD is a type of full frame transfer (FFT). The number of active pixels is 1024 (horizontal) \times 128 (vertical), each pixel is $48 \mu\text{m} \times 48 \mu\text{m}$, and the active area is $49.152 \text{ mm} \times 6.144 \text{ mm}$.

The FFT-CCD is comprised of one vertical shift register, one horizontal shift register and an output section. The vertical shift register operates as the photosensitive and storage section simultaneously. The horizontal shift register sends the signal charge transferred from the vertical shift register to the output section. Accordingly, the FFT-CCD is normally used in conjunction with an external shutter mechanism to ensure that no light enters the CCD while the signal charges are being transferred from the vertical shift register.

4.6.3 CCD driver system

A CCD driver system was newly developed. The operating principle of the FFT-CCD is as follows. During the signal integration, i.e., exposure period, the signal charge is collected in a potential well in the vertical shift register. Then the signal charge is transferred to the output section via the horizontal shift register during the closed period of an external shutter. In charge transfer operations, the CCD use a pair of gate electrode and it is called as two-phase CCD. In the two-phase CCD, the signal charge is transferred in the direction determined

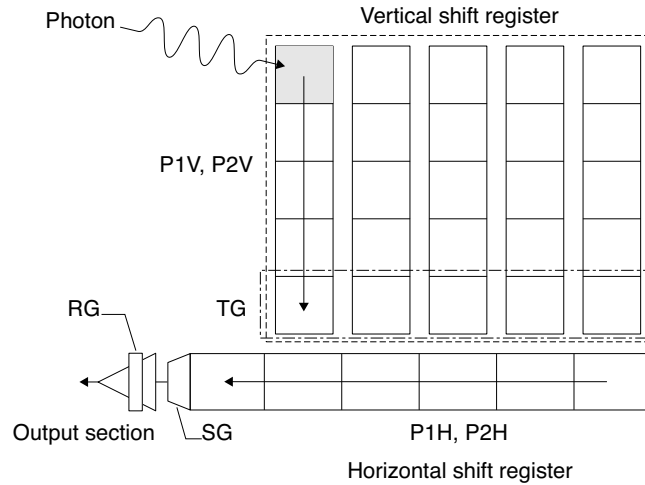


Figure 4.13: Schematic drawing of the CCD structure

by the potential difference created in the wafer process. A schematic drawing of the FFT-CCD is shown in Figure 4.13.

For this CCD, seven types of clocks are required. Two clocks of P1V and P2V are applied to the vertical shift register to transfer the signal charge because of the two-phase CCD. The clock of TG is applied to the transfer gate between the vertical shift register and the horizontal shift register and it is synchronized with P2V in ordinary uses. Two clocks of P1H and P2H are applied to the horizontal shift register. The clock of SG is applied to the summing gate between the horizontal shift register and the output section and it is synchronized with P2H in ordinary uses. The clock of RG is applied to the reset gate to clear the signal charge. The CCD can be operated by two modes: the line binning mode and the pixel binning mode. In the line binning mode, the signal charges in the vertical shift register are accumulated in the horizontal direction, and the output data is one-dimensional data of 1024 channels. In the pixel binning mode, the signal charges of all pixels are sent to the output section one after another, and the output data is two-dimensional data of 1024×128 channels. The timing chart for each clock in the line binning mode is shown in Figure 4.14. In addition, Figure 4.15 shows the timing chart of the clocks for the vertical (PV) and horizontal (PH) shift register in each mode of the line binning and the pixel binning.

Here, the schematic diagram of the CCD driver system is shown in Figure 4.16. The

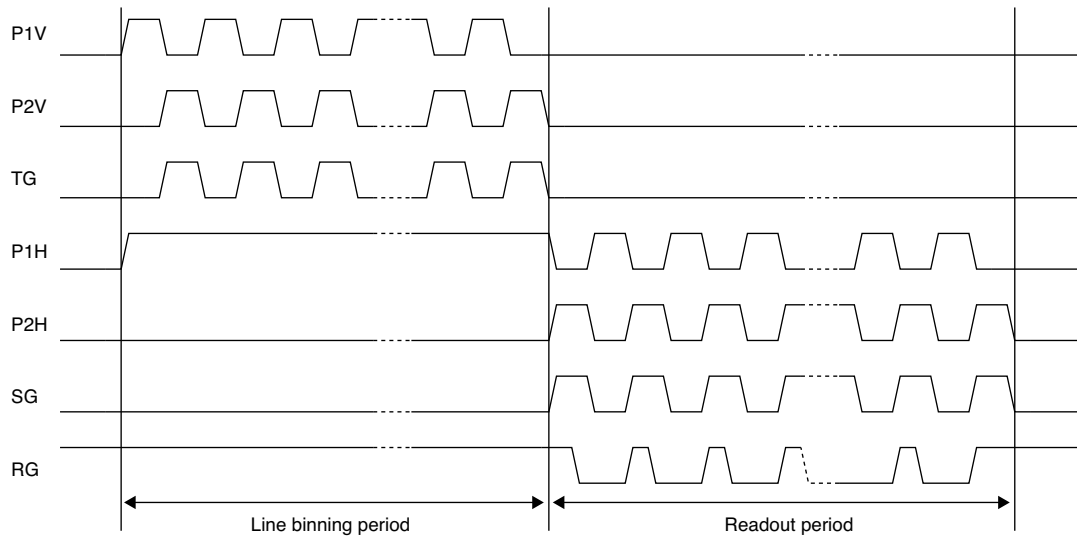
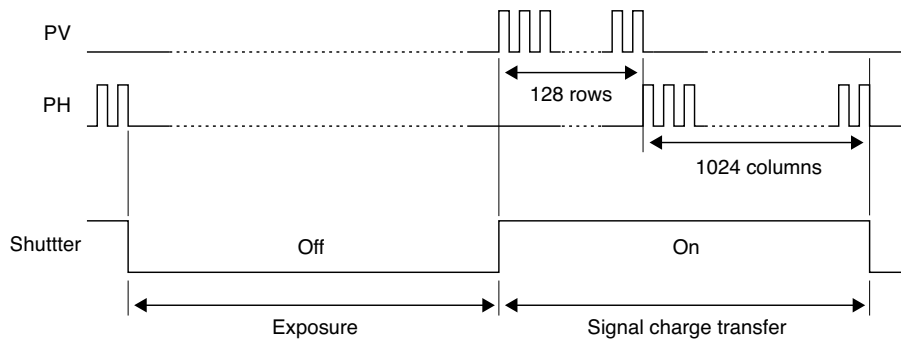


Figure 4.14: Timing chart of the clocks in the line binning mode of the CCD

(a) Line binning mode



(b) Area binning mode

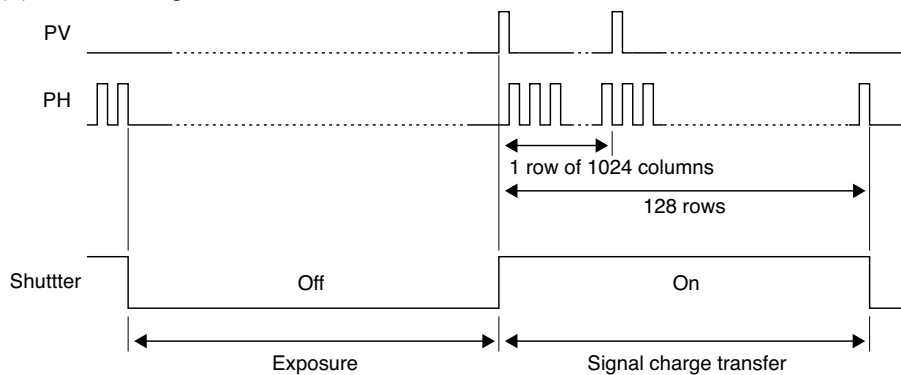


Figure 4.15: Timing chart of the clocks for the vertical (PV) and horizontal (PH) shift register in each mode of (a) the line binning and (b) the pixel binning.

required clocks for driving the CCD are generated by a digital I/O board (PCI-2472C, Interface, Hiroshima, Japan). A user interface to control the digital I/O board is developed by the graphical development environment (LabVIEW 6.0, National Instruments, Texas, USA). Although the digital I/O board generates nominal TTL signals of 0 - 5 V, the CCD requires -8 V at the low level and 6 V at the high level for signals. Thus, a voltage conversion circuit system was constructed. The circuit system consists of voltage conversion units and buffer units. TTL signals of 0 - 5 V are converted to signals of -8 - 6 V by the MOSFET switch of the voltage conversion unit. These signals are sent to the buffer units in the vacuum chamber. The buffer units are near the CCD in the vacuum chamber, and converted signals are branched after the buffer units as demanded for each signal. The same clocks are generated by branching the clock after the buffer units to simplify the circuit system. Since the clocks of P2V and TG are synchronous, these are branched from one clock. The clocks of P2H and SG are same as the clocks of P2V and TG.

In this driving system, the clock frequency of the signal charge transfer is 100 kHz. The frame rate in the line binning mode is about 100 frame per second (fps) without the exposure time. That in the pixel binning mode is about 1 fps.

4.7 Data acquisition system

A data acquisition system was newly developed. In the CCD, the signal charge transferred by the shift register is finally converted to the voltage corresponding to the charge. The method for charge-to-voltage conversion is the floating diffusion amplifier (FDA) method which is the most popular one [4.5]. A schematic diagram of the FDA method is shown in Figure 4.17. The method consists of nodes for detecting a charge and a pair of MOSFETs connected to each node. The charge in the detection node is converted into a voltage with the simple relationship $Q=CV$ by the readout MOSFET. This process is the nondestructive readout. The detecting node is reset by the reset MOSFET to the reference level in order to read the next signal. The output voltage from the CCD is first amplified by the preamplifier installed near the CCD as shown in Figure 4.17.

Then, the output signals are sent to a correlated double sampling (CDS) circuit [4.5]. The

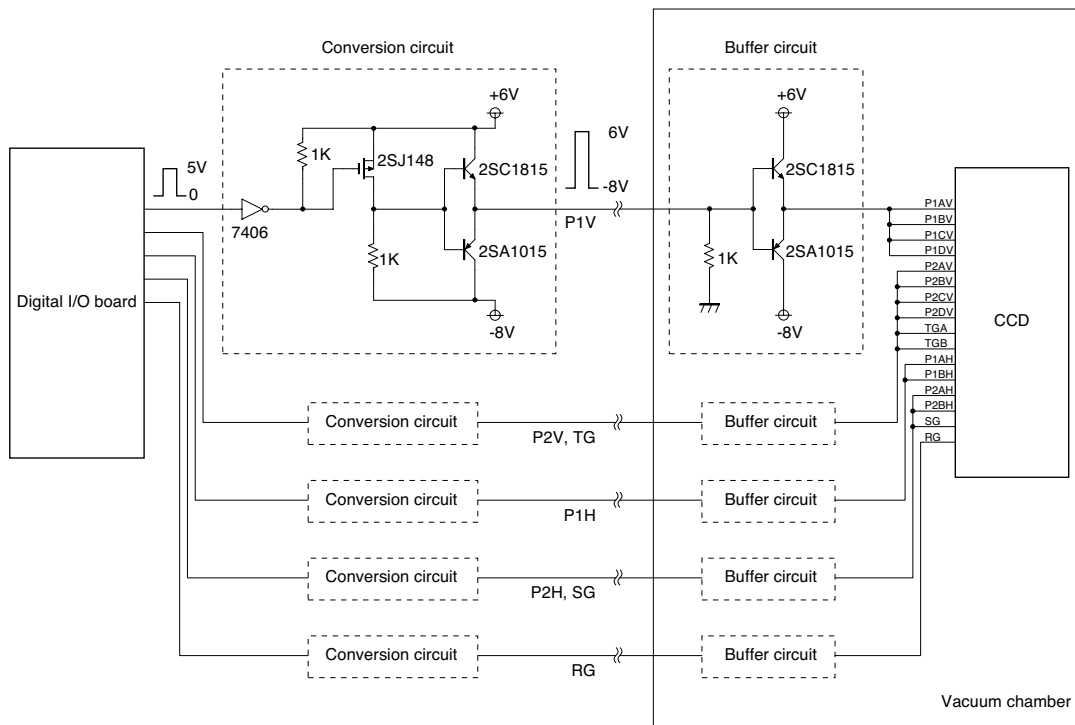


Figure 4.16: Schematic diagram of the CCD driver system

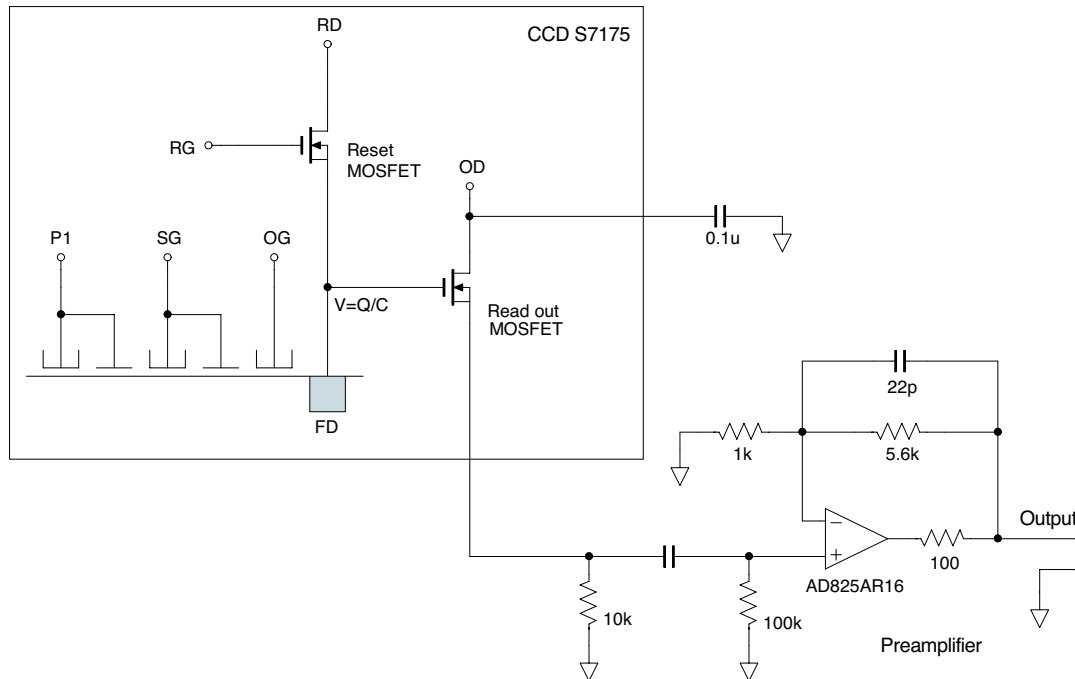


Figure 4.17: Schematic diagram of charge-to-voltage conversion method and the preamplifier

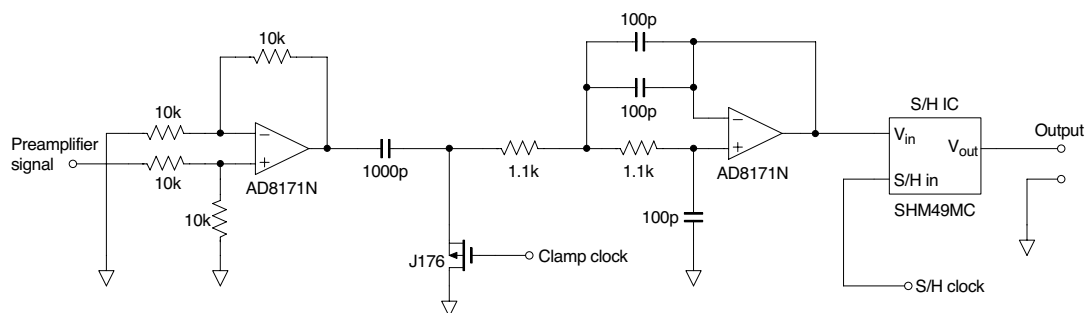


Figure 4.18: Schematic diagram of the CDS circuit

CDS circuit can remove the KTC noise associated with the capacitor of the shift register and the $1/f$ noise. The CDS circuit consists of a lowpass filter, a clamping circuit and a sample and hold circuit. A schematic diagram of the CDS circuit is shown in Figure 4.18. In the CDS circuit, the signal level immediately after reset is clamped at a certain voltage, then the signal level is sampled. The output signals of the CDS circuit are acquired as a digital data via a 12-bit A/D board (PCI-3163, Interface, Hiroshima, Japan). A user interface to control the A/D board is developed by LabVIEW (National Instruments, Texas, USA). The schematic diagram of the data acquisition system and the CCD driver system is shown in Figure 4.19. As previously explained, a shutter mechanism is required for the FFT-CCD. For the shutter mechanism, a pulsed voltage is applied to the deflecting electrode in the ion source to prevent the ion beam entering the detector while the signal charges are being transferred inside the CCD. The pulsed voltage is generated by a pulser using a MOSFET switch. All clocks for the data acquisition system and the shutter mechanism are also supplied by the digital I/O board (PCI-2472C) controlling the CCD driver system.

4.8 Conclusion

A miniature double-focusing mass spectrograph employing the newly designed ion optical system was constructed. The instrument consists of an EI ion source, a spherical electrostatic sector, a homogeneous magnetic sector and a focal plane detector. The focal plane detector is comprised of an MCP, a phosphor layer, a FOP, and a CCD. The CCD driver system and the data acquisition system was developed.

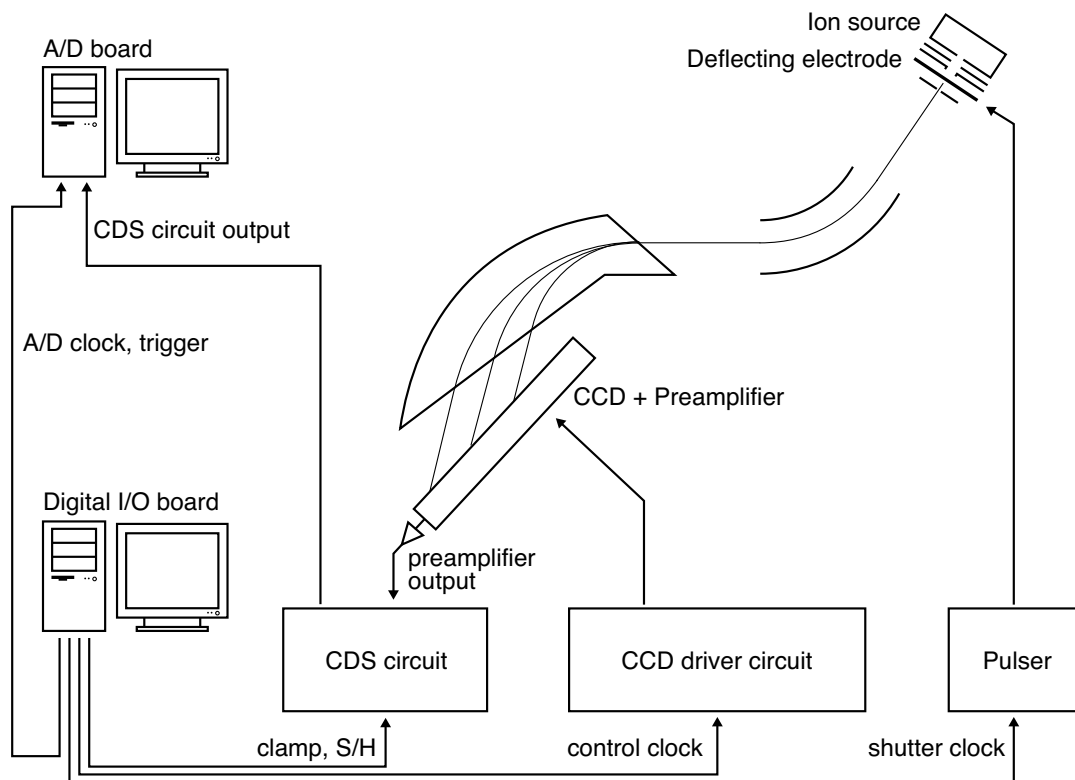


Figure 4.19: Schematic diagram of the data acquisition system and the CCD driver system

References

- [4.1] M. Nishiguchi, M. Toyoda, M. Ishihara, M. Ohtake, T. Sugihara, and I. Katakuse. Development of a miniature double focusing mass spectrograph using a focal plane detector. *J. Mass Spectrom. Soc. Jpn.*, 54:1–9, 2006.
- [4.2] NEOMAX Co., Ltd., Osaka, Japan. *Rare Earth-Iron-Boron-Permanent Magnets NEO-MAX*.
- [4.3] Hamamatsu Photonics, Shizuoka, Japan. *MCP & MCP ASSEMBLY*.
- [4.4] Hamamatsu Photonics, Shizuoka, Japan. *CCD area image sensor S7175*.
- [4.5] Hamamatsu Photonics, Shizuoka, Japan. *Characteristics and use of a FFT-CCD area image sensor*.

Chapter 5

Evaluation of the miniature double-focusing mass spectrograph

5.1 Introduction

The miniature double-focusing mass spectrograph was newly designed and constructed as presented in previous chapters. Then, the performance of the instrument was investigated. The shapes of the energy and angular focal planes are important ion optical properties in a mass spectrograph. The focal planes of the newly constructed mass spectrograph were evaluated experimentally. In the experiment, the peak shifts were observed when the initial energy or angle was fractionally changed. Additionally, the focal planes were also evaluated by the simulation to compare with the experimental result. Ion trajectories were simulated over several mean radii in the magnetic sector by combining the transfer matrix method and a ray tracing method. The energy and angular focusing points for each mean radius were calculated from simulated ion trajectories. Furthermore, an element of the transfer matrix of $(x|\delta\delta)$ was measured experimentally.

The quantitative performance is also essential for this instrument. The dynamic range of the simultaneous detection was evaluated. Moreover, the distribution of the gain in the employed focal plane detector was investigated.

In this chapter, the evaluation of the ion optical properties and the quantitative performance is described.

5.2 2D and 1D spectra

5.2.1 Observation of the phosphor layer image

First, images on the phosphor layer was observed for a performance check of the newly constructed instrument. When the CCD is not coupled with the MCP assembly, the image on the phosphor layer in the MCP assembly can be directly observed through a window attached

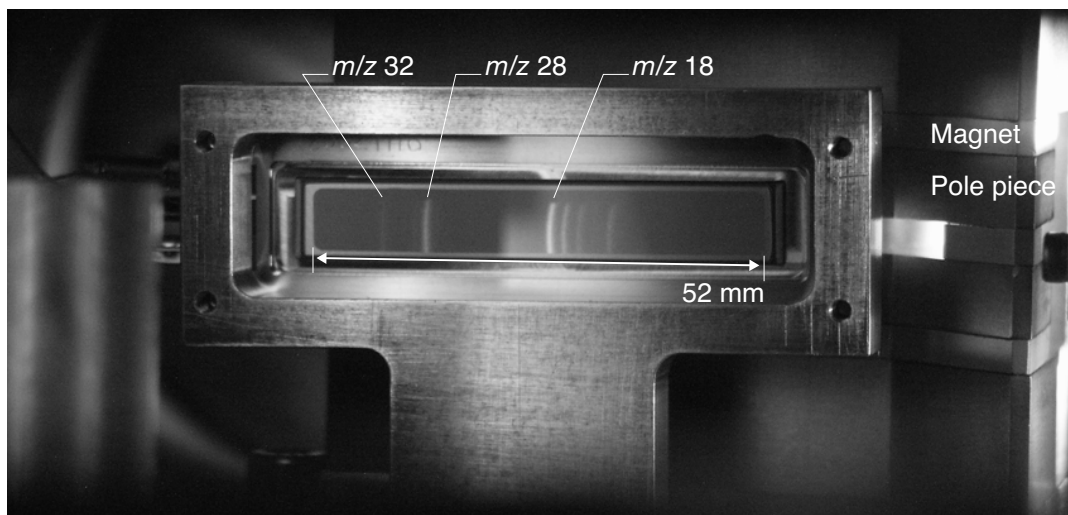


Figure 5.1: Photograph of the mass spectrum on the phosphor layer in the vacuum chamber

at the vacuum chamber. A photograph of a mass spectrum on the phosphor layer is shown in Figure 5.1. The spectrum of the residual gases in the vacuum chamber was observed. The photograph shows that the ion beams of each mass were dispersed in the magnetic sector and the luminous images of the ion beam profile were observed at the position where ion beams had arrived. From this experiment, it was confirmed that mass spectra could be observed in the newly constructed instrument. Then, the CCD was installed in the focal plane detector.

5.2.2 2D and 1D spectra

Without the magnetic shunt

The CCD was combined with the MCP assembly, and the image on the phosphor layer was observed by the CCD with the data acquisition system. A photograph of the assembled focal plane detector is shown in Figure 5.2. The preamplifier and the buffer circuit are set in the vacuum chamber near the CCD as explained in the previous chapter. The focal plane detector mounted near the exit of the magnetic sector. it can be moved to adjust the detecting plane by the practical focusing condition. First, the magnetic shunt at the exit fringe of the magnetic sector was not equipped.

Figure 5.3 shows 2D and 1D spectrum of residual gases without the magnetic shunt. The

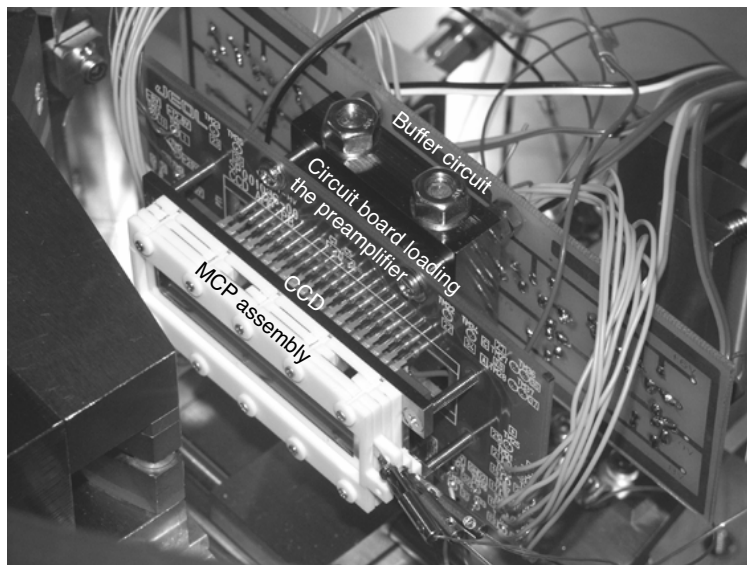


Figure 5.2: Photograph of the focal plane detector consisting of the MCP assembly and the CCD

experimental conditions were as follows: the accelerating voltage of the ions was 1500 V; the voltage applied to the electrostatic sector was ± 297.0 V; the electron energy and the electron current for the ionization were 70 eV and $200 \mu\text{A}$. The voltage applied to the MCP and the phosphor layer was 0.8 kV and 3.8 kV. The operation mode of the CCD was pixel binning, and the exposure time of the CCD was 1.0 s. The 1D spectrum was obtained by accumulating the lines from 10 to 120 of the 2D spectrum in the vertical direction. The abscissa axis of the 1D spectrum shows the CCD channel. The m/z value of a peak increases as the channel number increases.

Here, a broad image surrounded by a broken line in Figure 5.3(b) was observed. A small broad peak had coexisted with each main sharp peak as shown with solid circles in the 1D spectrum of Figure 5.3(c). The broad accompanying peak was always observed at any spectrum without the magnetic shunt. At any case, it was observed as the following characteristic way. The accompanying peak always appeared at smaller channel than that of the main peak. In addition, the distance between the accompanying and main peaks increased as the channel of the main peak increases. Thus, the accompanying peak would be artifact. The accompanying peak is nothing but a interference, and it must be eliminated for the quantitative

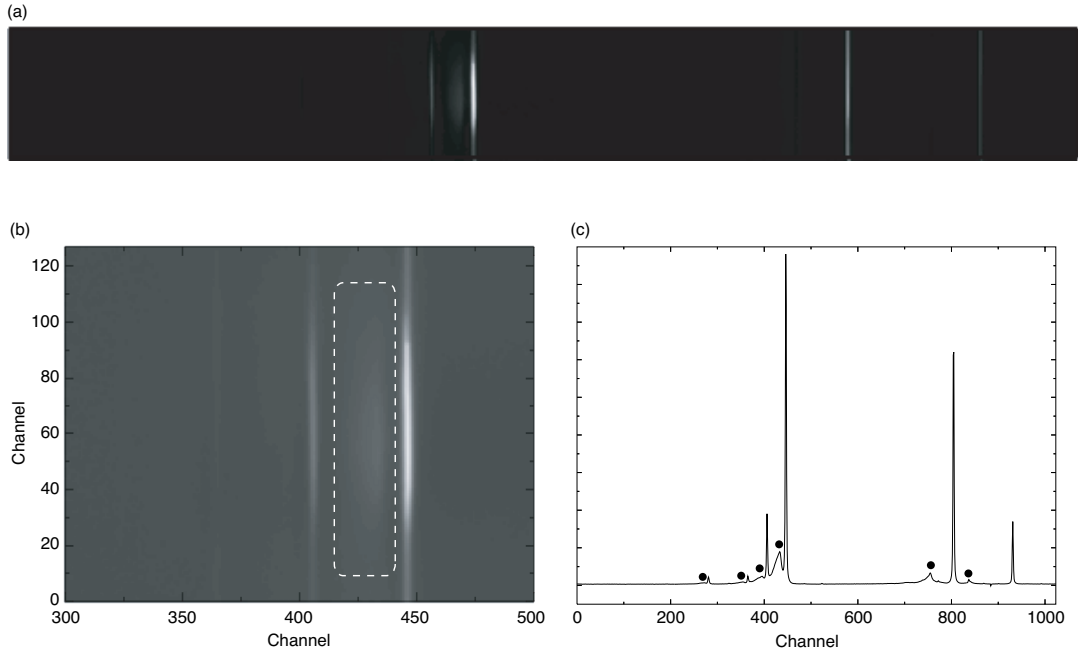


Figure 5.3: 2D and 1D spectrum of the residual gases without the magnetic shunt. (a) 2D spectrum , (b) expanded 2D spectrum in a range of 300-500 channels, and (c) 1D spectrum are shown.

analyses.

It was most likely that the broad accompanying peak would be caused by the sputtered electrons from the MCP. A schematic drawing of the motion of the sputtered electrons is shown in Figure 5.4. The accompanying peak can be consistently explained by the sputtered electrons from the MCP as follows. When the ion beam has arrived at the MCP surface, electrons would be sputtered to the front side of the MCP. Then, these electrons would be deflected into a circular orbit by the leaked magnetic field, and they would return to the MCP. The direction of the circular motion is same for all electrons because its direction is determined by the Lorentz force exerting on the electrons in the leaked magnetic field. In this system, the sputtered electrons would return at smaller channels than the position where the ion beam has arrived as shown in Figure 5.4. Accordingly, the accompanying peak would always appear at smaller channels than that of the main peak.

Furthermore, the distance between the MCP surface and the exit fringe of the magnetic

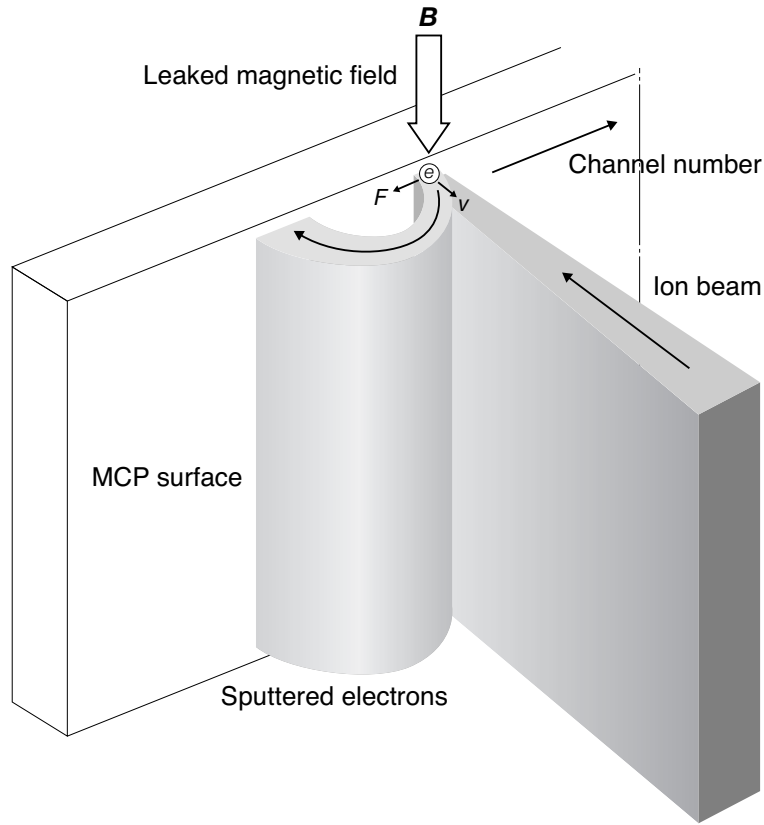


Figure 5.4: Schematic drawing of the motion of the sputtered electrons near the MCP surface

sector increases as the channel number increases in this instrument. In consequence, the strength of the leaked magnetic field would decrease at the MCP surface as the channel number increases. That is, the radius of the circular motion of the sputtered electrons would increase as the channel number increases. Therefore, the distance between the accompanying peak and main peak increases as the channel of the main peak increases. As discussed above, the cause of the accompanying peak is the sputtered electrons from the MCP surface and the leaked magnetic field.

From the above discussion, there are two effective methods in order to eliminate the accompanying peak. One is the method to apply the electric field so as to prevent that the electrons would be sputtered to the front side of the MCP. In this method, however, the electric field affects the ion trajectories and the focusing conditions if the electric field would properly limited. Accordingly, the mesh shield is generally required in front of the MCP

in this method. The other is the method to limit the leakage of the magnetic field so as to prevent that the sputtered electrons would not return to the MCP. The leakage of the magnetic field can be limited by installing the magnetic shunt at the exit fringe of the magnetic sector. In this instrument, the latter method was employed. The magnetic shunt was installed at the exit of the magnetic sector to eliminate the accompanying peak. The magnetic shunt was constructed by laminating iron plates.

With the magnetic shunt

Figure 5.5 shows 2D and 1D spectra of residual gases with the magnetic shunt. The experimental conditions were as follows: the accelerating voltage of the ions was 1550 V; the voltage applied to the electrostatic sector was ± 306.9 V; the electron energy and the electron current for the ionization were 70 eV and 200 μA . The voltage applied to the MCP and the phosphor layer was 0.8 kV and 3.8 kV. The operation mode of the CCD was pixel binning, and the exposure time of the CCD was 1.0 s. The 1D spectrum was obtained by accumulating the lines from 20 to 120 of the 2D spectrum in the vertical direction.

Figure 5.5 clearly shows that the accompanying peak was eliminated by installing the magnetic shunt. It was confirmed that the sputtered electrons to the front side of the MCP caused the accompanying peak. Then, the ion optical properties of the newly constructed instrument were evaluated in detail.

5.2.3 Mass resolution

For the evaluation of the mass resolution, the 2D and 1D spectra of the residual gases were observed. The detector position was practically adjusted so as to observe 2D and 1D spectra with a good focusing in the overall detecting range. The 2D and 1D spectra of the residual gases are shown in Figure 5.6. The experimental conditions were as follows: the width and the height of the main slit were 0.25 mm and 2.0 mm; the width and the height of the α slit were 0.5 mm and 3.0 mm; the accelerating voltage of the ions was 2200 V; the voltage applied to the electrostatic sector was ± 435.6 V; the electron energy and the electron current for the ionization were 70 eV and 250 μA . The voltage applied to the MCP

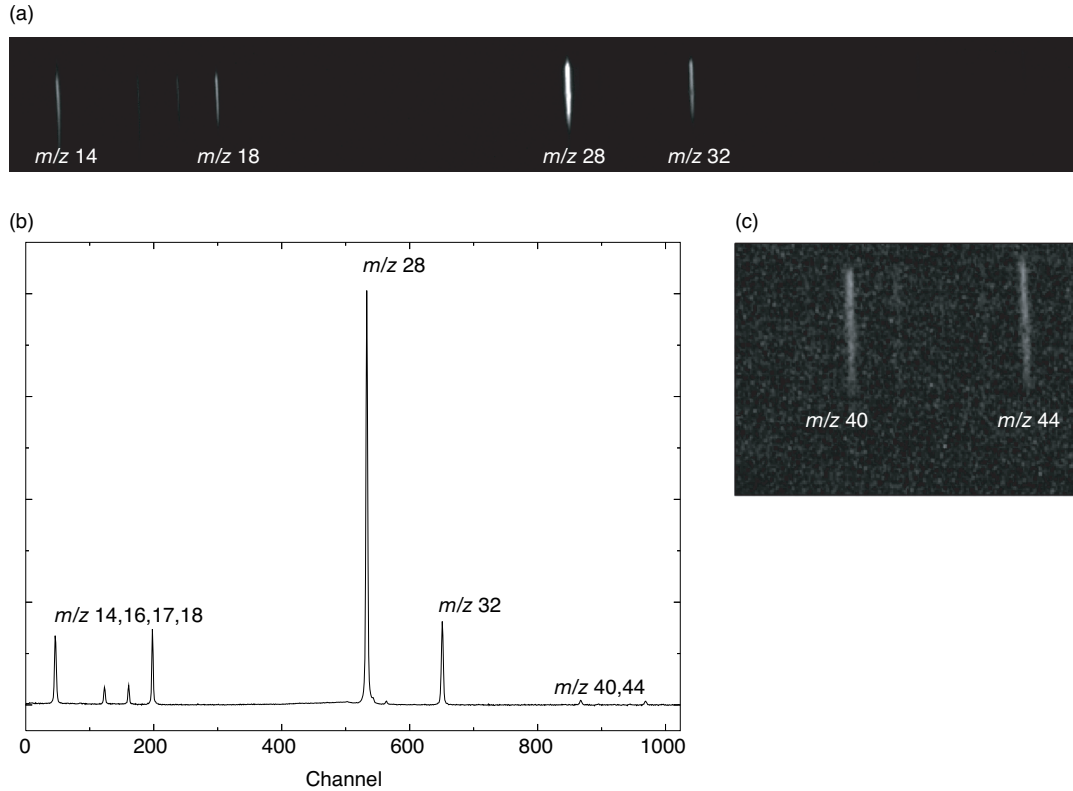


Figure 5.5: 2D and 1D spectra with the magnetic shunt. (a) 2D spectrum of the full range, (b) 1D spectrum obtained by accumulating the lines from 20 to 120 of the 2D spectrum in the vertical direction, and (c) expanded 2D spectrum in a range from 800 to 1000 channels with enhanced contrast.

and the phosphor layer was 0.7 kV and 3.7 kV. The operation mode of the CCD was the pixel binning, and the exposure time of the CCD was 1.0 s. The 1D spectrum was obtained by accumulating the lines from 10 to 120 of the 2D spectrum in the vertical direction. Then, the expanded 2D spectrum at m/z 18 of Figure 5.6(a) is shown in Figure 5.7(a). A mass resolution of 130 (10% valley) was achieved at this peak of m/z 18. The simulated image of the beam profile corresponding to the experimental data of Figure 5.7(a) is shown in Figure 5.7(b). The main and second slit sizes are set to coincide with the experimental conditions, and the initial energy deviation δ was in a range from -0.001 to 0.001. From the simulation of the beam profile, a mass resolution of 130 is obtained. The experimental result is, therefore, in good agreement with this simulation.

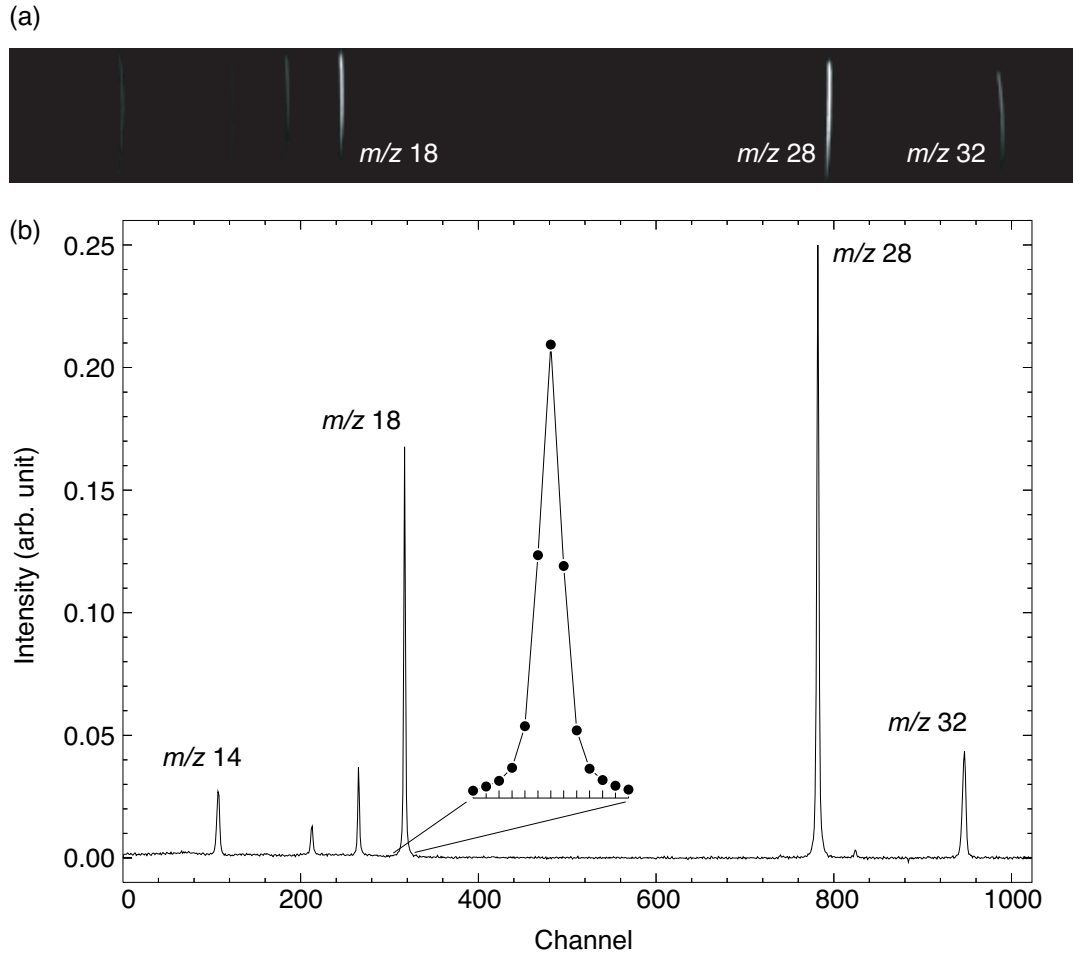


Figure 5.6: (a) 2D and (b) 1D spectra of residual gases. The 1D spectrum was obtained by accumulating the lines from 10 to 120 of the 2D spectrum in the vertical direction.

Then, mass resolutions experimentally achieved for three different main slit width are shown in Figure 5.8. When the main slit width are 0.15 mm and 0.07 mm, the mass resolutions of 150 and 200 were achieved, respectively. It was confirmed that the mass resolution increases as the main slit width decreases. The mass resolutions with the main slit width of 0.15 mm and 0.07 mm were, however, lower than the simulated values. This result can be explained by considering the increase of the image width of the beam profile, which mainly caused by the spread of the electron cloud in the MCP. The channel diameter of the MCP is $12 \mu\text{m}$, and it is composed of two stages. The final width of the electron cloud would spread by the following processes. First, the area of the channels generating the secondary electrons

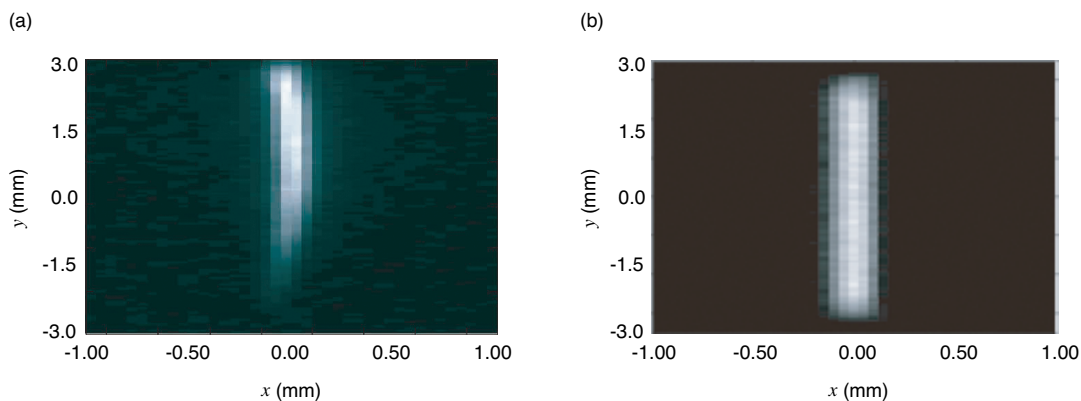


Figure 5.7: (a) 2D spectrum expanded around m/z 18 in Figure 5.6 and (b) simulated image of the beam cross section.

would be larger than the area of the ion beam profile because of the finite channel diameter of $12\ \mu\text{m}$. Even if the width of the ion beam profile is smaller than the channel diameter of the MCP, the ion beam would activate an area of channels corresponding a width of two or three channels as shown in Figure 5.9. Consequently, the initial width of the electron cloud would be about $20\text{--}30\ \mu$ larger than that of the ion beam profile. Moreover, the electron cloud would also spread at the bonded surface of the each stage of the MCP by the same reason. At this joint, the electron cloud would spread by $20\text{--}40\ \mu\text{m}$. Finally, the width of the electron cloud released from the MCP would spread about $80\ \mu\text{m}$ as large as that of the ion beam profile. This spread of the image width would have seriously influence on the mass resolutions with the main slit width of $0.15\ \text{mm}$ and $0.07\ \text{mm}$.

5.2.4 Evaluation of the detectable m/z range

As previously described, the simultaneous detection of a wide mass range is a significant feature of the mass spectrograph. The detectable m/z range was evaluated experimentally. In this ion optical system, the detectable m/z range depends on the detector size and the detector position. A schematic drawing of the geometrical configuration of the detecting plane and the observable mean radius of the magnetic sector is shown in Figure 5.10. From the geometrical consideration, the relation between the detectable mean radii of the magnetic sector and the

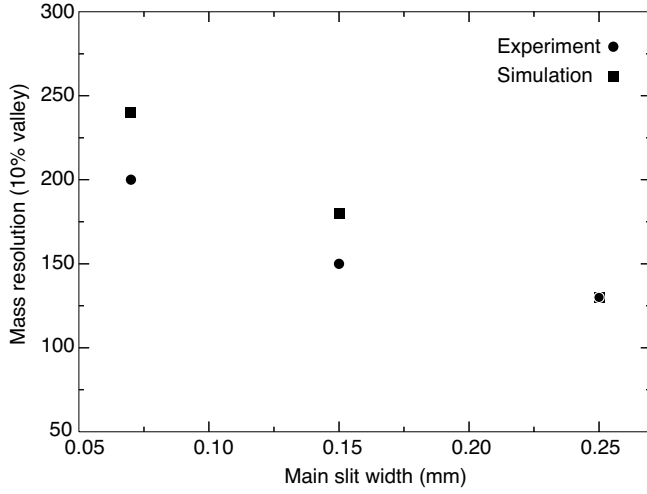


Figure 5.8: Mass resolution against the main slit width.

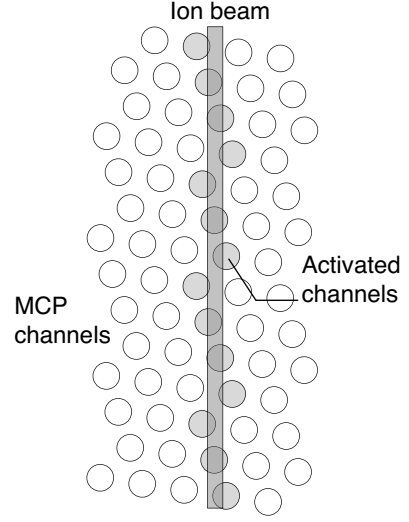


Figure 5.9: Increase of the image width in the MCP.

detector size D is given as follows:

$$r_{\max} - r_{\min} = \frac{\sin 25.50}{2 \cos^2 52.63} D = 0.5843D \quad (5.1)$$

where r_{\max} and r_{\min} are the maximal and minimal mean radius. As already mentioned, the detectable m/z range is defined as $(r_{\max}/r_{\min})^2$. From eq. 5.1, the detectable mass range is expressed as

$$\left(\frac{r_{\max}}{r_{\min}}\right)^2 = \left(1 + 0.5843 \frac{D}{r_{\min}}\right)^2 \quad (5.2)$$

From eq. 5.2, it can be found that the detectable mass range decreases as the minimal detected mean radius increases. In this system, the active area of the focal plane detector is about 50 mm. Accordingly, the detectable m/z range varies from 2.6 to 4.7 according to the detecting position.

In the 1D spectrum of Figure 5.6, the detectable m/z range was calculated. First, the channel numbers of the abscissa axis were calibrated to m/z . Since m/z is proportional to the square of the mean radius of the ion trajectory in the magnetic sector, the relation between m/z and the channel numbers of the abscissa axis can be expressed as $m/z = ax^2 + bx + c$. Here, a , b and c denote the calibration coefficients, and x denotes the channel numbers. These coefficients were calculated by applying the least-squares fitting to the channels numbers cor-

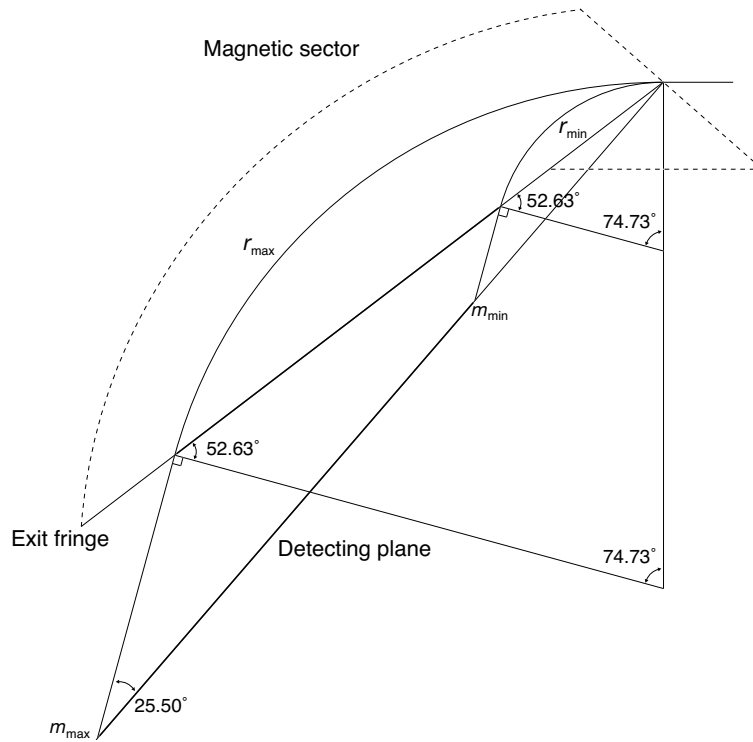


Figure 5.10: Schematic drawing of the geometrical relation between the detector and the detectable maximal and minimal radius of the magnetic sector

responding to the peak centroids of m/z 14, 18, 28 and 32. The 0 and 1024 channels correspond to m/z 12.4 and 34.1, respectively. In consequence, the detectable range of $34.1/12.4 = 2.8$ was obtained.

On the other hand, the mean radius of m/z 34.1 in the magnet is calculated as 68.5 mm when the accelerating voltage and the magnetic flux density are 2200 V and 0.576 T, respectively. When the maximal mean radius in the magnetic field is 68.5 mm, the minimal mean radius is calculated as 41.0 mm from eq. 5.1 by assuming a detector size of 50 mm. The detectable m/z range is then calculated as $(68.5/41.0)^2 = 2.8$. This value is well consistent with the experimental result.

5.3 Evaluation of the energy and angular focal planes

The shapes of the energy and angular focal planes are important properties in a mass spectrograph with a focal plane detector: these focal planes must be along the same straight line to observe highly resolved mass spectra in the overall detecting plane. In the 1930s, Mat-tauch and Herzog theoretically investigated conditions for double-focusing for all masses in a first-order approximation without taking into account the fringing fields [5.1]. Matsuda and Wollnik investigated the double-focusing properties of CQH-type mass spectrographs over a wide mass range using the transfer matrix method [5.2]. In their calculations, the influence of the fringing fields was taken into account up to the second order. They demonstrated two ion optical systems of the CQH-type mass spectrographs that would allow double-focusing in a mass range from m_0 to $3m_0$ and have small second-order aberration coefficients. In their ion optical systems, however, the energy and angular focal planes would, in principle, curve. Ishihara and Kammei proposed a lens system consisting of a quadrupole doublet and an octapole lens to enable the use of a focal plane detector in a conventional sector-type mass spectrometer [5.3]. They simulated the ion trajectories of a conventional double-focusing mass spectrometer using a lens system based on the transfer matrix method and showed that the curvature of the focal plane could be corrected by the octapole lens. In these investigations, the focal planes were only evaluated theoretically or by simulations.

In this section, the experimental evaluation of the focal planes for a wide mass range is presented. In order to evaluate the focal planes, the peak positions need to be measured with high accuracy. The dependence of the peak position on the magnet temperature, therefore, was measured for correction of the data.

5.3.1 Method for the evaluation of the energy and angular focal planes

First, the evaluation method of the energy focal plane would be explained in detail. If the energy focusing is satisfied on the detecting plane, the peak position does not shift by the value of the initial energy deviation δ in the first-order approximation. In other words, if the energy focusing is not satisfied, the peak position shifts by the value of δ . Figure 5.11 is a schematic drawing of the direction of the peak shifts under three different focusing

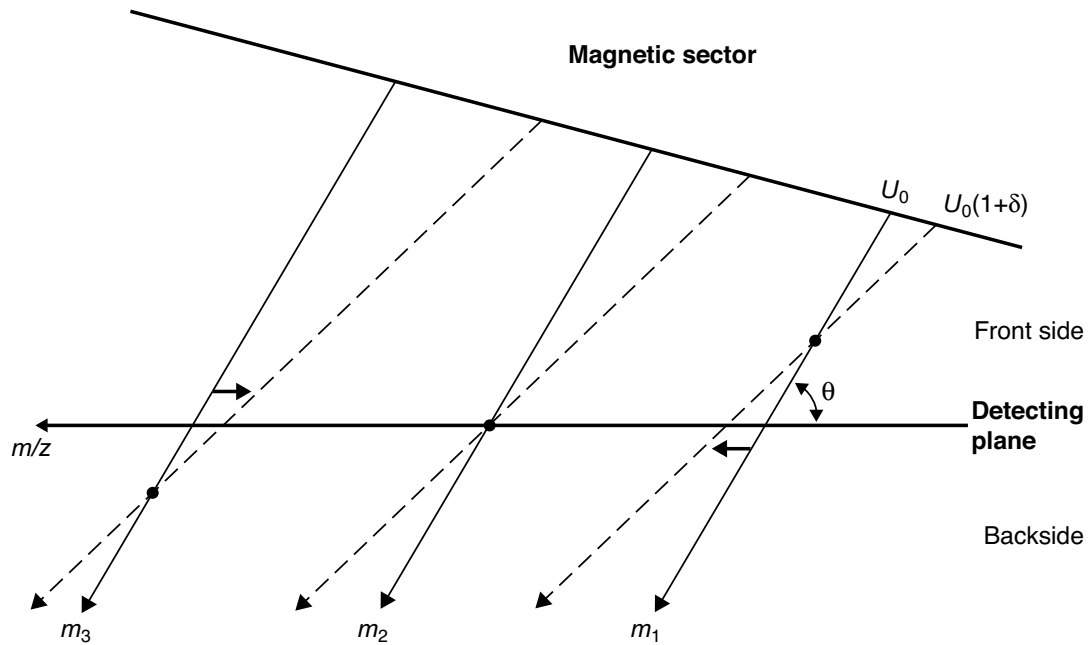


Figure 5.11: Schematic drawing of the direction of the peak shift for the fractional change of the initial energy

conditions. The region between the exit of the magnet and the detecting plane is called the front side, and the opposite side relative to the detecting plane is called the back side. Here, it will be discussed about the direction of the peak shifts when the initial energy of the ions is increased from U_0 to $U_0(1 + \delta)$. The schematic ion beams of a newly-designed ion optical system for each initial energy are shown in Figure 5.11. The ion beams of the initial energy of U_0 are shown as solid lines, and these of the initial energy of $U_0(1 + \delta)$ are break lines. For the ion beam m_1 in Figure 5.11, if the peak position shifts in the direction that the m/z value increases, the energy focusing point is in the front side of the detecting plane. For the ion beam m_2 , if the peak position does not move, the energy focusing point is on the detecting plane. For the ion beam m_3 , if the peak position shifts in the direction where the m/z value decreases, the energy focusing point moves to the back side of the detecting plane.

For the evaluation of the angular focal plane, the same method can be applied. The shape and the position of the angular focal plane can be evaluated by measuring the peak shifts when the initial angle of the ion beam is changed. When the initial angle is increased, the

direction of the peak shifts is the same as when the initial energy is increased. The initial angle of the ion beam can be changed by shifting the center of the α slit.

Moreover, the distance L_δ between the focusing points and the detecting plane along the optic axis can be roughly estimated from the peak shifts by means of the transfer matrix method. Here, a schematic drawing to explain the distance between a energy focusing point and the detecting plane along the optic axis is shown in Figure 5.12. The angle between the optic axis and the ion trajectory of its initial energy of $U_0(1 + \delta)$ is given as $(\alpha|\delta)\delta$ in the first-order by the transfer matrix method. From the geometrical consideration, the following relationship is satisfied in the first-order approximation:

$$L_\delta(\alpha|\delta)\delta = \Delta x_\delta \sin \theta \quad (5.3)$$

where Δx_δ and θ are the amount of the peak shifts in the detecting plane due to the initial energy deviation of δ and the angle between the optic axis and the detecting plane, respectively. That of the angular focusing point can be given as the same way. In consequence, These distances for the energy and angular focusing points L_δ and L_α are expressed as follows:

$$L_\delta = \frac{\Delta x_\delta \sin \theta}{(\alpha|\delta)\delta}, \quad L_\alpha = \frac{\Delta x_\alpha \sin \theta}{(\alpha|\alpha)\alpha} \quad (5.4)$$

The matrix elements of $(\alpha|\delta)$ and $(\alpha|\alpha)$ would be calculated for each peak at the corresponding mean radius in the magnetic field.

5.3.2 Dependence of the peak position on the voltage applied to the electrostatic sector

The focal planes can be evaluated by measuring the peak shifts as explained in the foregoing subsection. First, the dependence of the peak position on the voltage applied to the electrostatic sector was investigated. The peak position were measured for several voltages applied to the electrostatic sector near the theoretical one. The spectra of residual gases were observed for this purpose. The accelerating voltage of ions was 2200 V. The theoretical voltage applied to the electrostatic sector is ± 435.6 V. The voltage applied to the electrostatic sector was varied in a range from ± 435.1 V to ± 436.0 V when the accelerating voltage was fixed at 2200 V. Other experimental conditions same as the spectrum shown in Figure 5.6.

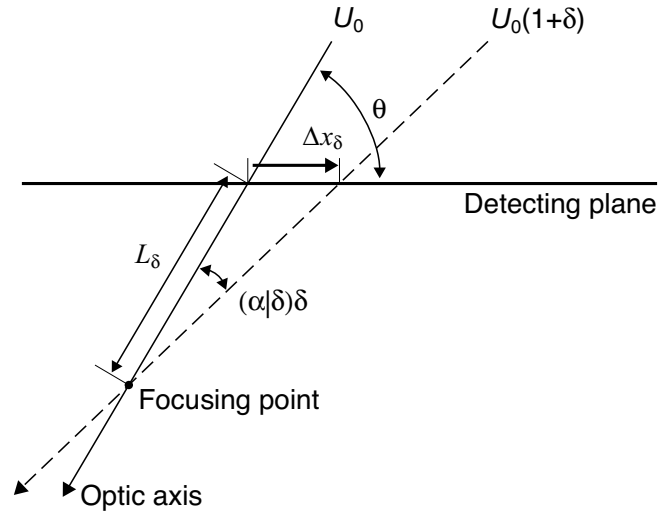


Figure 5.12: Schematic drawing of the direction of the peak shift for the fractional change of the initial energy

The peak centroid of $m/z = 28$ against the voltage applied to the electrostatic sector is shown in Figure 5.13. The straight line shows the result of the least squares fitting to a linear function applied to the data points. In this instrument, the voltage applied to the electrostatic sector can be determined within the error of 0.05 V. By the least squares fitting, the gradient of the linear function was 2.8 ± 0.2 . Consequently, the peak position would have the error caused by the determination accuracy of the voltage applied to the electrostatic sector as $\sigma_{EF} = 2.8 \times 0.05 = 0.14$ channel.

5.3.3 Temperature dependence of the peak position

The peak position is likely to be influenced by fluctuations in the temperature of the magnet, because the magnetic field strength depends on the temperature of the magnet. Generally, the permanent magnet has a negative temperature coefficient. Since the magnetic field affects the ion trajectories, the temperature of the magnet will have a significant influence on the peak position. Therefore, the dependence of the peak position on the temperature of the magnet is investigated.

A circuit system of a thermometer using a thermistor (103JT, Ishizuka Electronics Co., Tokyo, Japan) was constructed to measure the temperature of the magnetic sector. A schematic

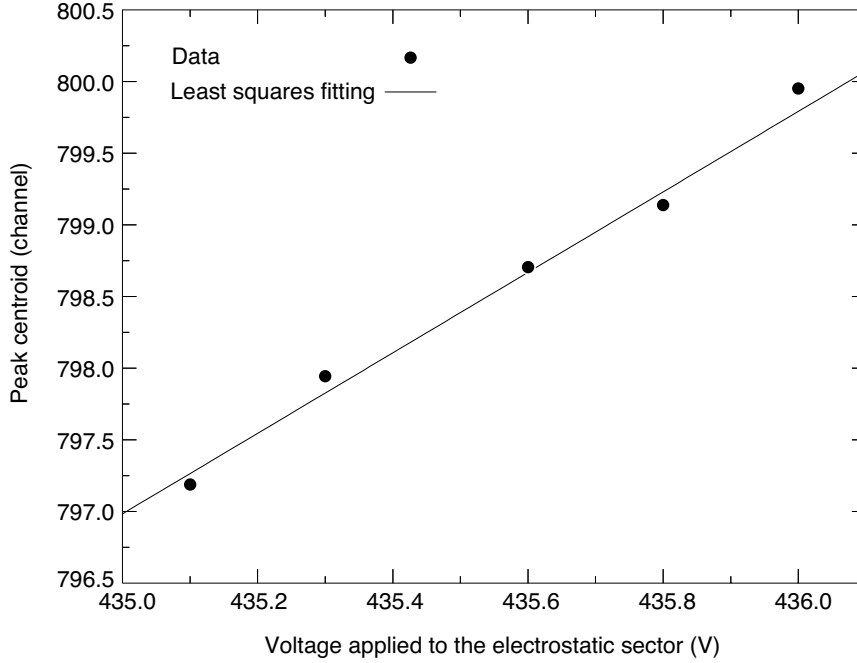


Figure 5.13: Peak position against the voltage applied to the electrostatic sector.

diagram of the circuit system is shown in Figure 5.14. The thermistor was attached to the magnetic sector in the vacuum chamber. By the circuit system, the resistance of the thermistor is displayed in a digital panel meter. The relation between the resistance and the absolute temperature of a thermistor is expressed as follows [5.4]:

$$R(T) = R_0 \exp \left[B \left(\frac{1}{T} - \frac{1}{T_0} \right) \right] \quad (5.5)$$

where $R(T)$, R_0 and B are the resistance at temperature T , the resistance at temperature T_0 , and a constant depending on the material of the thermistor, respectively. From the specification data of the thermistor 103JT [5.4], $B = 3435$ K and $R_0 = 10$ k Ω at $T_0 = 25$ °C are given. Accordingly, the resistance of the thermistor could be converted to the temperature by eq. 5.5.

The spectra of the residual gases were observed to measure the fluctuation of the peak position by the temperature of the magnetic sector. The experimental conditions are same as the spectrum shown in Figure 5.6. Many spectra were observed at different temperatures. The peak centroid position of m/z 28 expressed with the CCD channels is plotted against the temperatures in Figure 5.15. The errors show the sum of σ_{EF} and the mean square errors of

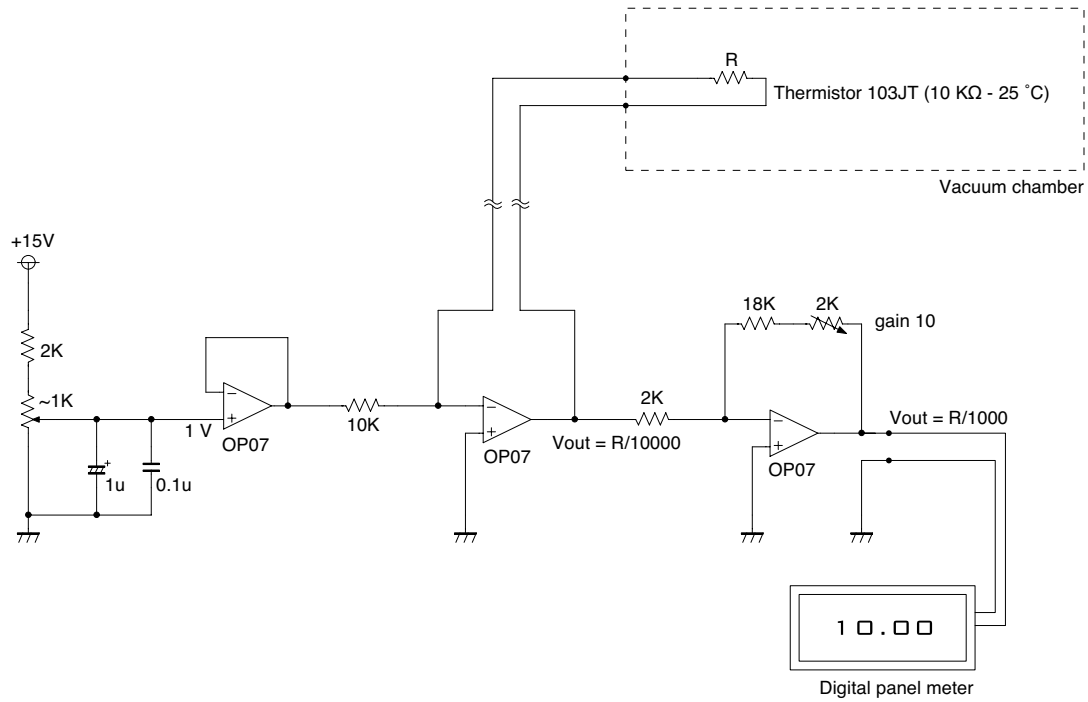


Figure 5.14: Schematic diagram of the thermometer circuit system

five consecutive measurements . For a typical permanent magnet, the magnetic flux density is expressed as:

$$B(T) = B_0 \{1 - \eta(T - T_0)\} \quad (5.6)$$

where T , T_0 , B_0 and η respectively denote an arbitrary temperature, a standard temperature, a magnetic flux density at the standard temperature and the temperature coefficient. If the accelerating voltage is fixed, the radius of the trajectory in the magnetic field is, as is well known, in inverse proportion to the magnetic field strength. Thus, the peak centroid position can also be fitted as a function that is inversely proportional to the magnetic field strength. In short, the relationship between peak centroid position and the temperature of the magnet can be expressed as follows:

$$x = \frac{a}{b - cT} \quad (5.7)$$

where a , b and c denote the fitting coefficients, and x and T respectively denote the peak centroid channel and the temperature of the magnetic sector. The result of the least squares

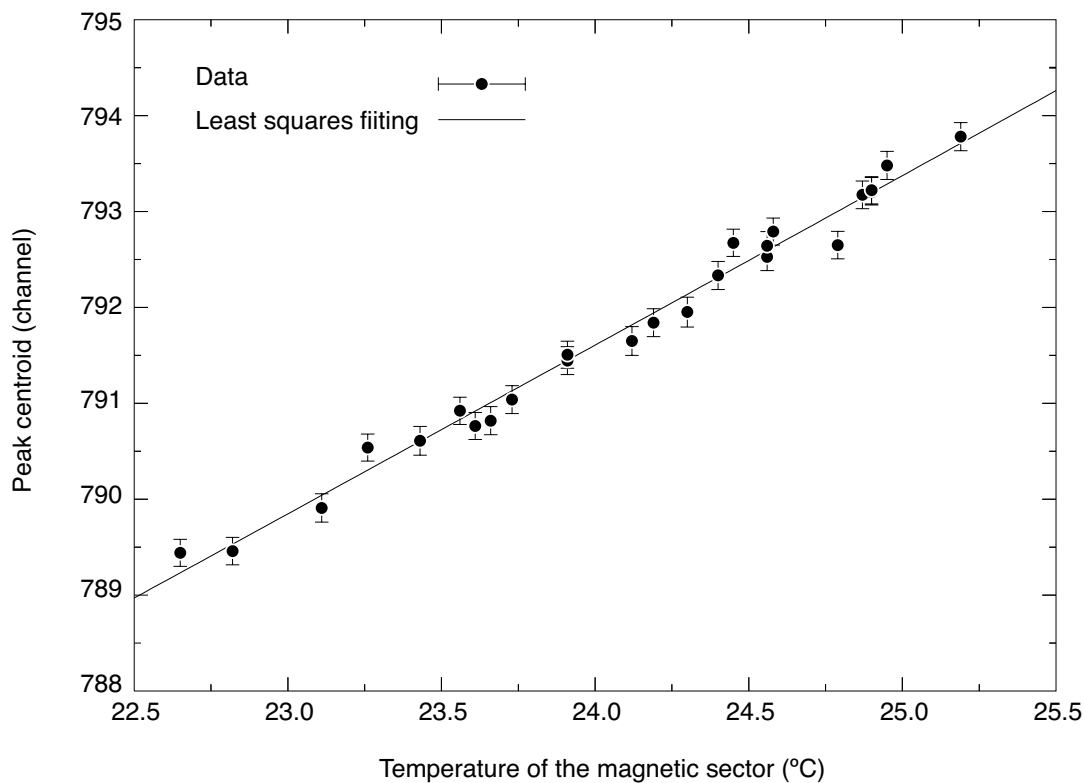


Figure 5.15: Peak position against the temperature of the magnetic sector

fitting applied to the data points is also shown in Figure 5.15. The temperature coefficient was experimentally derived as -0.1% at $20\text{ }^{\circ}\text{C}$. This result is in agreement with the specification data of the Neomax 39SH of -0.11% at $20\text{ }^{\circ}\text{C}$.

The experimental results show that the peak position strongly depends on the temperature of the magnet, indicating that temperature correction is essential for the measurement of a meaningful peak shift if the fluctuation of the temperature of the magnetic sector is significant.

5.3.4 Evaluation of the energy and the angular focal planes

Experimental

The spectra of the residual gases were also observed for evaluation of the energy focal plane. When the accelerating voltage of ions is 2200 V , six peaks of m/z 14, 16, 17, 18, 28 and 32 can be observed simultaneously, as already shown in Figure 5.6. However, there

are only two peaks in the region from 400 – 1000 channels and no peaks in the region from 400–700 channels under these experimental conditions. For the evaluation of the focal plane, the peaks should be observed in the overall detecting plane. When the accelerating voltage is 3000 V, peaks of m/z 14, 16, 17 and 18 are observed in the region from 350 – 700 channels. Also, when the accelerating voltage is 3800 V, these four peaks are observed in the region from 600 – 1000 channels. Thus, the spectra were observed at three different accelerating voltages of 2200 V, 3000 V and 3800 V. When the accelerating voltages of ions are 2200 V, 3000 V and 3800 V, the theoretical values of the voltages applied to the electrostatic sector are ± 435.6 V, ± 594.0 V and ± 752.4 V, respectively. At each accelerating voltage of V , the peak shifts were measured when the accelerating voltage was switched from V to $V(1+0.005)$ while the voltages applied to the electrostatic sector were fixed.

For the evaluation of the angular focal plane, the spectra of residual gases were observed at acceleration voltages of 2200 V, 3000 V and 3800 V, the same as in the case of the energy focal plane. The center of the α slit was shifted by 0.2 mm in the horizontal direction to change the initial angle of the ion beam. The initial angle is increased 0.006 radian by this shift of the α slit. At each of the accelerating voltages, the peak shift was measured when the initial angle of the ion beam was increased by 0.006 radian.

Results and discussion

The shifts of the peaks with the temperature correction are plotted against the peak centroid positions in Figure 5.16. The circles show the peak shifts when the initial energy was increased by $\delta = 0.005$, and the squares show those when the initial angle of the ion beam was increased by 0.006 radian. The mean radius in the magnetic field corresponding to the channel number of the peak position is also shown in Figure 5.16. If the peak position moved with increased channel number, it would show that the peak position moves as the m/z value increases. In Figure 5.16, the peak shifts in the range from 300 – 1000 channels are nearly equal to zero for both the energy and the angular deviations, indicating that double-focusing is sufficiently achieved in this range of the detector plane. Small positive shifts of peaks are observed in the range from 0 – 300 channels. This shows that the focal planes are curved toward the magnet.

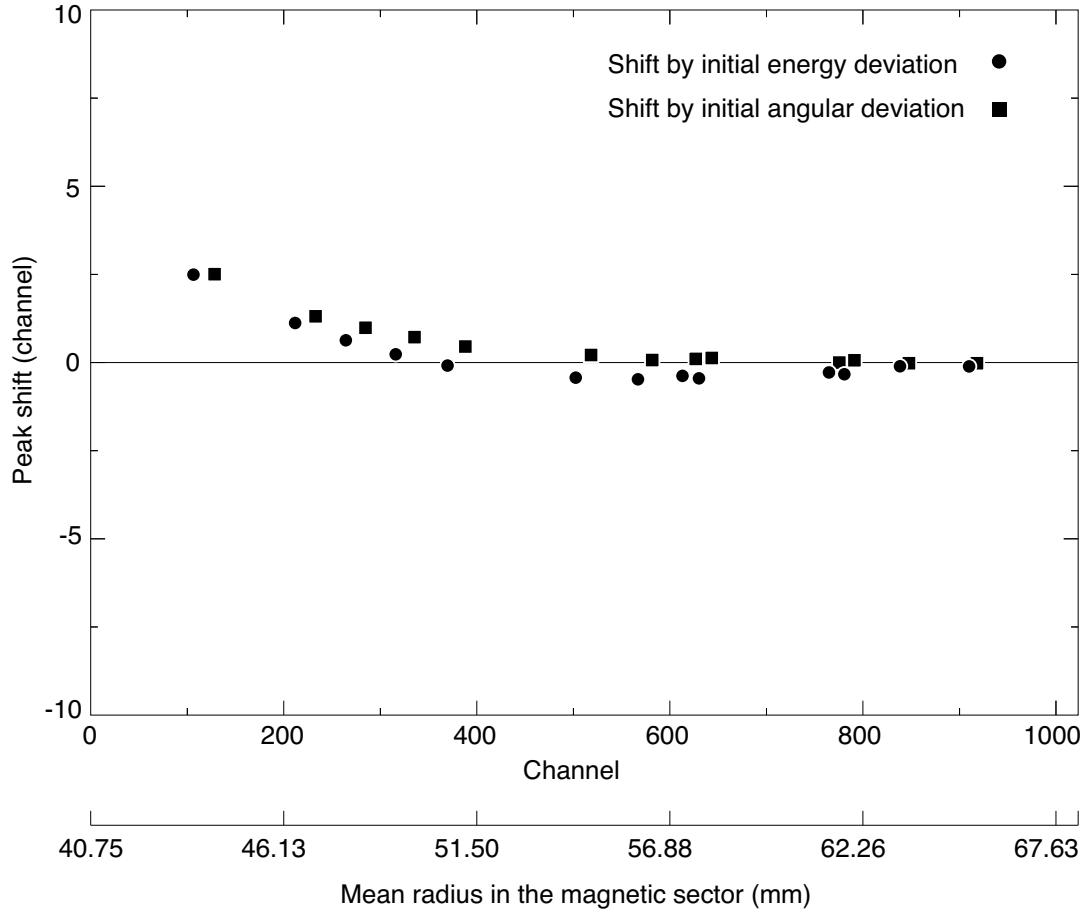


Figure 5.16: Peak shifts when the initial energy or the initial angle is fractionally increased

The positions of the energy and angular focusing points relative to the detecting plane were estimated by eq. ???. The matrix elements of $(\alpha|\delta)$ and $(\alpha|\alpha)$ were calculated for each peak by TRIO 2.0. The positions of these focusing points are shown in Figure 5.17. The corresponding mean radii in the magnetic sector and the schematic configuration of the magnetic sector are also shown in Figure 5.17.

It was confirmed that the energy and angular focal planes sufficiently coincide with each other and are along a straight line in the range of more than 50 mm of the mean radii of the magnetic field. The focal planes curve slightly toward the magnetic sector relative to the detecting plane in a range of less than 50 mm of the mean radii of the magnetic field.

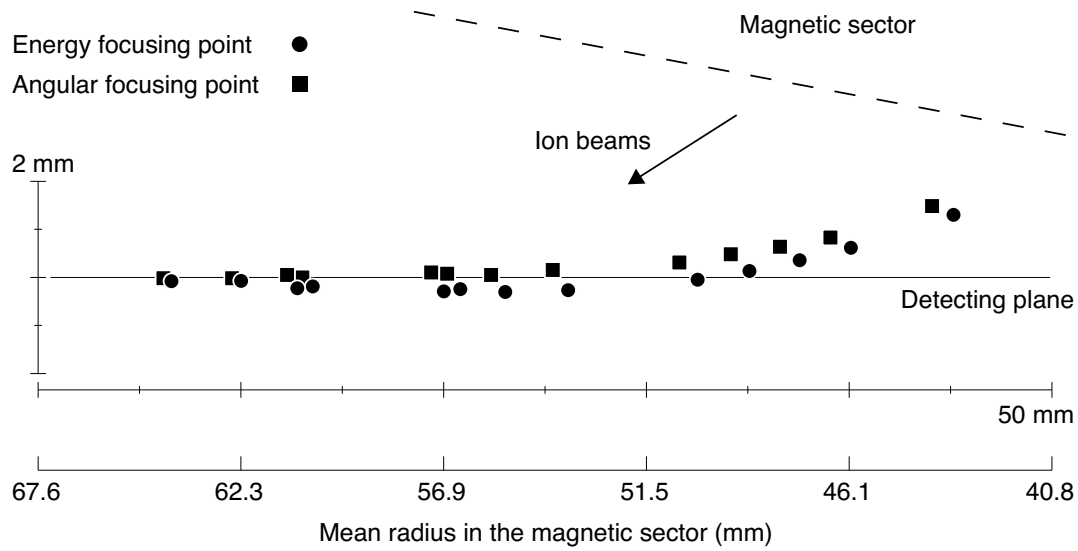


Figure 5.17: Energy and angular focusing points estimated from the peak shifts

5.4 Measurement of a second-order element of the transfer matrix ($x|\delta\delta$)

If energy focusing is achieved, i.e., the first-order element of the transfer matrix ($x|\delta$) is equal to zero, the deviation of the trajectories depending on the value of δ is proportional to δ^2 . Thus, by measuring the deviation x for several values of δ , the second-order element of the transfer matrix ($x|\delta\delta$) can be obtained experimentally as a coefficient of δ^2 .

The spectra of the residual gases were observed for the measurement of ($x|\delta\delta$). First, the voltage applied to the electrostatic sector was adjusted at the theoretical value of ± 465.3 V for the accelerating voltage of 2350 V. The spectra of residual gases were then observed at the accelerating voltages in steps of 5 V from 2330 V to 2370 V while the voltage applied to the electrostatic sector was fixed. This scan range of the accelerating voltage corresponds to a range of δ from -0.0085 to 0.0085 .

The deviation of the ion trajectories in the profile plane is estimated from the shift of the peak centroid by considering the angle between the ion beam and detecting plane. The deviation of the ion trajectories in the x direction is plotted against δ in Figure 5.18. A quadratic function of the least squares fitting applied to the data points is also shown in

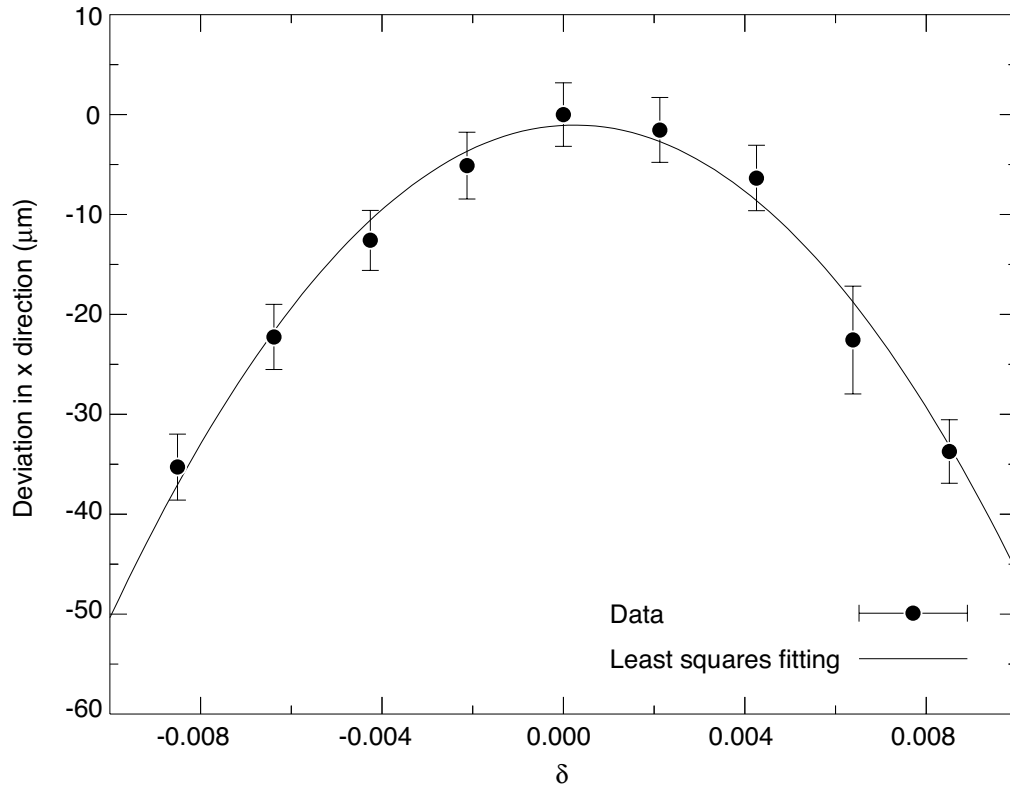


Figure 5.18: Deviation of ion trajectories against δ . The least squares fitting was applied to the data points as a quadratic function.

Figure 5.18. The second order coefficient of the fitting function is -0.47 ± 0.03 m. This result is in good agreement with the simulation by TRIO 2.0 of -0.44 m.

5.5 Simulation of the ion trajectories in the magnetic sector

The experimental results of the evaluation of the focal planes indicate the minimal curve of the focal planes. In this ion optical system, the fringing field of the magnet exit is likely to considerably influence the focal planes. Although the TRIO 2.0 computer program can analytically take into account the influence of the fringing field for several determined shapes in third order approximations, it is unable to calculate the influence of the fringing field of our newly-designed magnet. A ray tracing method would be more effective in this case. Therefore, the magnetic field and ion trajectories in the magnetic sector were simulated by a ray tracing method for comparison with the experimental result. The calculation of the magnetic field was carried out by employing the 'ELECTRA' computer program [5.5]. This program can calculate electric potential and electric field in three dimensions using the charge density method [5.6]. In the charge density method, the surface of the electrode is divided into elements to approximate the continuous charge distribution. The electric potential and field can be obtained by integrating the contribution of the charges on each element. The electric potential calculated by the charge density method will exactly satisfy Laplace's equation in principle.

If there is no saturation of the magnetic material in the magnetic circuit, the static magnetic field can be calculated by the program for calculating the electric field according to the following principle. If the currents do not exist, the magnetic field \mathbf{H} satisfies the Maxwell equations as follows.

$$\operatorname{div} \mathbf{H} = 0 \quad (5.8)$$

$$\operatorname{rot} \mathbf{H} = 0 \quad (5.9)$$

Equation 5.9 indicates that the magnetic field \mathbf{H} can be defined with the magnetic scalar potential ϕ_m as:

$$\mathbf{H} = -\operatorname{grad} \phi_m \quad (5.10)$$

Substitution of eq. 5.10 into eq. 5.8 yields:

$$\nabla^2 \phi_m = 0 \quad (5.11)$$

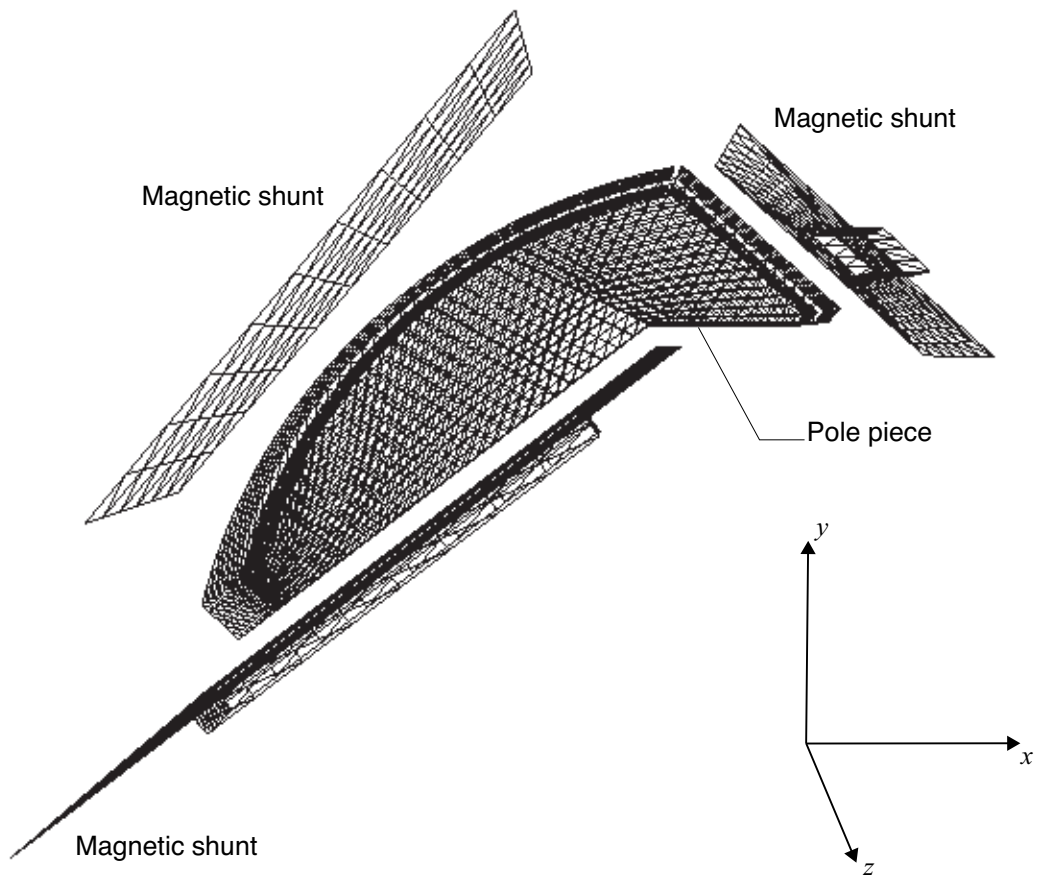


Figure 5.19: Mesh of the magnet and the magnetic shunts generated by ELECTRA.

Equation 5.11 shows that the magnetic scalar potential ϕ_m obeys Laplace's equation, as does the electric potential. Therefore, the magnetic scalar potential and field can be calculated by the charge density method for the electric field calculation.

Here, the simulation of the magnetic field by ELECTRA is described. Figure 5.19 shows the generated mesh of the magnet and the magnetic shunts. The mesh consists of 2498 nodes. The contour map of the magnetic flux density in z -direction on the median plane is shown in Figure 5.20. The contour map of the magnetic scalar potential in the cross section A-B of Figure 5.20 is shown in Figure 5.21. The distribution of the magnetic flux density along the cross section A-B in Figure 5.20 is also shown in Figure 5.22. The simulated distribution is shown as the solid line and the measurements are plotted as circles in Figure 5.22. The magnetic flux density was practically measured without the magnetic shunt of the

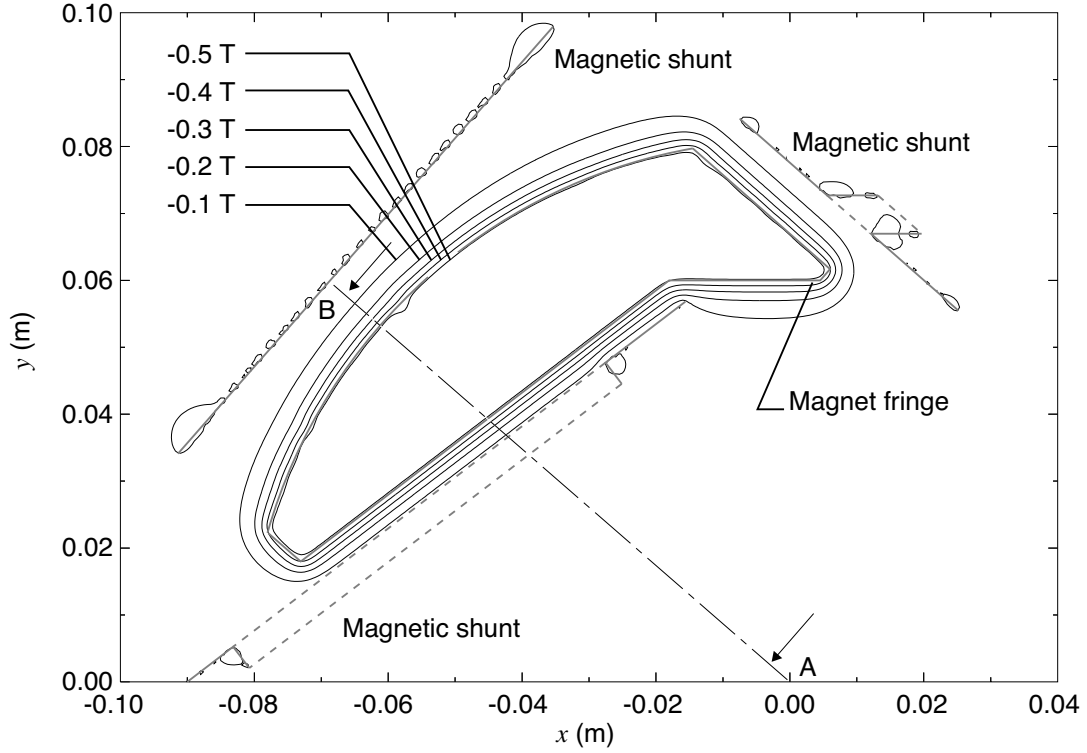


Figure 5.20: Contour map of the magnetic flux density in z -direction simulated by ELEC-TRA.

exit fringe of the magnet. The simulation in Figure 5.22 was, therefore, executed without the magnetic shunt of the exit fringe. The simulated magnetic field shows good agreement with the measurements. The simulation result and the measurements, moreover, show sufficiently high uniformity of magnetic field strength in the area where ions pass through.

Then, ion trajectories were simulated in this calculated magnetic field. The integration of the equation of motion was carried out by means of a fourth-order Runge-Kutta method. Ion trajectories were simulated for mean radii of 35 – 70 mm at 5 mm intervals. In principle, an ion's trajectory in an electrostatic field does not depend on its m/z value. In consequence, the starting points of each trajectory was set at the exit of the electrostatic sector. The initial positions and angular deviations were calculated using the transfer matrix method. Ion trajectories with initial energy deviations of $\delta = 0$ and $\delta = 0.005$ were simulated for each mean radius to evaluate the energy focusing points. Ion trajectories with initial angular deviations of $\alpha = 0$ and $\alpha = 0.006$ radian were also simulated to evaluate the angular focusing

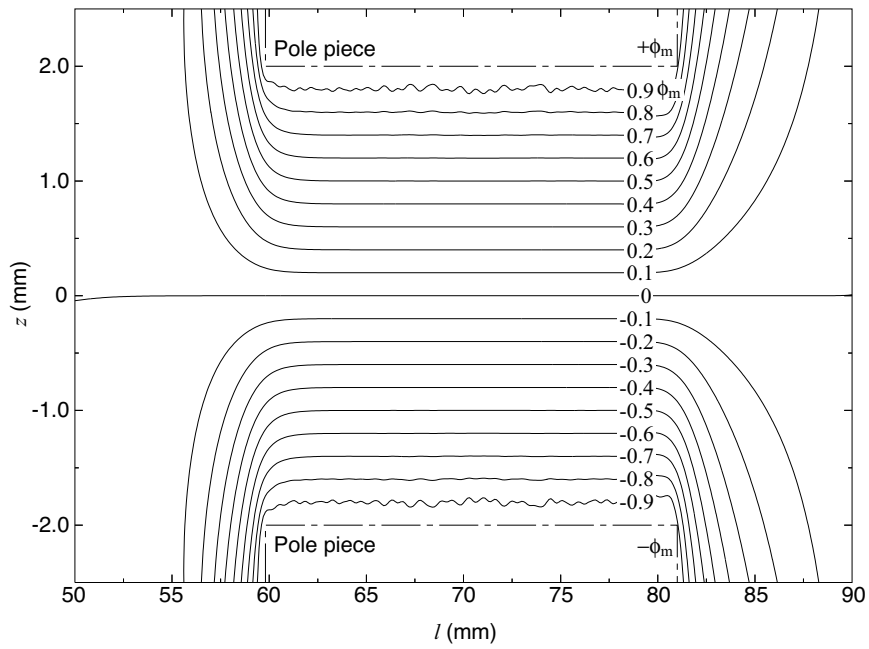


Figure 5.21: Contour map of the magnetic scalar potential in the cross section A-B in Figure 5.20.

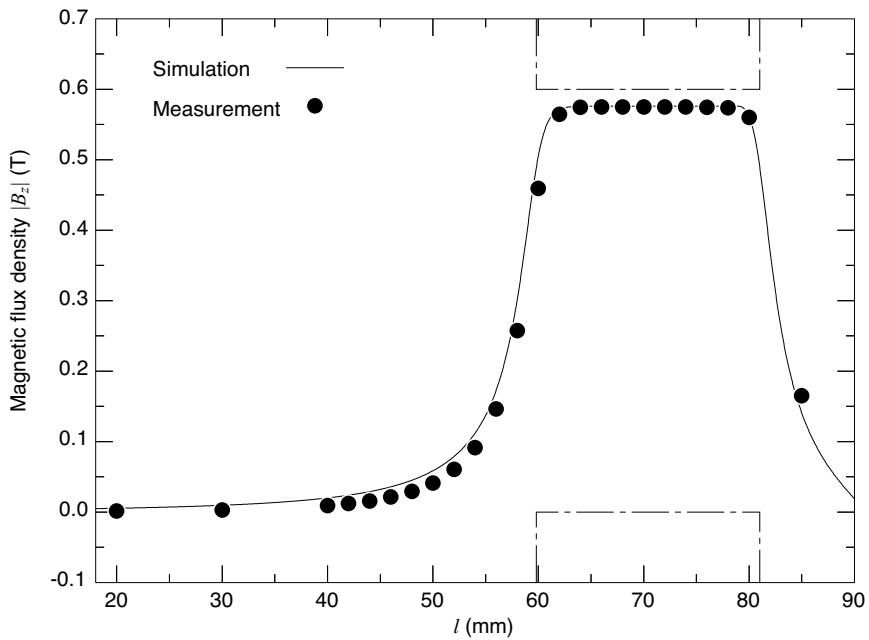


Figure 5.22: Distribution of the magnetic flux density along the cross section A-B in Figure 5.20.

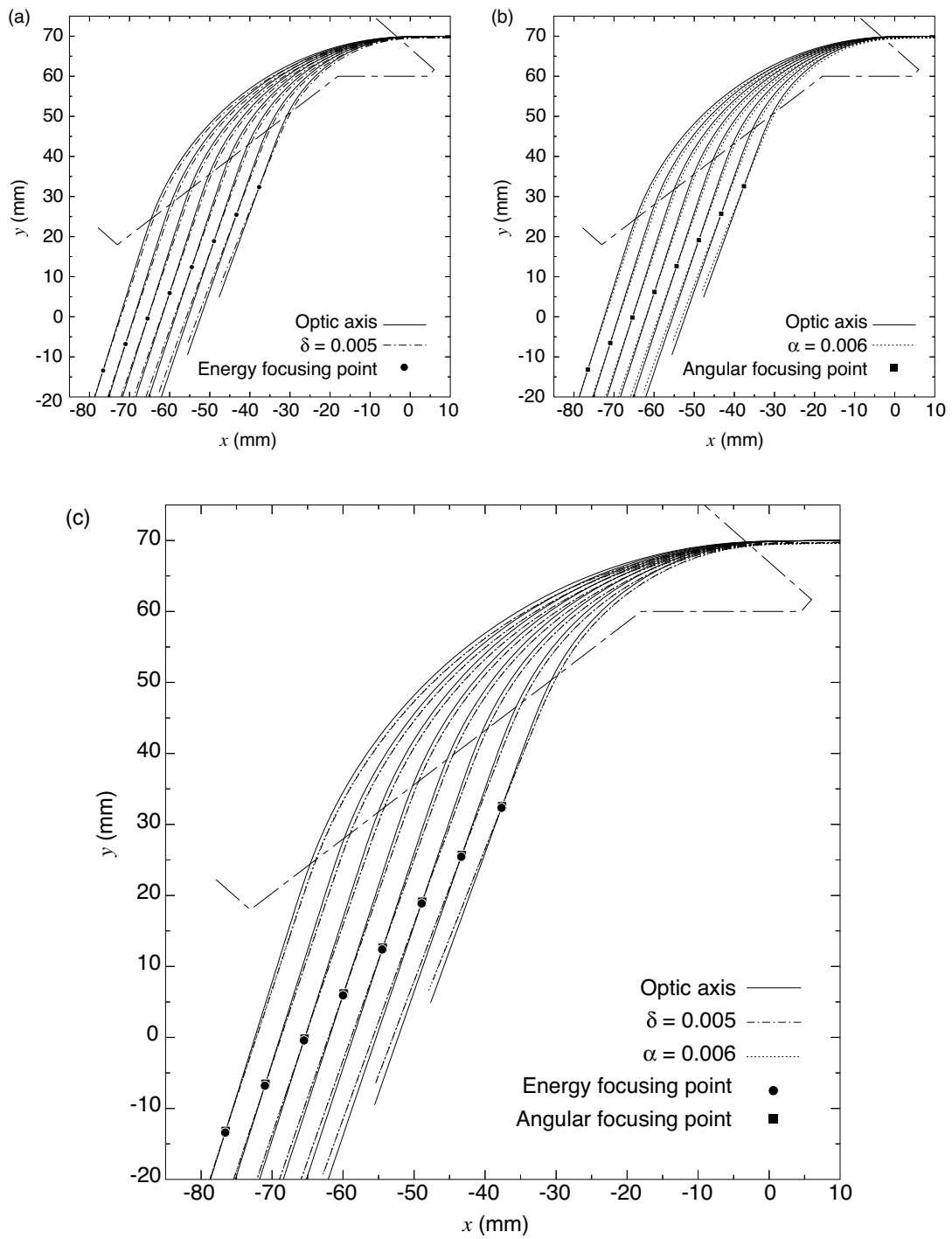


Figure 5.23: Ion trajectories and focusing points simulated by ELECTRA. (a) energy focusing points, (b) angular focusing points, and (c) both of them are overlaid.

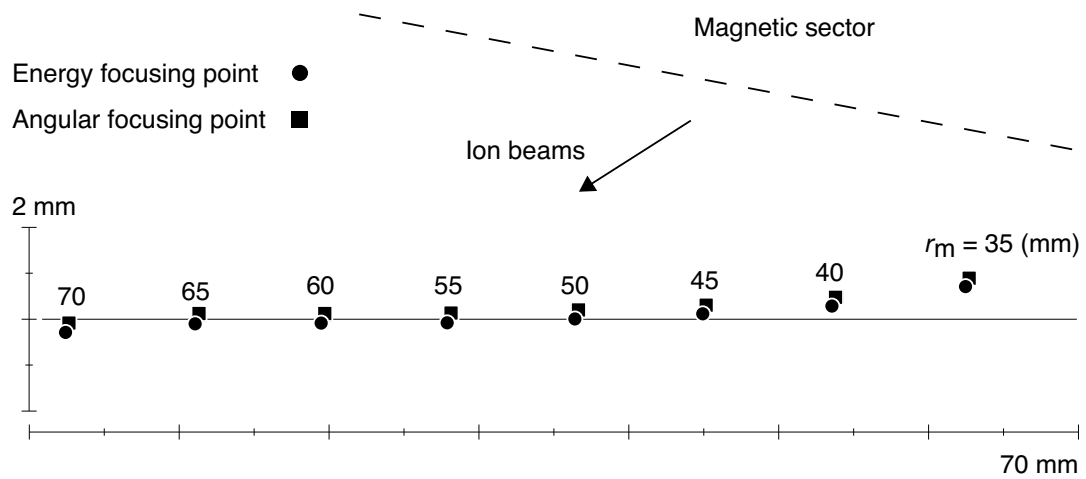


Figure 5.24: Energy and angular focusing points simulated by ELECTRA

points. Ion trajectories and the focusing points for both cases are shown in Figure 5.23. The expanded plots of the focusing points are shown in Figure 5.24.

The energy and the angular focusing points sufficiently coincide with each other along a straight line. Moreover, the simulated focal planes slightly curve toward the magnet as observed in the experimental results as shown in Figure 5.17. It was confirmed the following two points both experimentally and by simulation:

- The double-focusing is sufficiently achieved along a straight line.
- The focal planes curve slightly toward the magnet as the mean radii in the magnetic field decrease.

5.6 Evaluation of the quantitative performance

The quantitative performance is the most essential feature of the instrument. The characteristics of the focal plane detector significantly affect it in this mass spectrograph. In this section, the evaluation of the quantitative performance is described. The dynamic range of the simultaneous detection was evaluated by observing spectra of krypton and neon [5.7]. Furthermore, the distribution of the gain in the detector was investigated.

5.6.1 Dynamic range of the simultaneous detection

The 2D spectra of krypton and neon were observed to evaluate the dynamic range of the simultaneous detection. First, the 2D and 1D spectrum of krypton is shown in Figure 5.25. The experimental conditions were as follows. The background pressure was 4.0×10^{-4} Pa in the vacuum chamber, and the pressure was increased to 1.3×10^{-3} Pa when krypton gas was introduced. The accelerating voltage of ions was 800 V. The voltage applied to the electrostatic sector was ± 158.4 V. The electron energy and the electron current for ionization were 70 eV and 250 μ A. The voltage applied to the MCP and the phosphor layer was 1.0 kV and 4.0 kV. The operation mode of the CCD was the pixel binning and the exposure time of the CCD was 1.0 s. The 2D spectrum shown in Figure 5.25(a) is expanded around the spectrum of krypton. The 1D spectrum shown in Figure 5.25(b) was obtained by accumulating the lines from 30 to 120 of the 2D spectrum in the vertical direction.

All the stable isotopes of krypton are observed simultaneously without saturation of the CCD. The ratios of peak areas were calculated; their peak areas are shown in Table 5.1. The peak area was calculated by integrating the intensity in twice peak width at 5% peak height. The errors show mean square errors of five consecutive measurements. Each peak area ratio (the roughly estimated isotope ratio) agrees with the standard isotope ratio [5.8] within a deviation of 30%. A dynamic range of 200 was obtained from the $^{78}\text{Kr}/^{84}\text{Kr}$ ratio.

Then, the 1D spectrum of neon is shown in Figure 5.26. The experimental conditions are as follows. The background pressure was 4.0×10^{-4} Pa in the vacuum chamber, and the pressure was increased to 1.3×10^{-3} Pa when neon gas was introduced. The accelerating voltage of ions was 3050 V. The voltage applied to the electrostatic sector was ± 609.3 V.

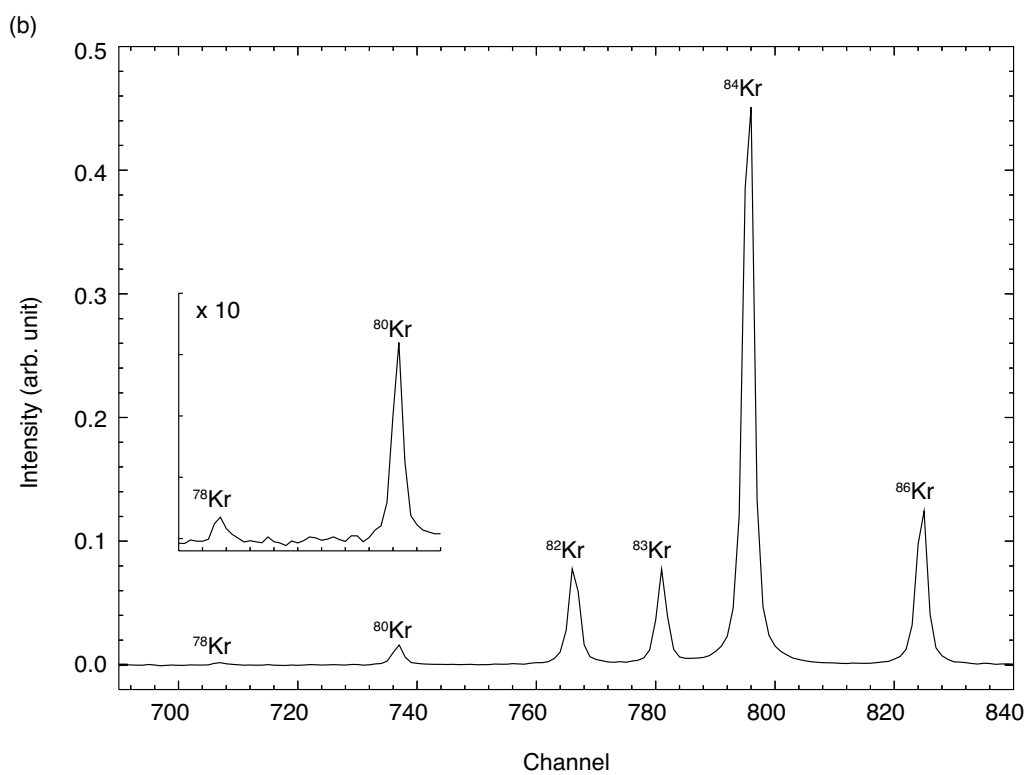
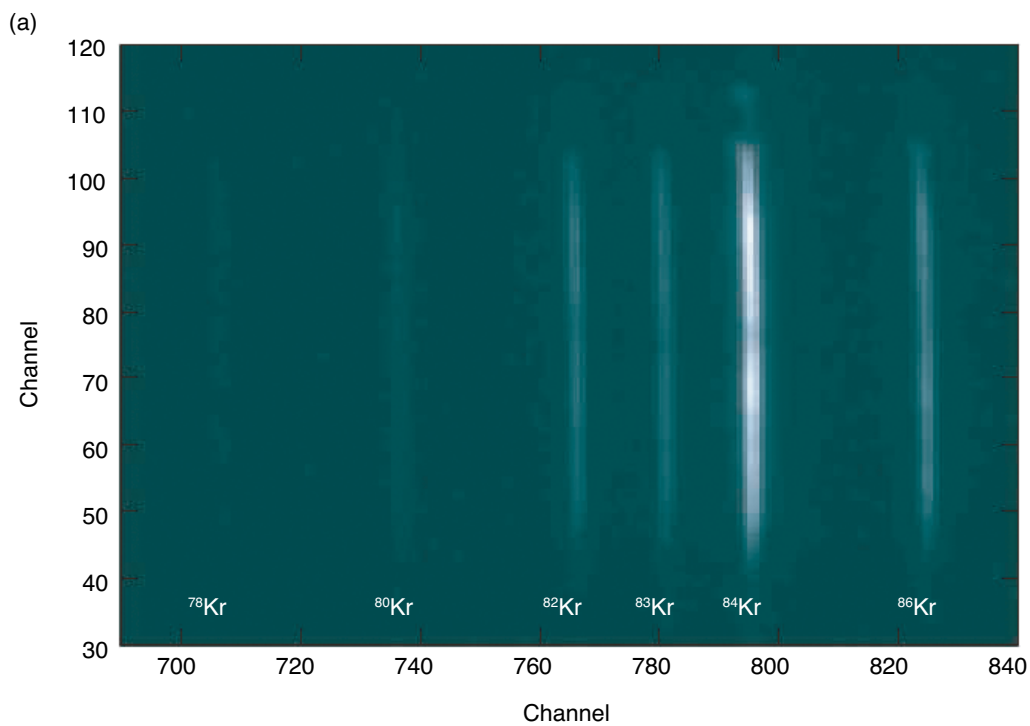


Figure 5.25: (a) 2D and (b) 1D spectrum of krypton. The 1D spectrum was obtained by accumulating the lines from 30 to 120 of the 2D spectrum

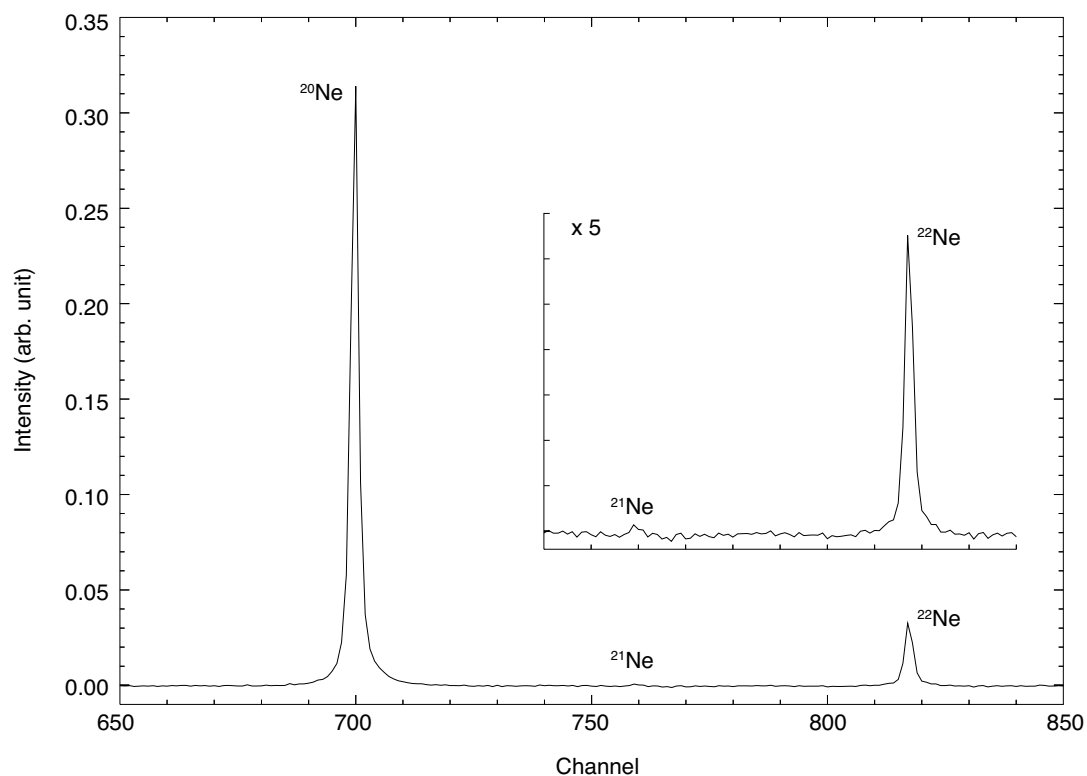


Figure 5.26: 1D spectrum of neon. The spectrum was obtained by accumulating the lines from 30 to 120 of the 2D spectrum

The electron energy and the electron current for the ionization were 70 eV and 250 μA . The voltages applied to the MCP and the phosphor layer were 0.9 kV and 4.0 kV. The operation mode of the CCD was pixel binning and the exposure time of the CCD was 1.0 s. The 1D spectrum was obtained by accumulating lines 30 to 120 of the 2D spectrum in the vertical direction. All the stable isotopes of neon were observed simultaneously without saturation of the CCD, although the signal-to-noise ratio of the ^{21}Ne peak was not sufficient. The ratios of peak areas were calculated. These ratios of peak areas are also shown in Table 5.1. The errors show mean square errors of five consecutive measurements. These roughly estimated isotope ratios agree with the standard values [5.8] within a deviation of 6%. In addition, a dynamic range of 300 was achieved with the $^{21}\text{Ne}/^{20}\text{Ne}$ ratio.

Table 5.1: Peak area ratios of krypton and neon

	Peak area ratio	Standard isotope ratio
$^{78}\text{Kr}/^{84}\text{Kr}$	0.0041 ± 0.0002	0.0062
$^{80}\text{Kr}/^{84}\text{Kr}$	0.0336 ± 0.0002	0.0401
$^{82}\text{Kr}/^{84}\text{Kr}$	0.173 ± 0.001	0.2034
$^{83}\text{Kr}/^{84}\text{Kr}$	0.156 ± 0.001	0.2018
$^{86}\text{Kr}/^{84}\text{Kr}$	0.276 ± 0.002	0.3032
$^{21}\text{Ne}/^{20}\text{Ne}$	0.0031 ± 0.0003	0.0030
$^{22}\text{Ne}/^{20}\text{Ne}$	0.1087 ± 0.0006	0.1022

5.6.2 Gain distribution in the detector

The inhomogeneity of the distribution of the gain in the focal plane detector has seriously influence on the measurement of the isotope ratio because the peaks for each mass are observed at different positions in the detector. For evaluation of the gain distribution, spectra of neon were observed for several detector positions.

The experimental conditions are as follows. The background pressure was 3.0×10^{-4} Pa in the vacuum chamber, and the pressure was increased to 6.9×10^{-4} Pa when neon gas was introduced. The accelerating voltage of ions was 3000 V. The voltage applied to the electrostatic sector was ± 594.0 V. The electron energy and the electron current for the ionization were 70 eV and $300 \mu\text{A}$. The voltages applied to the MCP and the phosphor layer were 0.8 kV and 4.0 kV. The operation mode of the CCD was pixel binning and the exposure time of the CCD was 1.0 s. The 1D spectrum was obtained by accumulating lines 10 to 120 of the 2D spectrum in the vertical direction. The experimental conditions at each position of detector were fixed at above values. The detector position was mechanically moved to observe the peaks at different channels in the detector. The detector position was shifted only in lateral direction while the detector angle is retained.

The peak areas for each detector position are shown in Figure 5.27. Here, the peak area was obtained by integrating the intensity in twice peak width at 5% peak height as same as the previous subsection. The peak position in the detecting plane is represented by the peak

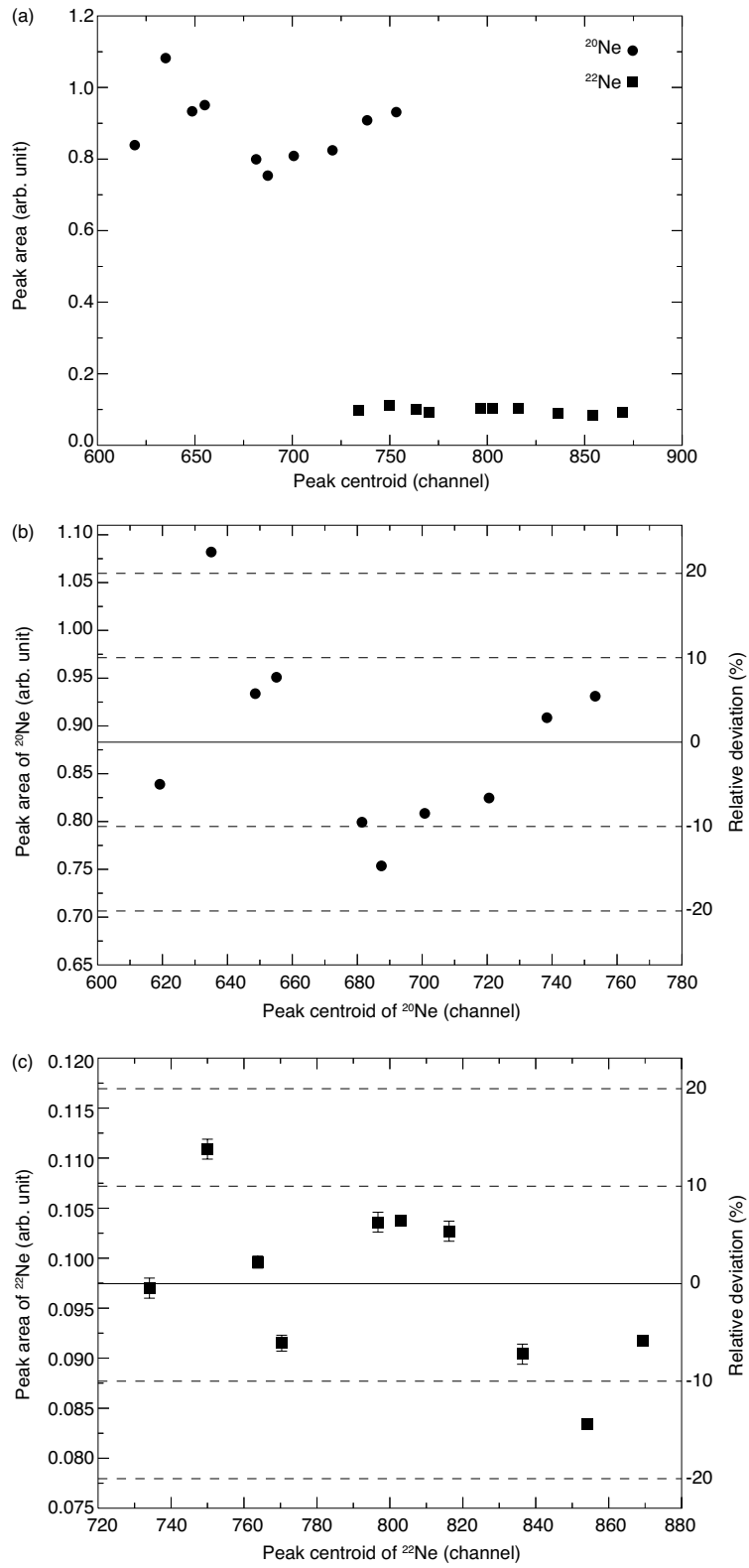


Figure 5.27: Peak areas of ^{20}Ne and ^{22}Ne for each detecting position.

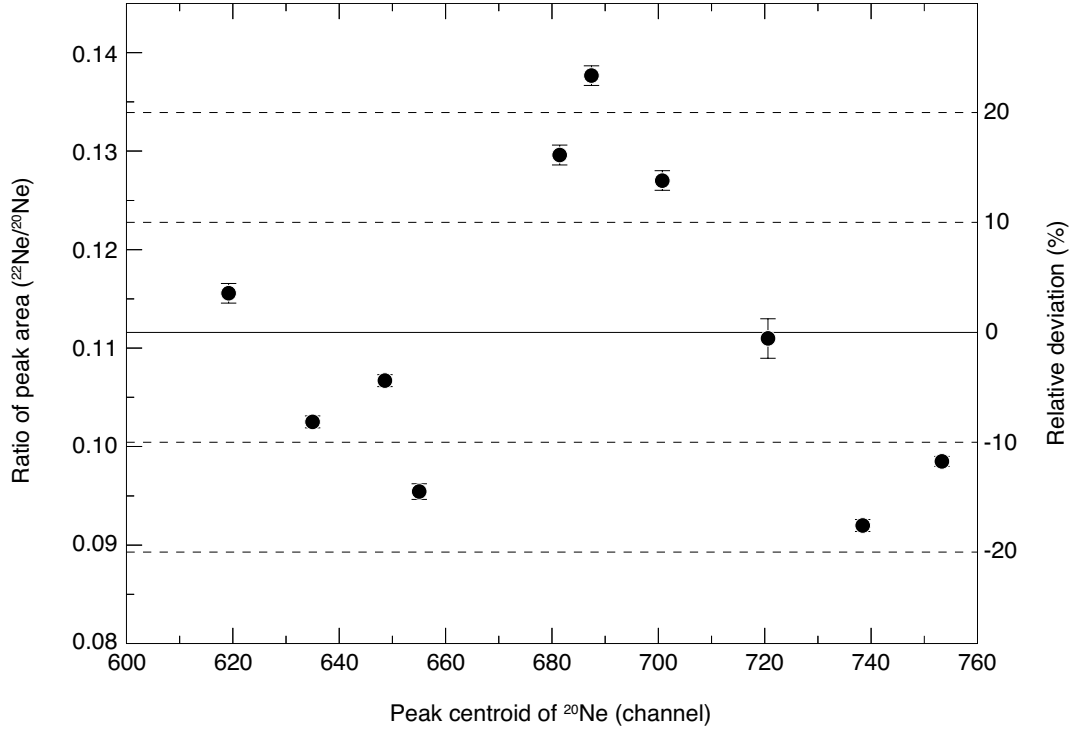


Figure 5.28: Peak area ratio of $^{22}\text{Ne}/^{20}\text{Ne}$ for each detecting position.

centroid. Figure 5.27(a) is the plots of the peak areas against the peak centroid of ^{20}Ne and ^{22}Ne . Figure 5.27(b) and (c) shows the expanded plots of Figure 5.27(a) for ^{20}Ne and ^{22}Ne , respectively. The experimental result shows that the peak area fluctuated about 40% by the detecting position of the peak. The peak area ratios for each detecting position are shown in Figure 5.28. The peak area ratios of $^{22}\text{Ne}/^{20}\text{Ne}$ are plotted against the peak centroid of ^{20}Ne . The peak area ratios also fluctuated about 40% by the detecting position. This indicates that the employed focal plane detector has a large inhomogeneity of the distribution of the gain.

Then, the reproducibility and the linearity of the gain were evaluated when the detecting position is fixed. Spectra of neon were observed at a fixed position in the detector. The experimental conditions without the pressure are same as the previous experiment. The amount of neon gas introduced in the vacuum chamber was changed. The pressures were from 4.9×10^{-4} Pa to 1.0×10^{-3} Pa when neon gas was introduced. Moreover, the spectra were observed at a constant temperature because the peak position is affected by the temperature of the magnet as already described. The peak areas of ^{22}Ne against those of ^{20}Ne are plotted in Figure

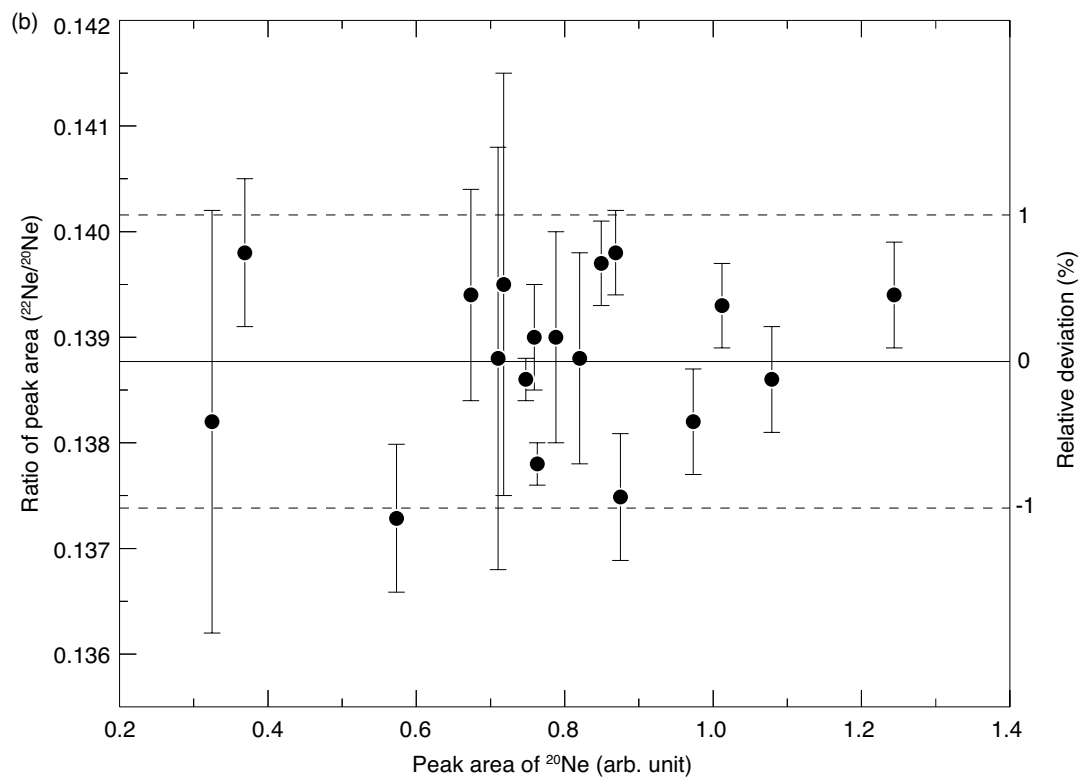
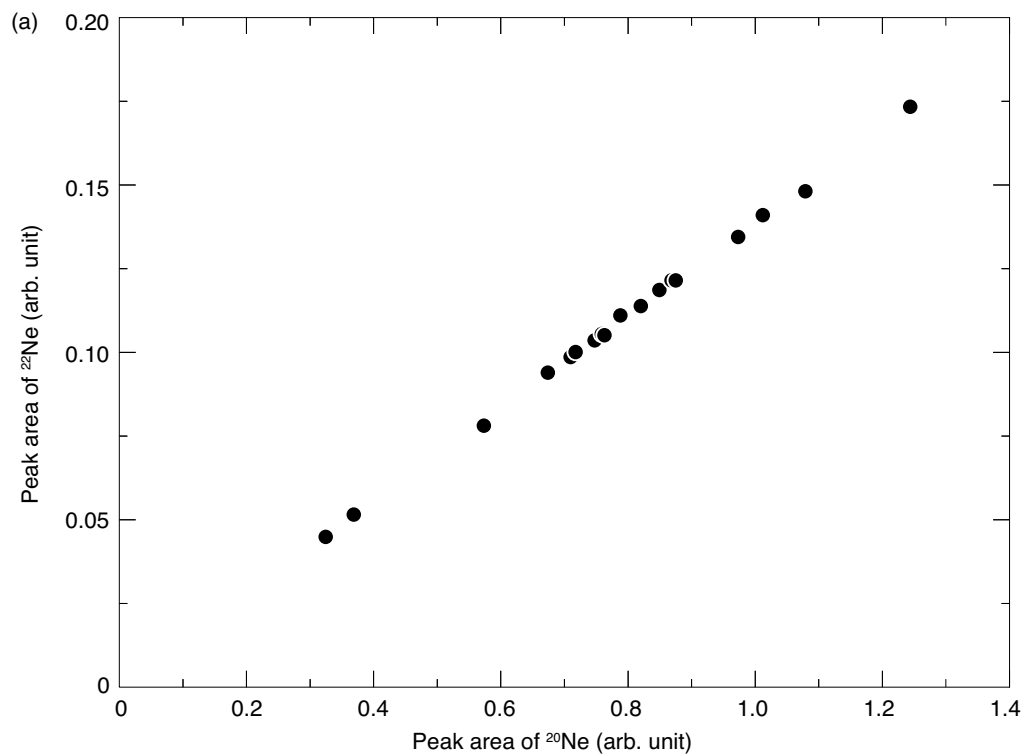


Figure 5.29: (a) Peak area of ^{22}Ne against that of ^{20}Ne . (b) Peak area ratio of $^{22}\text{Ne}/^{20}\text{Ne}$ at fixed detecting position.

5.29(a), and the peak area ratios of $^{22}\text{Ne}/^{20}\text{Ne}$ against the peak area of ^{20}Ne are shown in Figure 5.29(b). The temperatures of the magnet were from 24.77 °C to 24.85 °C, and the peak centroid of ^{20}Ne was from 621.58 channels to 621.62 channels for all the measurements. This shift of the peak can be negligible. The peak area ratios are measured within a relative deviation of 2%. This result shows that a sufficiently useful reproducibility and linearity of the gain can be achieved when the detecting position is fixed.

The experimental result for the evaluation of the gain distribution in the employed focal plane detector showed serious inhomogeneity. However, a sufficiently useful reproducibility and linearity of the gain was confirmed when the detecting position is fixed. This indicates that the calibration of the gain distribution in the overall detecting plane is essential for the measurement of the isotope ratio. If the gain distribution would be calibrated, the instrument could provide high sensitive and good quantitative analyses.

5.7 Conclusion

The performance of the newly designed and constructed instrument was investigated. The mass resolution of 130 was achieved with the main slit width of 0.25 mm. This result agreed with the simulation using the transfer matrix method. The experimental value of the detectable m/z range was also consistent with the calculated value. The energy and the angular focal planes were evaluated experimentally. Double-focusing was successfully achieved along a straight line. The focal planes, however, curve slightly toward the magnet as the mean radii in the magnetic field decrease. These focal planes were also evaluated by the simulation to compare with the experimental result. The energy and angular focusing points were simulated by the ray-tracing method. The magnetic field was simulated by ELECTRA using the charge density method. The results of the experiment and the simulation were well consistent with each other. Additionally, the second-order element of the transfer matrix ($x|\delta\delta$) was measured experimentally as -0.47 ± 0.03 m. This measurement was in good agreement with the simulation.

The quantitative performance of the instrument was also evaluated. All stable isotopes of Kr and Ne were observed without the saturation of the detector. A dynamic range of 300 was

achieved by the peak area ratio of $^{21}\text{Ne}/^{20}\text{Ne}$. The gain distribution of the employed focal plane detector was evaluated. In 600–900 channels of the detector, the peak area of ^{20}Ne and ^{22}Ne fluctuated about 40%, and the peak area ratio of $^{22}\text{Ne}/^{20}\text{Ne}$ also fluctuated same amount. This value of the fluctuation is seriously large for the measurements of the isotope ratio. The calibration of the gain distribution in the overall detecting plane is essential. When the detecting position is fixed, a sufficiently useful reproducibility and linearity of the gain was achieved. Therefore, if the gain distribution would be calibrated, the instrument would be available for quantitative analyses.

References

- [5.1] J. Mattauch and R. Herzog. Über einen neuen Massenspektrographen. *Z. Phys.*, 89:786–795, 1934.
- [5.2] H. Matsuda and H. Wollnik. SECOND ORDER DOUBLE-FOCUSING MASS SPECTROGRAPH WITH A WIDE MASS RANGE. *Int. J. Mass Spectrom. Ion Proc.*, 91:19–26, 1989.
- [5.3] M. Ishihara and Y. Kammei. Ion Optical Considerations of a Quadrupole-Octapole Lens System for Variable Mass Range on a Simultaneous Detector. *Rapid Commun. Mass Spectrom.*, 3:420–423, 1989.
- [5.4] Ishizuka Electronics Corporation, Tokyo, Japan. *PRODUCT CATALOG*.
- [5.5] M. Ishihara and T. Matuo. A new ray tracing code “ELECTRA”. *Nucl. Instrum. Methods B*, 70:445–450, 1992.
- [5.6] R. F. Harrington. Matrix methods for field problems. *Proc. IEEE*, 55:136–149, 1967.
- [5.7] M. Nishiguchi, M. Toyoda, M. Ishihara, M. Ohtake, T. Sugihara, and I. Katakuse. Development of a miniature double focusing mass spectrograph using a focal plane detector. *J. Mass Spectrom. Soc. Jpn.*, 54:1–9, 2006.

[5.8] J. R. DE LAETER and J. K. BÖHLKE and P. DE BEVRE. ISOTOPE-ABUNDANCE VARIATIONS OF SELECTED ELEMENTS. *Pure Appl. Chem*, 75:683–800, 2003.

Chapter 6

Conclusion

A miniature double-focusing mass spectrograph has been developed as a prototype model for a lunar exploration. The computer program TRIO 2.0 was developed for the design of the ion optical systems, with which the new ion optical system for employing a focal plane detector was designed. The ion optical properties and the quantitative performance of the constructed instrument were evaluated. From this work, the following conclusions can be led:

Development of the computer program TRIO 2.0

The computer program TRIO 2.0 was developed. The program has many functions for the design and evaluation of the ion optical systems and, moreover, useful GUIs were equipped. The aberration coefficients can be calculated up to third-order by the transfer matrix method. The program accepts a system including the following ion optical components: drift spaces, electrostatic sectors, magnetic sectors, electric or magnetic quadrupole lenses, and multipole lenses. The program supplies functions to evaluate the ion optical properties of a system. The following properties can be simulated and visualized: ion trajectories, the image of the beam profile, the beam envelope and the ion transmission, the TOF peak, and the energy and angular focal planes. It should be noted that all the programs of TRIO 2.0 are written in a modern object oriented language of Java. This brings us a high expandability, flexibility and maintainability of the coding.

Design and construction of the miniature double-focusing mass spectrograph

The miniature double-focusing mass spectrograph was newly designed and constructed. The ion optical system was designed to satisfy the double-focusing along a straight line being at a distance from the exit fringe of the magnetic sector to employ a focal plane detector. In the design, the ion optical properties of the system, e.g., beam profile, mass resolution, beam envelope, and transmission were evaluated by TRIO 2.0.

The instrument is comprised of an EI ion source, a spherical electrostatic sector, a homogeneous magnetic sector and a focal plane detector using a CCD. A CCD driver system and a data acquisition system was developed.

Performance evaluation of the instrument

The ion optical properties and the quantitative performance of the newly constructed instrument was evaluated. The mass resolution of 130 was achieved with the main slit width of 0.25 mm, which is in good agreement with the simulation. The detectable m/z range was estimated from a spectrum of the residual gases. The result was well consistent with the theoretically calculated value. The energy and the angular focal planes were evaluated. In the system, double-focusing was successfully achieved along a straight line. The focal planes, however, curve slightly toward the magnet as the mean radii in the magnetic field decrease. Then, the energy and angular focusing points were simulated to compare with the experimental result. These results of the experiment and the simulation well agreed with each other. In addition, the second-order element of the transfer matrix ($x|\delta\delta$) was measured experimentally as -0.47 ± 0.03 m. This measurement was in good agreement with the simulation by TRIO 2.0.

The quantitative performance of the instrument was evaluated. A dynamic range of the simultaneous detection was achieved as 300 from the spectrum of neon. Moreover, the gain distribution of the employed focal plane detector was evaluated. The peak intensity of the isotope of neon fluctuated about 40%. This result shows that the gain distribution is inhomogeneous in the focal plane detector, and the calibration of the gain distribution in the overall detecting plane is essential. However, a sufficiently useful reproducibility and linearity of the gain was achieved when the detecting position is fixed. The instrument could, therefore, provide a high sensitivity and a good quantitative performance if the gain distribution would be calibrated.

Acknowledgment

The author would like to express his sincere appreciation to Professor Itsuo Katakuse, under whose guidance the work was conducted and completed. He also wishes to express his sincere gratitude to Professor Yasuo Nozue for encouragement and advice. He would like to express his sincere appreciation to Associate Professor Morio Ishihara for instructing him about ion optics and many useful suggestions. He also wishes to express his sincere appreciation to Assistant Professor Michisato Toyoda for instructing him about ion optics and experiments, and useful advice. He wishes to express his sincere gratitude to Mr. Toshio Ichihara for technical supports and useful advice. He also expresses his appreciation to Mr. Hiroki Sakae for technical supports on development of the CCD driver system.

He would like to express his special appreciation to Dr. Kousuke Kumondai and Dr. Daisuke Okumura for useful discussion and advice. He also wishes to express his thanks to colleagues.

Finally, he expresses his sincere gratitude to his parents.